Evaluation of New Zealand Estuarine Water Properties Using Remote Sensing

A thesis

submitted in fulfilment

of the requirements for the degree

of

Doctor of Philosophy in Environmental Sciences

at

The University of Waikato

by

Zhanchao Shao

THE UNIVERSITY OF
WAIKATO
Te Whare Wānanga o Waikato

2024

ABSTRACT

Estuaries and shallow lagoons are the most productive marine systems in the world and contribute to the maintenance of coastal biodiversity by providing various unique habitats for aquatic species. However, due to the inputs of nutrients, sediments and pollutants from the surrounding landscape, light availability and primary productivity can be strongly restricted, which may trigger rapid ecological change over time and cause substantial loss of coastal flora and fauna. This thesis explores the use of Sentinel-2 remote sensing imagery to monitor water properties of shallow intertidal tidal estuaries, for the purposes of managing the estuaries of New Zealand.

The first goal (Chapter 2) was to develop a method to remove the influence of water bottom substrate reflectance in order to detect the true water colour (represented by dominant wavelength) and diffuse attenuation coefficients from Sentinel-2 imagery, in the case study estuary of Tauranga Harbour. The new methodology used direct measurement of bottom reflectance of intertidal areas while exposed, and used a regression estimator to derive subtidal bottom reflectance from particle size (developed using the intertidal properties). The method required the water depth to be known (from LiDAR) and reflectance observations from multiple water depths (either extracted along transects or at the same location at different tides). The method was applied to all available Sentinel-2 images and showed seasonal fluctuations and strong correlations with chlorophyll-a, suspended sediments and coloured metal ions collected by the regional council monitoring programme. This methodology was then applied to 12 estuaries and the results were interpreted in terms of ecological changes (Chapter 5).

The second goal (Chapter 3) was to detect the distribution or density of seagrass/sandflats (where microphytobenthos (MPB) thrive) and use this as a basis to estimate their gross primary productivity (GPP). The new methodology combined Sentinel-2 imagery, machine learning and literature-derived photosynthesis-irradiance ($P - I$) curves. The machine-learning model included (1) supervised classification with random forest to delineate seagrass and sandflat areas (2) and three machine learning regressions (artificial neural network (ANN), support vector machine (SVM) and random forest regression (RFR)) to predict the density of seagrass. The result showed ANN was the optimal algorithm to predict seagrass coverage. By adjusting the input water depth and light

intensity, the methodology could be further developed to predict the response of seagrass and MPB to sea level rise. To counteract the negative impact of increased turbidity caused by coastal erosion and sediment resuspension due to sea level rise and climate change, controlling sediment loading in coastal waters could be an effective solution for maintaining current productivity throughout the entire harbour.

Considering monitoring suspended sediment concentration (SSC) is essential for understanding the resilience of coastal wetlands, a prediction model in Chapter 4 consisting of satellite imagery, numerical simulation and machine learning was developed to enable continuous estimation of SSC. The prediction model included two steps: (1) comparing the Delft3D-derived SSC with corrected satellite data and using K-means classification to categorise the differences into classes; (2) developing a random forest regression model for each class to predict the satellite-derived SSC using Delft3D-derived SSC and other physical parameters. Comparison of the prediction model with *in situ* measurement showed high accuracy, and the model provided the basis for estimating the accumulated sediment in wetlands. The results showed strong sensitivity to different ways of accounting for incoming SSC supply coastal wetlands. Therefore, employing a model based on real-time observations, like the one developed here, would substantially improve sediment budget estimates in coastal wetlands.

Dominant wavelength and diffuse attenuation coefficients (K_d) can form the basis of ecologically relevant indicators. Therefore, in Chapter 5, classification based on these two indicators was developed to cluster New Zealand estuaries with similar states into groups as a basis for management. The dominant wavelength and K_d were derived from the Sentinel-2 images using the seabed correction model developed in Chapter 2. Three groups, including less impacted, moderately impacted and highly impacted, were created which were in broad agreement with other *in situ* measurements and indicator models such as those focused on light availability and benthic health. Therefore, satellite-derived dominant wavelength and K_d can be two good indicators to reflect estuarine water properties for management.

ACKNOWLEDGEMENTS

First and foremost, I would like to thank my chief supervisor Professor Karin Bryan who provided countless amounts of support and guidance during this journey. If not for her dedication, inspiration and motivation, this study would never achieve fruition. Thank you, Karin! A similar level of gratitude goes to my co-supervisors Prof. Conrad Pilditch and Dr. Moritz Lehmann for their encouragement and insights. This journey would never have been so enjoyable without all their help.

I would like to thank the Sustainable Seas, National Science Challenge, for providing the funding for this study. I also appreciate being a recipient of the Terry Healy Memorial Award and Open Access Equity Fund grant from the University of Waikato, which provided financial support for my study and made my publications more accessible.

I also want to thank Georgina Flowers, Dr Varvara Vetrova from the University of Canterbury and Dr Dana Clark from the Cawthron Institute for their significant contribution to my chapters. Special thanks to Dr Josie Crawshaw from the Bay of Plenty Regional Council, Dr Steph Mangan from the National Institute of Water and Atmosphere and Dr Tarn Drylie from the Auckland Regional Council for providing useful data for my chapters. I am very grateful for the great help from Dr Benjamin Stewart, Dr Amin Rahdarian and Joshua Sargent during the fieldwork in Tauranga Harbour.

I really appreciate the unconditional love from my friends and family. I will never forget the moments with my buddies from the Coastal Marine Group, Dr Hemanth Vundavilli, Dr Berengere Dejeans, Dr Wagner Costa, Dr Mariana Cussioli, Edouard, Sanne, Vinay and Shahab. A special thank you to all my friends I have met in New Zealand (Hamilton, Tauranga and Auckland) and at the conference in Spain. Thank you, Alice, Juan and Xin Li. Thanks, Jamin, Wanli, Enge, Yi and other friends based in China for your company over the years. I also want to express my great gratitude to Micheal Stokes, for your unwavering encouragement and invaluable support during this journey. Lastly, thank you, Mum, for supporting me to chase after my dreams. **道阻且長，行則将至。追風趕月莫停留，平蕪盡處是春山。**

TABLE OF CONTENTS

LIST OF TABLES

LIST OF FIGURES

Chapter 1

Introduction

1.1 Introduction

As important transitional habitats that link terrestrial, fresh river water and open ocean, the ecological health of our estuaries is of increasing public concern. A thriving and biodiverse estuary depends on relatively low nutrient inputs, consistent tidal flow, good water quality, stable sediment transport and healthy surrounding ecosystems (Fairweather, 1999). However, anthropogenic and climate change related stress poses a substantial challenge to estuarine health (Tallam & White, 2023) because they are often associated with the introduction of additional nutrients and toxic substances (Costanza et al., 2014; Mastrocicco et al., 2019). Currently, the land-use further up catchments together with land degradation throughout coastal flooding and erosion due to sea level rise controls the inloads of sediment entering marine systems (Borrelli et al., 2020; Ward et al., 2009). The increased suspended sediment concentration in the estuarine water can impact the sediment budget and light availability at the seabed (Neverman et al., 2023). Therefore, this thesis was developed to meet the growing need to establish robust monitoring/predicting systems for estuarine health, including optical water quality, the extent of aquatic primary producers and suspended sediment concentrations.

1.2 Research aims

The overarching objectives of this thesis are to develop remote-sensing based models to monitor New Zealand's estuarine health and to use these in case studies to illustrate how these new methods can provide a step change in our understanding of potential factors affecting the coastal ecosystems. This was accomplished through (1) extracting satellite-derived estuarine optical water quality parameters at scale, (2) detecting the distribution of coastal primary producers and assessing the benthic primary productivity using

machine learning, (3) combining remote sensing and numerical model to provide better evaluation of the control of suspended sediment supply on estuarine wetland resilience, and (4) proposing a nationwide remote-sensing based monitoring system for New Zealand estuaries based on new optical indicators and classifying 12 estuaries as a component on which to base future management.

1.3 Background

1.3.1 Monitoring estuarine health via indicators

1.3.1.1 Estuarine health indicators

Estuarine indicators are tools that are used to monitor the condition and functionality of these delicate ecosystems (Cloern et al., 2016). These indicators include physical, chemical and biological measures that best represent water quality, habitat health, biodiversity or overall system resilience (O'Brien et al., 2016). By monitoring estuarine health indicators, researchers and policymakers can better understand the impact of anthropogenic activities, climatic variations, and other external effects on estuarine habitats. There are a wide range of indicators in common useage, including turbidity, clarity, chlorophyll-a concentration etc. This study mainly focuses on water colour, diffuse attenuation coefficient (K_d), suspended sediment concentration (SSC) and benthic primary productivity because remote-sensing may be a way to collect information on these efficiently and at scale.

Water colour and K_d are the two major indicators that reflect estuarine optical properties. The colour of estuarine water is primarily influenced by the presence of coloured dissolved organic matter (CDOM), chlorophyll-a pigments, and suspended particulate

matter (SPM), all of which contribute to the unique optical properties observed (Kirk, 1994). CDOM strongly absorbs short wavelength light ranging from 400 nm to 500 nm, which often gives the water a characteristic yellow-brown hue. Similarly, chlorophyll-a contributes to a greenish colour, especially during bloom conditions (Bricaud et al., 1981). These inherent optical properties directly impact K_d, which quantifies the decrease in light intensity with depth, governed by absorption and scattering processes within the water column (Gallegos, 2001). Variability in K_d has substantial implications for ecosystem processes, including photosynthesis in submerged aquatic vegetation and benthic habitats, and is crucial for the management of estuarine resources (Davies-Colley et al., 2003). In addition, advancements in remote sensing technology have facilitated the simultaneous monitoring of water colour and K_d on larger scales, providing valuable insights into ecosystem dynamics, water quality, and the potential impacts of climate change (Binding et al., 2008).

Suspended sediment generally comprises a mix of inorganic particles (ranging in size from fine clay and silt to coarser sand), microorganisms, organic materials, and interface spaces (pores) that are carried within the water column (Droppo, 2001). These particles and organic matter, are fundamental to various ecological, geological, and biogeochemical processes within aquatic systems (Syvitski et al., 2005). The presence, concentration, and distribution of suspended sediment in water bodies can be influenced by many factors including river discharge, wind patterns, tidal action, human activities, and catchment land use (Owens et al., 2005). Due to the scattering and absorption properties of suspended sediment, it can substantially influence light penetration of the water column and thus limit the light availability to coastal primary producers (Kirk, 1994). Consequently, primary productivity and the larger food web dynamics in aquatic

ecosystems are likely to be strongly restricted (Kirk, 1994). Furthermore, these particles often function as carriers for pollutants, nutrients, and organic carbon, potentially impacting water quality and marine biota (Bianchi, 2011). Therefore, tracking suspended sediment concentrations and understanding their dynamics is imperative for managing water quality, maintaining ecosystem health, and understanding sediment transport processes (Walling, 2006).

Benthic primary productivity is the production of organic substances by benthic photosynthetic producers, predominantly composed of macroalgae, aquatic plants (seagrass) and microalgae (Ask et al., 2016). These primary producers play a crucial role in energy transfer within aquatic food webs as they can convert inorganic carbon into organic matter, which serves as the food source for the majority of benthic fauna (Pinckney & Zingmark, 1993). Therefore, benthic primary productivity can indicate the general health of coastal vegetation and micro/macroorganisms. In addition to the trophic significance, benthic primary productivity can also influence sediment stability, biochemical cycling, and optical properties of the surrounding environment (Cahoon, 2002). For example, the metabolic activities of primary producers can enhance sediment oxygenation and modulate nutrient fluxes between particles and water columns (Jensen et al., 1993). Given the ecological importance of benthic primary productivity, establishing a monitoring system and understanding its fluctuation and distribution are becoming vitally important for assessing the health and function of coastal ecosystems

1.3.1.2 Monitoring techniques

Methods of monitoring and evaluating estuarine health mainly can be broadly separated into two categories: traditional field measurements and remote sensing. Field

measurements are usually carried out on a small or moderate scale and provide immediate and reliable results relating to classic indicators (i.e. salinity, clarity, turbidity etc.) at specific data collection points (Borkman & Smayda, 1998). For example, in order to measure water colour and turbidity, the Forel-Ule scale and Secchi disc are commonly used in fieldwork (Wernand & Van der Woerd, 2010; Wernand, 2010). However, the spatial limitations of field measurement and the associated costs strongly restrict the feasibility of using such methods at scale.

Compared to traditional methods, changes to estuarine health at scale can be effectively evaluated by a number of environmental/ecological indicators and indices derived by satellite remote sensing. Therefore, remote sensing has rapidly become the predominant technique for large-scale monitoring. After the launch of the first generation of satellites like Nimbus-7, equipped with the coastal zone colour scanner (CZCS), a series of water quality parameters started to be derived at scale including salinity and ocean temperature (Vette, 1991). The sensors equipped on the second generation of water colour scanners (e.g. SeaWiFS) possessed better sensitivity, more bands and higher spectral resolution, which allowed for a more detailed and accurate analysis of aquatic environments (Bailey & Werdell, 2006). Numerous studies emphasized the proficiency of third generation satellite platforms, such as Landsat-8 and Sentinel-2, in delineating detailed water quality parameters like chlorophyll-a concentration (Kuhn et al., 2019), turbidity (Maciel & Pedocchi, 2022) and SSC (Liu et al., 2017) via building empirical or semi-empirical relationships with *in situ* measurements. In addition, the spectral reflectance can also be used as a basis for derived indices including, for example, the normalized difference vegetation index (NDVI) and the tropical state index (TSI), which can provide general insights into vegetation and eutrophication detection (Claverie et al., 2018; Sekertekin,

2021). The overarching benefit of satellite remote sensing lies not just in its cost-efficiency, but also in its ability to provide consistent and comprehensive observations across vast aquatic systems including both water and surrounding intertidal vegetation.

Regardless of the advantages of broad coverage and periodic measurements, monitoring estuarine health using satellites still presents specific challenges due to observation conditions and errors. One primary limitation is temporal resolution. Many satellites like Landsat may not capture the fine-scale dynamics in the small estuarine systems (Petus et al., 2014). The long time between revisits of satellites, as well as poor atmospheric conditions like extensive cloud cover, can also substantially restrict the detection of swift changes in the coastal regions (Mouw et al., 2015). Additionally, the adjacency effect, where light from a bright pixel (like sandy shores) spills over to adjacent darker pixels (like deep water), can result in misleading interpretations (Zhang et al., 2022). With a mix of terrestrial and marine inputs, the complex and dynamic nature of coastal waters further complicates the retrieval algorithms (Mannino et al., 2008). The shallow depths in coastal regions can also cause bottom reflection to influence the remote sensing signal, making it difficult to differentiate between water column effects and seabed contributions (Hedley et al., 2018). These effects can introduce significant errors in the values derived from satellite observations. Therefore, additional *in situ* measurements or numerical modelling might be required to validate and rectify these discrepancies.

With the advance of Artificial Intelligence (AI) in recent years, machine learning models, capable of operating in multidimensional spaces and utilizing complex non-linear relationships, demonstrate their robustness in addressing various spatial data analysis challenges. Artificial neural networks (ANN), support vector machines (SVM) and random forest (RF) techniques are widely used to retrieve chlorophyll-a concentration,

SSC, turbidity and other water quality indicators (Dehkordi et al., 2021; Kim et al., 2014). Another common use of machine learning on satellite data is classification. Due to the unique spectral signatures of different landcovers (Talukdar et al., 2020), convolutional neural networks (CNN) and RF show their broad utility for detecting objects in the coastal environment including seagrass (Ha et al., 2020), algal blooms (Baek et al., 2021) and turbid waters (Nazemi Ashani et al., 2023). The results derived from these models usually show a high agreement with *in situ* measurements or ground truth points because most machine learning models make use of iterative learning to minimize and maximize the error and fit of the models, respectively (Ray, 2019). However, machine learning models can be prone to overfitting based on the size of the training data and their parameter settings, especially when they have multiple collinear training variables like narrow hyperspectral bands (Hafeez, 2022; Rocha et al., 2017). The independent training/testing datasets and appropriate input features/variables can help promote the accuracy of the machine learning models (Ray, 2019).

1.3.1.3 New Zealand estuarine health

The health of New Zealand's estuaries has increasingly been the focus of environmental concern. Over recent decades, in line with global trends in estuarine health, many domestic estuarine areas have been subjected to degradation primarily due to the increased frequency of storms and extreme weather events as well as anthropogenic factors (Dudley et al., 2017; Robins et al., 2016; Sheahan et al., 2013; Thrush et al., 2004). Based on thirteen-year continuous water quality measurements (from 2003 to 2020), about 48% of estuaries in New Zealand have exhibited signs of eutrophication (turning green) at some point, which has been attributed to nutrient loading from agricultural runoff and wastewater discharge (Fraser et al., 2021; Hume et al., 2010).

Locally, the estuarine health of New Zealand is highly dynamic depending on site and time. Some studies find that estuaries from the west coast (Raglan & Kaipara) are generally less clear and more variable in K_d than those on the east (e.g. Tauranga Harbour & Tairua) (Gall et al., 2019). Estuaries including Manukau, Waitemata and Avon-Heathcote/Ihutai receive additional loading of sediments from industrial or urban pollution which strongly impacts the surrounding seagrass beds and benthic communities (Dudley et al., 2017). However, the variation patterns within these estuaries are not consistent with each other in terms of magnitude and time. Other estuaries in the far north like the Hokianga and Rangaunu show much more consistent patterns and vary with extreme natural events such as storms and floods (Fraser et al., 2021). Such challenges underscore the need for proactive monitoring systems; these estuaries are of great importance for biodiversity, Māori cultural values, and the nation's economy (Kettle, 2021).

1.3.2 Simulating sediment dynamics and predicting accumulation

1.3.2.1 Sediment dynamics and accumulation

Sediment transport and accumulation in estuaries is a complex and dynamic process influenced by surrounding discharges, tidal action, vegetation, morphology and salinity gradients. The primary source of fine sediment in an estuary is riverine input, which brings in loads of suspended and bedload sediment from upstream (Douglas et al., 2009). As riverine water velocity decreases as it enters the wider (and sometimes deeper) environment of the estuary, the coarser particles (diameter > 63μm) start to deposit while finer sediments (silt and clay) remain suspended in the water column (Papenmeier, 2012). With the effect of physical forces of attraction and repulsion between particles, the

suspended fine sediments start to flocculate when fresh and salt mix (Partheniades, 1962; Stone et al., 2021). This process involves the clumping of fine particles into larger aggregates (flocs) due to the presence of salts in the water (Manning & Dyer, 2007), which neutralize the electrical charges on the particle (Martin et al., 1986). The increased size and weight of these flocs result in faster settling and deposition in fringing environments such as mangrove and salt marsh wetlands (Manning & Dyer, 2007). The vegetation functions as a physical barrier to sediment transport because the stems and leaves obstruct the flow and further reduce the water velocity (Krauss et al., 2003). This reduction in water speed allows cohesive sediments to settle out and accumulate around the plant structures (Krauss et al., 2003). Over time, the accumulated sediments undergo consolidation, resulting in reduced volume and heightened density. This process is also affected by microorganisms and plant roots, which help stabilize the sediment and prevent erosion of the seabed. (Lee et al., 2014; Roskoden et al., 2020). For coastal wetlands, the rate of sediment deposition is the major control to counteract the effects of increased erosion due to the sea level rise.

1.3.2.2 Numerical simulation

Simple modelling approaches have been used to quantify the accumulated sediments in the fringing wetlands. Most of these approaches are based on the zero-dimensional mass balance equation over each tidal cycle (French, 1993; Krone, 1987). As confirmed by point field measurements (Reed et al., 1999), Temmerman et al. (2003) developed an empirical model that links sedimentation to increasing elevation, distance to channels and marsh edges. Another model based on the advection-dispersion equation, simplified for the study of sediment transport over marsh platforms, suggests that factors like

settling/flow velocity and inundation dept are key drivers of how sediment concentration attenuates along a line running perpendicular to the marsh edge (Fagherazzi et al., 2012).

Spatially and temporally-resolved numeric simulation is further developed to understand sediment dynamics, quantify sediment accumulation and forecast morphological changes in coastal environments. Based on *in situ* measurements such as surface elevation tables (SET) and sediment core analysis (Thomas & Ridd, 2004), popular models including Regional Ocean Modelling System (ROMS) and Delft3D are widely used in hydrodynamic simulations and shallow flows of coastal areas. However, ROMS and Delft3D have different emphases in simulation. ROMS highlights the interaction between between cohesive sediments and broader oceanographic processes including currents, eddies and thermohaline structures (Sherwood et al., 2018). In contrast, by incorporating relevant sediment characteristics (e.g. D50, density, settling velocity), Delft3D focuses on the detailed behaviour of SSC in various estuarine and nearshore environments using different hydrodynamic conditions (Flow or Wave model) (Roelvink & van Banning, 1995). Additionally, Delft3D concentrates on the dynamics between various physical processes that have a direct impact on sediment transport (Roelvink & van Banning, 1995), which provides opportunities to solve the impact of coastal vegetation on turbulence and estuarine exchange dynamics (Temmerman et al., 2005).

Other useful tools include the Princeton Ocean Model (POM) (Doglioli et al., 2004) and the Shallow Water Hydrodynamic Finite Element Model (SHYFEM) (Umgiesser et al., 2004). POM provides precise sediment transport simulation in both deep and shallow waters by solving the nonlinear, hydrostatic, primitive equations with time-dependent parameters including wind stress, heat flux, free-slip lateral boundary condition and quadratic bottom friction (Blumberg & Mellor, 1987). Conversely, SHYFEM addresses

the shallow water equations using a semi-implicit algorithm (fully valid for gravity waves). The resulting 3-dimensional model computes water level and velocity for each numerical domain node, which functions as the basis to estimate rates of sediment erosion and deposition (Umgiesser et al., 2004). Each simulation model caters to different aspects of sediment research, from Delft3D's broad range of applications to SHYFEM's specialization in shallow waters.

The recently developed numerical models have significantly advanced in their ability to capture the role of vegetation in sediment dynamics and its counteracting role in abating escalating coastal erosion. Based on the *in situ* measurements and numerical simulations, several studies have found that vegetation in the fringing environments can promote sediment deposition by increasing the erosion threshold of seabed sediments (Chen et al., 2012) and by providing extra drag force to trap cohesive sediments (Chen et al., 2016). Through incorporating the role of mangrove density in Delft-3D models, Horstman et al. (2015) have confirmed that tropical shorelines are strongly sensitive to coupled sediment-vegetation dynamics. The process-based models integrating biophysical feedback indicate that marshes can provide resilience to the sea level rise by offsetting accretion loss with deposited sediments in sediment-sufficient environments (Kirwan et al., 2016). The new vegetation model based on ROMS suggests that seagrass is important for sediment resuspension within coastal embayments and the long-term survival of coastal wetlands because seagrass can increase the sediment storage budget but reduces the total amount of sediments delivered to marsh platforms at high tides (Donatelli et al., 2018).

1.4 Thesis structure

This thesis consists of four scientific chapters in addition to the Introduction (Chapter 1) and the General Discussion (Chapter 6). Each scientific chapter in this thesis was intended as a self-contained document for submission to a peer-reviewed journal. However, they are strongly interconnected and systematically address the overarching theme of the study. A detailed description of each chapter follows below.

In Chapter 2, in order to monitor the water health of Tauranga Harbour in the long term, I extracted two water optical parameters, dominant wavelength (a numeric way to represent water colour) and diffuse attenuation coefficient (K_d) from satellite images. Due to the significant contribution of the seabed to the water reflectance in the optically shallow regions, I needed to develop methods to correct the biased reflectance in visible bands by using Lyzenga's algorithm. Empirical relationships between median particle size and seabed reflectance were developed during correction. This paper was published in *Remote Sensing*.

In Chapter 3, in order to monitor the vegetation health of Tauranga Harbour in the long term, I developed a machine learning (random forest) model to detect seagrass percentage coverage and sandflat distribution (microphytobenthos, MPB) using Sentinel-2 imagery. The results were compared to *in situ* measured seagrass percentage coverage to evaluate the performance of the machine learning model. The results derived from machine learning were combined with literature-derived $P - I$ curves and the light equation to estimate the benthic primary productivity at scale. This paper was published in *Science of the Total Environment*. I am also pleased to note that the detection model is currently being used by the Bay of Plenty Council and Tasman District Council to investigate the spatiotemporal variation of seagrass areas over the past decades.

The derivation of C_0 was of great importance in estimating the change in the sediment budget of the coast wetland that might accompany sea level rise. Therefore, in Chapter 4, the study aimed to determine the possibility of using the combination of satellite images, numeric simulation and machine learning to predict the incoming cohesive sediment (C_0) in a fringing environment (Ōhiwa Harbour). This paper is in preparation, and will likely be submitted to *Ocean Modelling*.

In Chapter 5, I used the method proposed in Chapter 1 to obtain the dominant wavelength and K_d Blue derived from the corrected reflectance at 13 different estuaries across New Zealand. I investigated the spatial and temporal patterns of these two indicators and attempted to find their correlations with other ecological factors. Additionally, the results from 13 sites were classified based on dominant wavelength and K_d Blue using K-Means clustering. This paper is in preparation, and will likely be submitted to *Estuaries and Coasts*.

Chapter 2

Extracting Remotely Sensed Water Quality Parameters from Shallow Intertidal Estuaries

Shao, Z., Bryan, K. R., Lehmann, M. K., & Pilditch, C. A. (2023). Extracting remotely sensed water quality parameters from shallow intertidal estuaries. *Remote Sensing*, *15*(1), 11.

The southern entrance of Tauranga Harbour

(Source: Bay of Plenty Regional Council)

Contribution of authors

Chapter 2 presents the paper entitled “Extracting remotely sensed water quality parameters from shallow intertidal estuaries”, which was published in Remote Sensing in 2022.

Zhanchao Shao and Professor Karin Bryan both contributed to the model development and manuscript editing. Zhanchao Shao was also responsible for model setup in Python 3, data processing and data analysis. Professor Karin Bryan, Dr Moritz Lehammn and Professor Conrad Pilditch provided useful comments and helped revise the draft.

Abstract

Sentinel-2 imagery is potentially ideal for providing a rapid assessment of the ecological condition of estuarine water due to its high temporal and spatial resolution and coverage. However, for optically shallow waters, the problem of isolating the effect of seabed reflectance from the influence of water properties makes it difficult to use the observed surface reflectance to monitor water quality. In this study, we adopt a methodology based on Lyzenga's model to estimate water quality properties such as the dominant wavelength and diffuse attenuation coefficient (K_d) of shallow estuarine waters. Lyzenga models the observed reflectance (R) using four parameters: total water depth (z), sea-bed reflectance (R_b), water reflectance (R_w) and K_d. If R_b is known a priori and multiple observations of R are available from different total water depths, we show that Lyzenga's model can be used to estimate the values of the remaining two parameters, K_d and R_w. Observations of R from different water depths can either be taken from the same image at different proximal locations in the estuary ("spatial method") or from the same pixel observed at different tidal stages ("temporal method"), both assuming homogeneous seabed and water reflectance properties. Tests in our case study estuary show that K_d and R_w can be estimated at water depths less than 6.4 m. We also show that the proximity restriction for the reflectance correction with the temporal method limits outcomes to monthly or seasonal resolution, and the correction with the spatial method performs best at a spatial resolution of 60 m. The K_d extracted from the blue band correlates well with the observed K_d for photosynthetically active radiation (PAR) ($r^2 = 0.66$) (although the relationship is likely to be estuary-specific). The methodology provides a foundation for future work assessing rates of primary production in shallow estuaries on large scales.

2.1 Introduction

Human effects on estuarine water quality include increased levels of nutrients and suspended solids and reduced light penetration, all with ecological flow-on effects (Tallam & White, 2023). The optical properties of estuarine water determine light availability and can control both submerged benthic and pelagic primary production by shortening the depth of the photic zone in turbid water (Gattuso et al., 2006). It can also alter vertical heat stratification, influencing nutrient availability and the photosynthetic activity of aquatic plants (Chiarelli et al., 2019; Gattuso et al., 2006). The impacts of reduced microphytobenthos (MPB) and macrophyte (e.g., seagrass) productivity are diminished food supply and nursery habitat, as well as changes to ecological interaction networks, which may trigger tipping points in ecological states and contribute to eutrophication cycles (Mangan et al., 2020; Rodriguez et al., 2021; Sundback & Miles 2002; Thrush et al., 2021). Considering the relationship between MPB/seagrass and their surrounding aquatic environment, there is a clear need to monitor the optical properties and turbidity levels of estuarine water at scale to inform sound management practices that will prevent potential habitat loss.

To monitor water optical properties at large temporal and spatial scales, remote sensing is widely used to assess water column turbidity, coloured dissolved organic (CDOM) and chlorophyll-a (chl-a) concentrations by building empirical or semi-empirical regression models between remotely sensed colour bands and *in situ* data (Brezonik et al., 2019; Kamerosky et al., 2015). Recent work has also used water colour evaluated by dominant wavelength as an intuitive way of monitoring water quality (e.g., Lehmann et al., 2018) since it can reflect the water colour as perceived by the human eye in a numerical way. Woerd and Wernand (2015) proposed empirical algorithms to estimate the hue (the

dominant wavelength) and intensity of light using a weighted linear sum of remote sensing reflectance blue, green and red bands, which made it possible to transform satellite signals into colour science data (Wyszecki & Stiles, 1982). These algorithms have been extended to other sensors deployed on Landsat and Sentinel-2 (Woerd & Wernand, 2018). However, there are few studies using satellite-derived watercolour as a compound indicator of water quality in shallow coastal waters due to the difficulty of obtaining true water reflectance.

The accuracy of using remotely sensed observations for water quality and water colour monitoring depends on the methods of obtaining the true remote sensing reflectance from observations. In optically shallow water, the seafloor contributes significantly to the water-leaving signals because photons reflected by the seabed contribute to the measured radiance (Kanno et al., 2013; McKinna et al., 2018). This reflected radiance is a function of the seabed properties (e.g., presence of vegetation, grain size) and causes biases (i.e., a non-water column signal) in remote sensors from which estimates of water quality are derived. Internally reflected light can be ignored because it is not the dominant source of additional upwelling radiance (Lyzenga, 1981). Seabed reflectance can be removed in intertidal regions if the bottom types are known, and light is assumed to attenuate exponentially with depth during submergence (Palandro et al., 2004). The seabed reflectance in visible bands can be estimated by the particle size when the sediments are exposed (Sadeghi et al., 2018). Based on Lyzenga's theories, Maritorena et al. (1994) proposed an equation to demonstrate the relationship between observed reflectance, bottom reflectance and deep-water reflectance, in which the bottom is assumed to be a Lambertian object:

$$R = (R_b - R_w)e^{-2K_d z} + R_w \quad (1)$$

where R is the reflectance of a visible band observed by sensors just above the water surface (spectral dependency is omitted for simplicity of notation); R_b is seabed reflectance; R_w is water reflectance at infinite depth; z is water depth and Kd is (the band-specific) diffuse attenuation coefficient. The spectral analysis software Hydrolight provides several theoretical bed reflectance characteristic models, which can be used in addition to *in situ* water quality measurements and Lyzenga's model to extract K_d and Rw from imagery (Mobley & Sundman, 2022). Recent extensions to the Hydrolight capability include wind speed and zenith angle in methods to estimate the true water surface reflectance (Albert & Mobley, 2003).

The primary objective of this study was to develop a methodology based only on Lyzenga's model (without the need for *in situ* water quality measurements) to remove the seabed reflectance and isolate the water reflectance and diffuse attenuation coefficient for optically shallow estuarine water. The corrected water reflectance could then be used to extract true watercolour (dominant wavelength) and to evaluate the relevance of this information (as well as K_d) to monitoring the estuarine ecological state. We also show how an established regression between the median sediment particle size and reflectance could be used to extend the corrections to shallow subtidal waters.

2.2 Materials and methods

2.2.1 Study area and required data

The study was conducted in Tauranga Harbour (37°39′S, 176°11′E, New Zealand), including its many sub-estuaries (Figure 2.1a). The harbour is large (242 km^2), predominantly shallow (60% intertidal), with a semi-diurnal spring and neap tidal range

of 1.62 m and 1.24 m, respectively (Tay et al., 2011). Seagrass (*Zostera muelleri*) only occurs in the intertidal regions (22.5% of the emerged area), with the remaining seafloor consisting of unconsolidated soft sediments. The seagrass biomass has a seasonal fluctuation where it gradually decreases in winter and reaches a minimum value in early spring (Ha et al., 2020). Fine sediment accumulates in the upper reaches of the estuary, and the main freshwater source of sediment is the Wairoa River (Hume et al., 2022). Therefore, these two factors have long-term and seasonal effects on water colour signatures and influence seabed characteristics.

This study used the Sentinel-2 Level-2A data product downloaded from the European Space Agency. In this product, satellite-measured top-of-atmosphere radiances have been corrected for atmospheric effects to yield surface reflectance. We used the bands (blue, green and red) at their native 10m pixel resolution. Fifty-one Level-2A images with cloud coverage less than 5% were selected for the Tauranga Harbour region. These images were divided into the northern and southern harbour at the natural sand barrier (dashed white line, Figure 2.1) to compare the difference in water optical quality between basins.

Water depth at each pixel at the time of data acquisition was derived from a merged elevation-bathymetry map and tide levels. The merged map was created by combining a digital elevation model (collected by airborne light detection and ranging (LiDAR)) of the intertidal regions with subtidal bathymetric data (single and multi-beam) assembled by the Port of Tauranga. The bathymetry has an accuracy of ±0.13 m (Stewart, 2021). Sediment grain size observations (Figure 2.1) were made into a spatial map with inverse distance weighting by Rullens et al. (2021) (Figure 2.1b–d). Photosynthetically-active radiation (PAR) measurements used in Flowers et al. (2023) were also collected at the sites shown in Figure 1a.

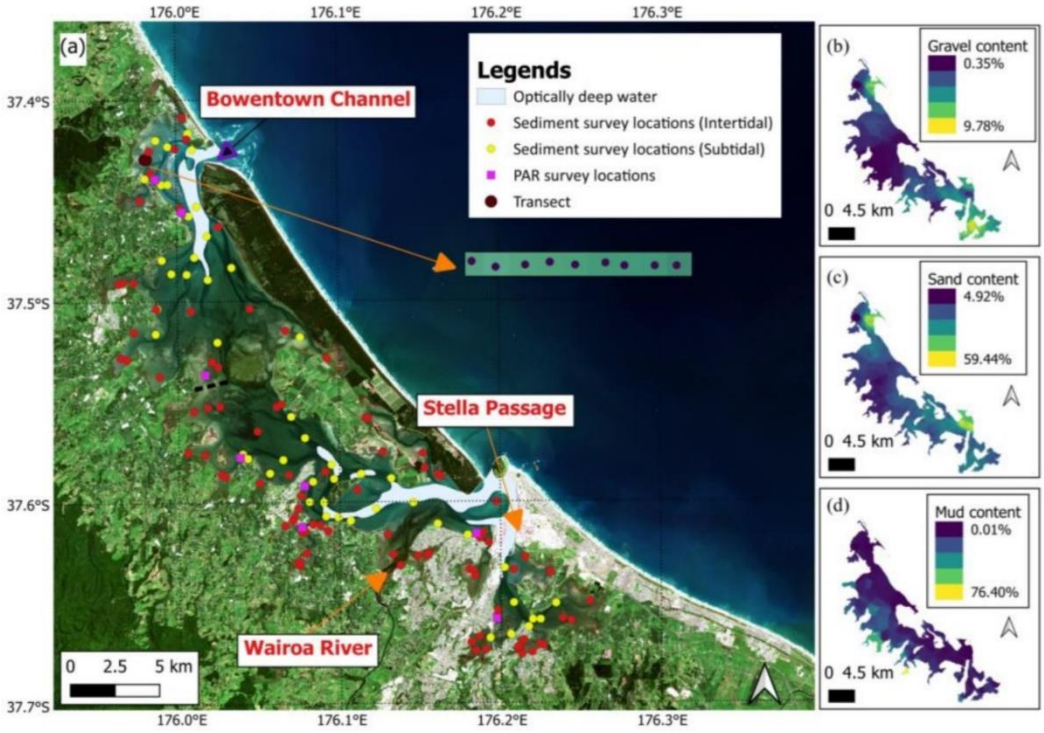

Figure 2. 1 Optically deep-water regions (where no corrections were needed) and in situ measurement (sediment and PAR) locations in Tauranga Harbour. (a) The in situ sediment data in the intertidal (for regression) and subtidal (for extrapolation) were provided by Clark et al. (2018) and Ellis et al. (2017), respectively (see Methods). The PAR data were provided by Flowers et al. (2023). The location of the spatial transect shown in the figure in Section 2.2.2.1 is marked with a black circle. The black dashed line is the natural barrier that isolates Tauranga Harbour into the northern and southern harbours. The selected transect was close to the northern entrance of the harbour. (b–d) Maps of sediment content percentages (gravel, sand and mud) from Rullens et al. (2021). The background image is from Sentinel-2.

2.2.2 Methods

Equation 1 shows that the reflectance measured at the water surface contains a contribution of R_b, which depends on K_d and z. To solve Equation 1, R_w, R_b and K_d must be approximated. For R_b, we either measured it directly when the sediments were exposed at low tide (intermittently exposed, Figure 2.2), or we used the relationship between R_b and particle size to infer R_b in permanently inundated regions (Figure 2.2)

(details in Section 2.2.2.1). With R_b constrained, we then optimised Equation (1) using observed reflectance collected over multiple water depths, assuming that R_b, R_w, and K_d are constants over these water depths (detail in Section 2.2.2.2). In the deep channels, z was large enough relative to K_d that $R \sim R_w$ (deep water in Figure 2.2).

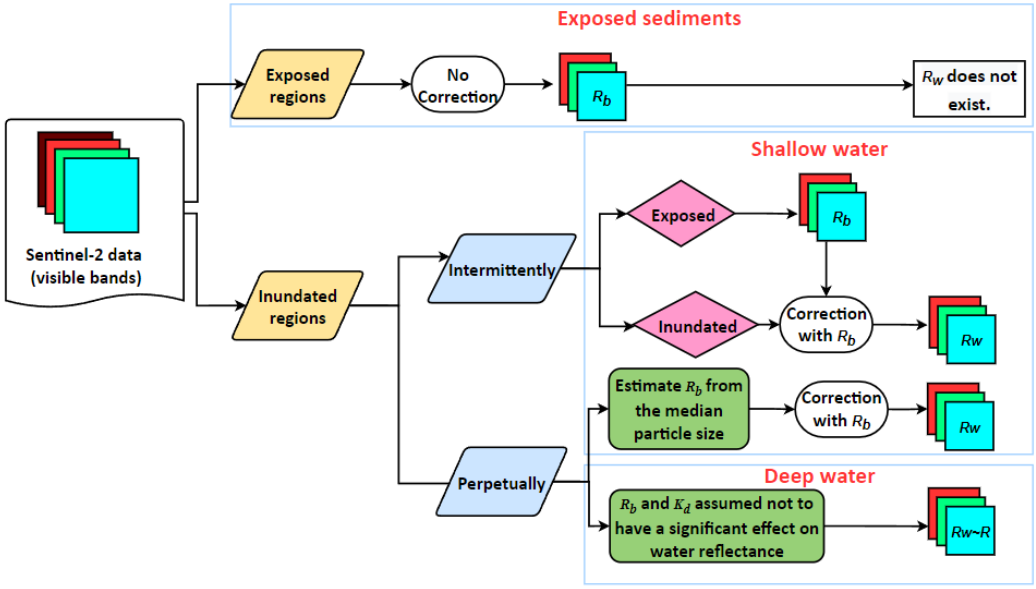

Figure 2. 2 Flow diagram showing how pixels are treated with respect to extracting the bottom and water reflectance, depending on whether they are permanently, temporally or never exposed.

The spectral information of intertidal vegetation (generally seagrass) in the harbour is different from the soft sediments, which change R_b. Intertidal areas where seagrass is abundant can be mapped using a supervised classification scheme tested by Ha et al. (2020). For simplicity, here we exclude these areas and use non-seagrass regions to extract R_w and K_d. However, seagrass areas could also be used by measuring the R_b of these regions while exposed (Tauranga Harbour has almost no subtidal seagrass).

2.2.2.1 Estimation of seabed reflectance

Our method for estimating R_b depended on whether the region was inundated, and so each pixel in the Tauranga Harbour image collection was classified in a simple way: exposed, intermittently inundated and perpetually inundated (Figure 2.2). Pixels were classified as exposed or inundated using the normalised deviation water index (NDWI) calculated with Band 3 (Green) and Band 8 (NIR) from the Sentinel-2 data (McFeeters, 1996). The variation of the NDWI has been shown to be good for the detection of waterbodies or changes in water level, using 0.3 as a threshold (McFeeters, 2013).

$$\text{NDWI} = \frac{R(Green) - R(NIR)}{R(Green) + R(NIR)} \tag{2}$$

For the intermittently exposed sediments, R_b could be derived from images taken at low tide. The curve in Figure 3.3a shows a synthetic example of R calculated using Equation 1 as a function of water depth ranging from 0 m (exposed) to 1.2 m (inundated). In the exposed region, the depth was set to zero and the reflectance was constant (the red rectangle in Figure 3.3a), and in the inundated region, the reflectance decreased exponentially to deep water, with the rate of decay dependent on K_d. Note that each visible band (blue, green and red) has a different decay rate and a different R_b. The observed reflectance confirmed the expected theoretical trend (examples shown in Figure 2.3b); the reflectance of the exposed pixels varied only slightly due to minor changes in the bed substrate, and R decreased asymptotically with water depth.

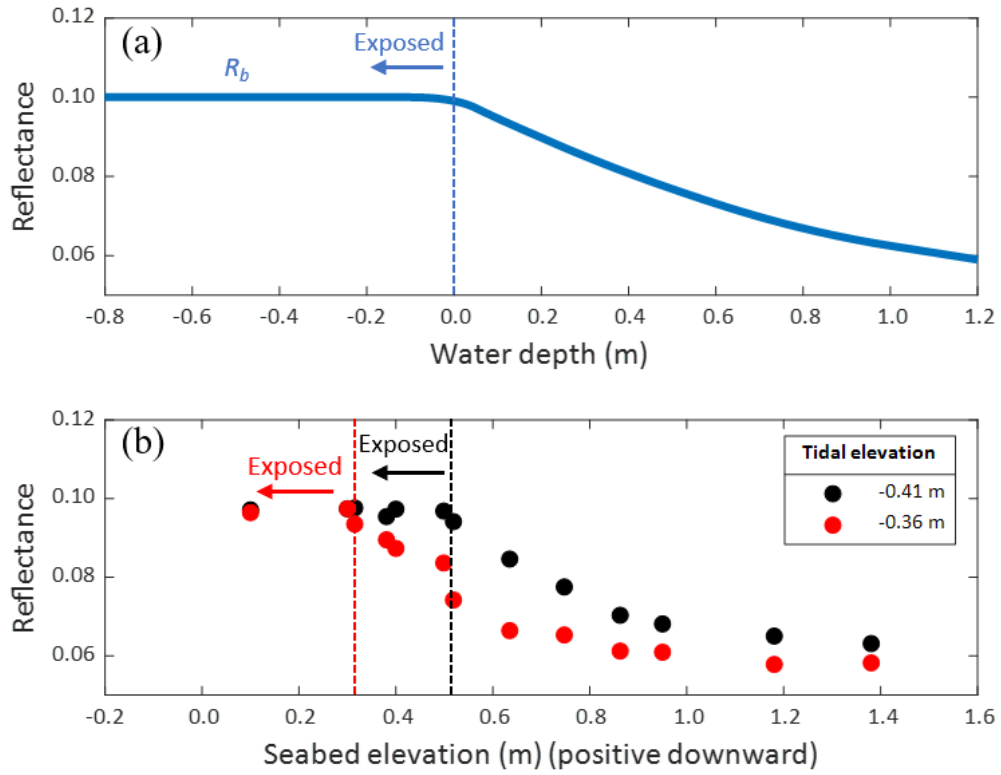

Figure 2. 3 (a) The theoretical dependence of R on water depth according to Equation (1). In this example, K_d was set to 0.5 m^{-1}, R_b was 0.11, R_w was 0.028, and the inundated region was at a water depth greater than 0 m. (b) Examples of the observed reflectance from the transect shown in Figure 2.1 in Band 2 (blue) plotted against seabed elevation for two different tides (in which the tidal elevation is 0.41 m and 0.36 m below mean sea level).

For the perpetually inundated regions, R_b needs to be estimated to correct R (Figure 2. 2) because it is not possible to obtain direct observations of R_b. To do this, we trialled three relationships (linear, logarithmic and exponential) between the *in situ* measured median particle size (d) and the reflectance of exposed pixels in each visible band (following Sadeghi et al., 2018), which we then applied to predict R_b using grain size maps for subtidal regions. Although R_b may depend on mineralogical composition as well as particle size, in Tauranga Harbour, the sediments in deeper water are from the same source as those in shallow water, which should restrict the variations in grain composition. The *in situ* median particle size data (115 samples) were derived from an ecological

survey of Tauranga Harbour (Ellis et al., 2017) and monthly measurements collected by the Bay of Plenty Regional Council in the intertidal regions (Figure 2.1a). Combined with 45 samples from subtidal regions collected by Clark et al. (2018), Rullens et al. (2021) used these *in situ* data to create sediment texture maps by using inverse distance weighting interpolation (Figure 2.1b–d). These sediment texture maps were resampled from 100 m to 10 m (Figure 2.1b–d) and were used to estimate the median particle size of each pixel in the perpetually inundated regions. In summary, spatial maps of R_b were constructed using direct measurements of seabed reflectance in regions that were exposed at low tide and using inferred values in subtidal regions (inferred using the intertidal relationships between median particle size and reflectance (Figure 2.2)).

2.2.2.2 Calculation of R_w and K_d

Having established a protocol to determine R_b across the range of elevations in the harbour, the next step was to solve the optimization problem and extract an estimate of R_w from an observed signal R using Equation 3 (Equation 1 rearranged). A numerical search algorithm was applied to seek the value of R_w that minimised the variance (V) and trend (S) in $K_{d(i)}$ over a range of depths z_i (assuming that the water properties are homogeneous across these pixels and any systematic differences in K_d at different depths were caused by the incorrect choice of R_w).

$$K_{d(i)}(\lambda) = \frac{1}{2z_i} \times \ln\left(\frac{R_b(\lambda) - R_w(\lambda)}{R_i(\lambda) - R_w(\lambda)}\right) \tag{3}$$

where R_i is the reflectance at pixel i with water depth z_i in band λ. To be assumed to be homogeneous, the pixels needed to be in close proximity. From here on, we drop the notation λ for clarity, but all analyses were performed separately for each visible band.

Given those proximal pixels (either in space or time) would have different depths in a shallow estuary, either because the depth changed gently over the intertidal region (spatial changes) or because the tide changed through time (temporal changes), the requirement of evaluating Equation 3 at multiple water depths to solve the optimization problem could be satisfied. An example of how S (the slope) and V (the variance) of $K_{d(i)}$ changed over water depth was provided in Figure 2.4, where each line represented a different "guess" of the value of R_w. The correct R_w in this example was 0.031 because it provided the same K_d at all depths while minimising V. Once R_w is known, the corresponding K_d value can also be calculated by using Equation 3.

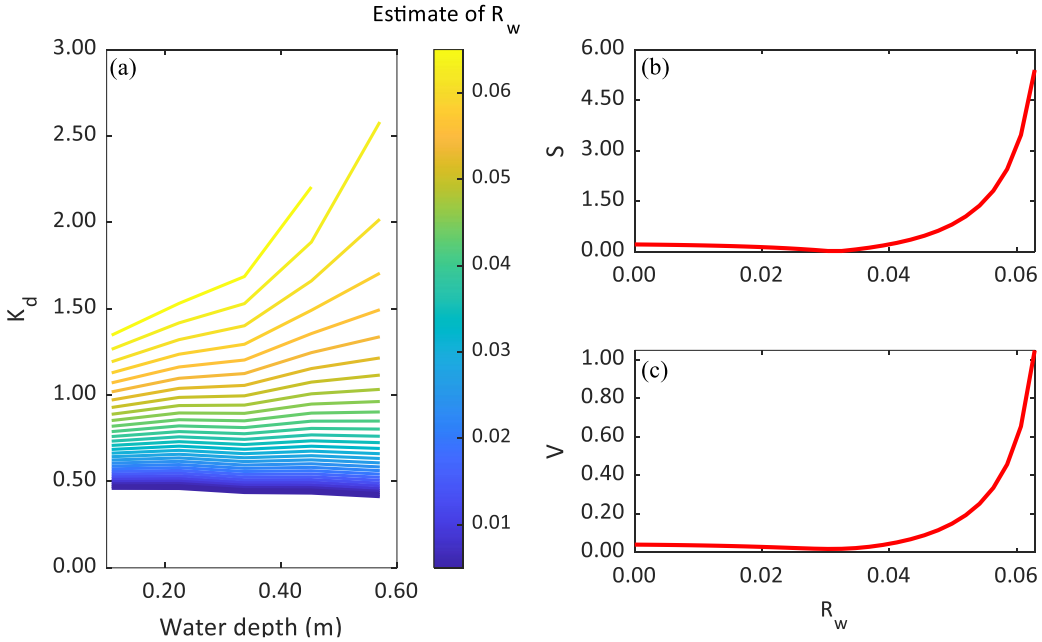

Figure 2. 4 (a) The relationship between K_d (Equation 3) and z, where each line corresponds to a different estimate of R_w (shown by the colour scale). The depths associated with areas that are exposed or covered by both sediments and vegetation are excluded. (b,c) are respectively the trend (S) and variance (V) of each line plotted in (a). S and V are evaluated over the same range of pixels as shown in (a) and clearly show a defined minimum corresponding to the true value of R_w (0.031 in this example).

Proximal pixels with varying water depths could either be selected from a single image where the water depth varied spatially due to the gently sloping intertidal bathymetry or could be selected from a series of images collected at the same location but at different tides. Hereafter, we called these two approaches the "spatial method" R_{ws} and "temporal method" R_{wt}, respectively. In the first case, R_{ws} retained the original temporal resolution, but the spatial resolution was reduced. To retain cross-shore resolution across the intertidal, we implemented the spatial method using square tiles of pixels with different water depths rather than transects. Therefore, the size of the tiles determined the spatial resolution of R_{ws}. In the second case (R_{wt}, reflectance corrected by the temporal method), the spatial resolution was the same as the original images (10 m), but the temporal resolution was sacrificed depending on the time period over which the images were selected and associated with different tides.

In order for the methods to work, the underlying water properties and bed properties should be uniform over the region of proximal pixels. Therefore, we conducted an unsupervised classificating using maximum likelihood on visible and NIR bands to precisely identify the zones where land cover variations were significant, which reauired additional additional manual check. This manual check could avoid areas where seagrass and sediment varies substantially or where seagrass and bare sediment occurred together within the same tile. Considering the spectral information of seabed coverage did not vary substantially over short time frames, we expect variation in vegetation (seagrass) will not have a significant effect on the temporal method.

2.2.2.3 Assessing the optimal resolution to use in spatial and temporal corrections

There is a trade-off between the number of pixels that are used to evaluate R_w and the requirements for homogeneity. More input data should allow Equation 3 to be optimised with greater confidence but may increase the possibility of non-uniform reflectance, in which case it is difficult to detect a minimum in the variance and slope of Equation 3. In total, we tested the spatial method with tile sizes of 40, 60, 80 and 100 m and the temporal method with images from the same month, season and year. Where values were missing due to the algorithm not finding a minimum within a likely range, nearest neighbour interpolation was used to fill gaps in the maps. We assumed that the variation caused by errors in the method should be reduced across the region when the optimal resolution is used for processing. The resolution should maximise the information used to calculate the correction at each location but should still be smaller than large-scale changes in the environment (such as seasonal changes to estuarine characteristics caused by, e.g., changes to seagrass areas, and spatial changes to estuarine characteristics, such as those caused by, e.g., changes to sediment grain sizes). The standard deviation (*STD*) of corrected reflectance (R_w) in each visible region (using either the spatial or temporal method) from shallow water regions was used as a measure to evaluate the model. In addition, a successful correction should return small missing value rates (n), where the missing value rate is the percentage of pixels where Equation 3 could not be solved (where no minima are found). Therefore, *STD* and n were assessed to evaluate the best temporal and spatial resolution.

2.2.2.4 Validating K_d

Due to the difficulty of obtaining direct measurements of K_d at a specific wavelength, we instead used the *in situ* measured PAR values (E_d) (Flowers et al., 2023) at the same

locations but at two different water depths (z) to calculate the $K_{d\ PAR}$ using Equation 4. The in situ measured PAR values were collected using light loggers at 8 sampling sites across the Harbour (Figure 2 .1) from February to March in 2020. We then compared the K_d values in visible bands to $K_{d\ PAR}$ to verify the model for ecological use in shallow water regions.

$$K_{d\ PAR} = \frac{1}{z_2 - z_1} ln\ [E_d(z_2)/E_d(z_1)]), \quad (4)$$

where E_d is downward irradiance over the wavelengths of PAR.

2.2.2.5 Calculation of dominant wavelength using R_w

The dominant wavelength, which reflects the natural colour of objects, is the wavelength of pure spectral colour derived as the intersection of the line joining the white point to the point of interest (in the form of chromaticity coordinate pairs (CIE x, CIE y)) at the border of the Commission Internationale de l'Eclairage (CIE) horseshoe chart (Wyszecki & Stiles, 1982) shown in Figure 2.5.

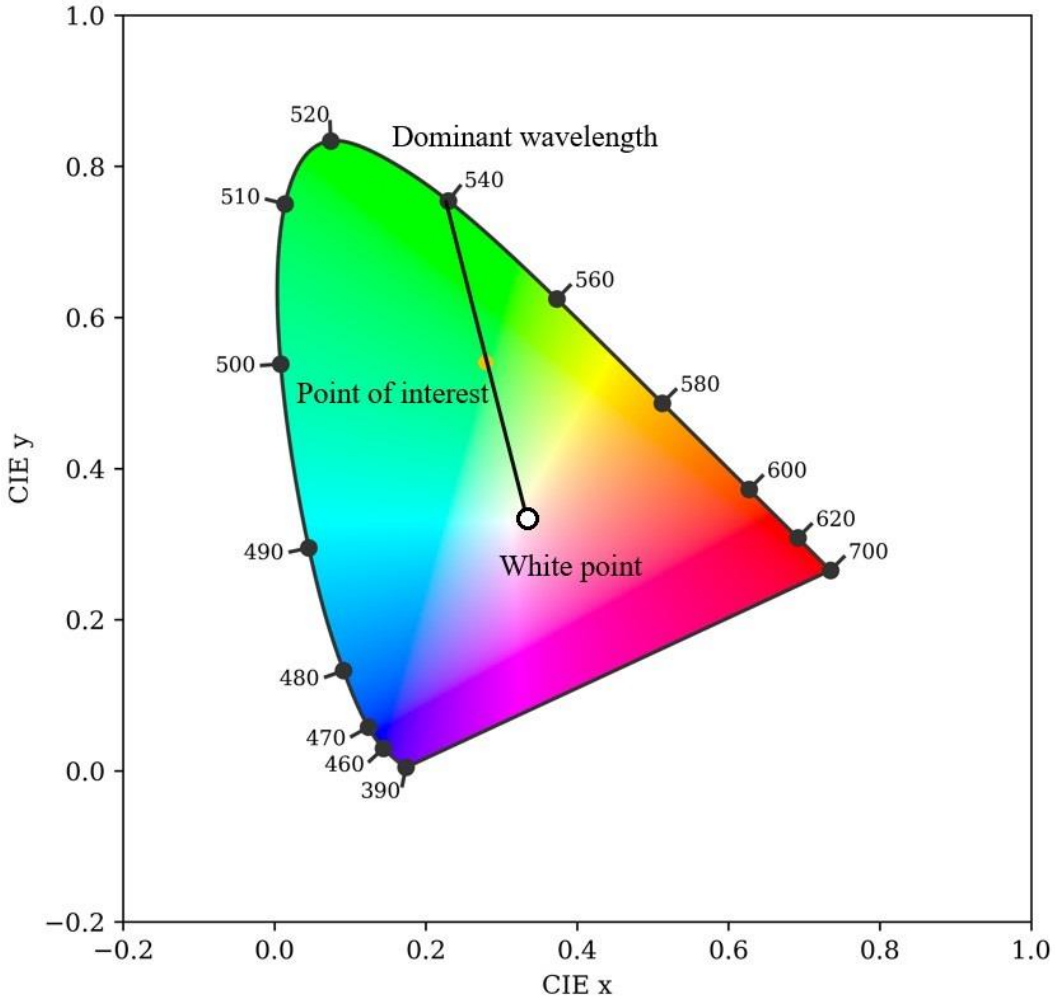

Figure 2. 5 CIE horseshoe chart showing the location of the white point, the point of interest (orange circle) and the associated dominant wavelength. The distance between the white point and the point of interest corresponds to the intensity.

The chromaticity coordinates (CIE *x*, CIE *y*) are calculated by normalising tristimulus values (*X*, *Y*, *Z*) (Equations 5 & 6), which can be obtained by using the multiple linear regression relationships developed in Woerd & Wernand (2015) (Equations 7–9). The chromaticity coordinates provide a measure of watercolour from the reflectance of blue, green and red bands (separately corrected for the effect of the seabed).

$$x = \frac{X}{X + Y + Z} \tag{6}$$

$$y = \frac{Y}{X + Y + Z} \tag{7}$$

$$\mathrm{X} = 6.423R_w(\mathrm{Blue}) + 53.696R_w(\mathrm{Green}) + 32.028R_w(\mathrm{Red}) \tag{8}$$

$$\mathrm{Y} = 22.289R_w(\mathrm{Blue}) + 65.702R_w(\mathrm{Green}) + 16.808R_w(\mathrm{Red}) \tag{9}$$

$$\mathrm{Z} = 31.101R_w(\mathrm{Blue}) + 1.778\,R_w(\mathrm{Green}) + 0.015R_w(\mathrm{Red}) \tag{10}$$

2.3 Results

2.3.1 Estimation of R_b in shallow water

For the exposed regions, R_b was measured directly, but in permanently inundated regions, R_b was inferred. One hundred and sixteen *in situ* samples were used to develop a regression fit between exposed reflectance R_b and seabed particle size (21 samples were excluded due to the presence of seagrass and other vegetation or because the pixel at that location was inundated at the time that the reflectance image was collected). Of the three regression models trailed, the logarithmic regression provided the relationship with the highest r^2 values (Table 2.1), explaining between 5% and 11% more variation than other models.

Table 2. 1 The r^2 values and coefficients of the logarithmic regression ($R_b = a_1 \log(d) + a_2$ for the blue, green and red bands from 2018 to 2020 ($p < 0.05$), where d is the median particle size (μm).

Year	Band	a_1	a_2	r^2
2018	Blue	-0.008	0.107	0.61
	Green	-0.010	0.120	0.66
	Red	-0.006	0.105	0.45

2019	Blue	-0.008	0.102	0.64
	Green	-0.007	0.112	0.53
	Red	-0.007	0.107	0.55
2020	Blue	-0.006	0.090	0.72
	Green	-0.008	0.119	0.61
	Red	-0.006	0.102	0.56

The seabed optical properties did not change greatly over three years, as indicated by the small changes in the standard deviation of reflectance in each band as well as minor inter-annual variation in the fitting coefficients (Table 2.1 and Figure 2.6). These regression relationships were applied to estimate R_b in the perpetually inundated regions (i.e., where R_b could not be observed directly). A spatially resolved example of R_b is shown in Figure 2.7. The R_b values in the visible bands remain similar in the perpetually inundated regions (where the grainsize is similar) and reach lower values (particularly in the red band) in the middle, intertidal regions of the harbour where seagrass is the dominant vegetation.

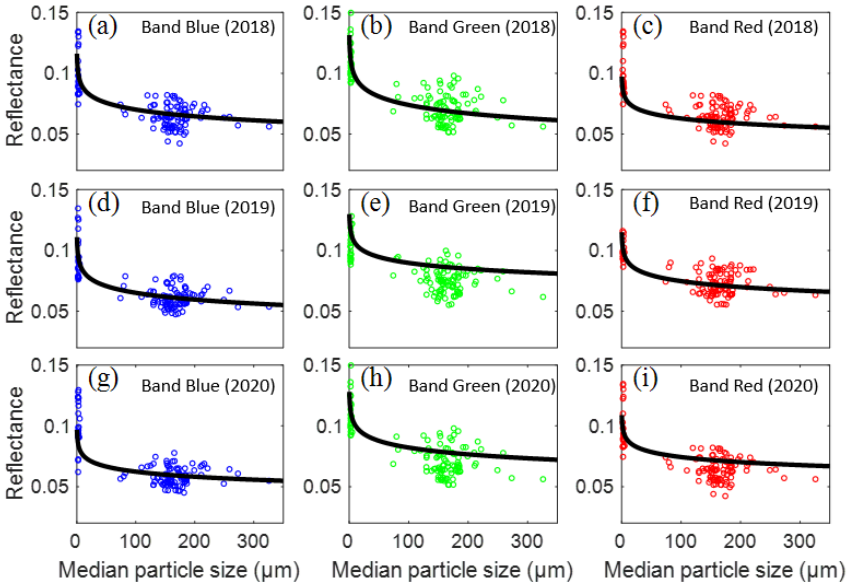

Figure 2. 6 Scatterplots for R_b regressions in each visible band for 2018 (a–c), 2019 (d–f) and 2020 (g–i).

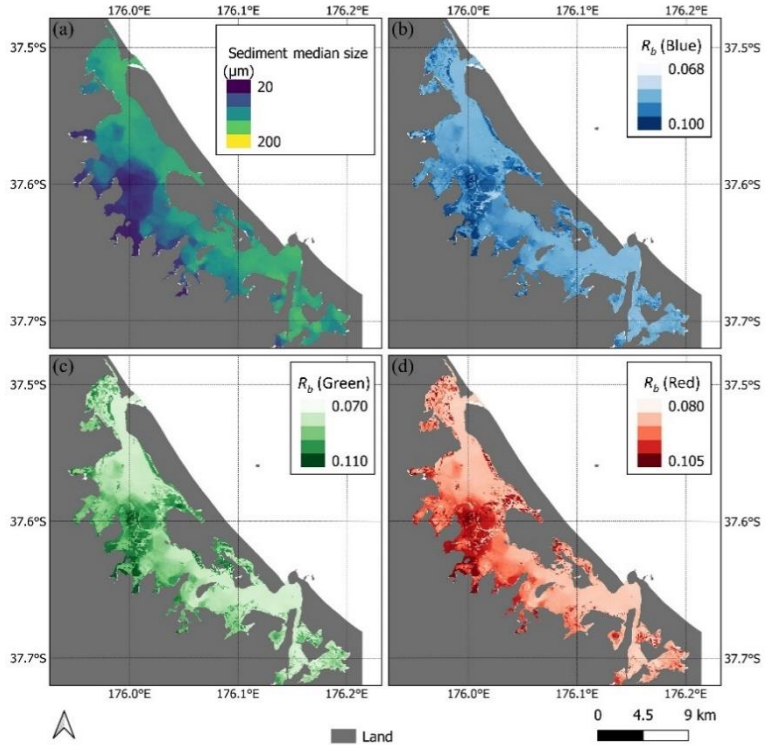

Figure 2. 7 Maps of (a) median particle size derived from the sediment texture maps in Figure 2.1 b–d using the cumulative curve and the estimated R_b (from empirical relationships) in the (b) blue, (c) green and (d) red bands.

2.3.2 Correcting reflectance and assessing the optimal resolution

2.3.2.1 Correction with the temporal method

In the case of the temporal method (R_{wt}), four, nine and sixteen Sentinel-2 images taken at low tides with low cloud coverage were selected to be used in the monthly (February 2019), seasonal (Summer 2018–2019) and annual (2019) corrections, respectively. Using only a month's worth of images meant that conditions varied less, but there were fewer degrees of freedom used to estimate reflectance. Nevertheless, extraction using the monthly and seasonal corrections had a greater success rate with a lower standard deviation (*STD*) in the optimal values of R_{wt} (Figure 2.8) and *n* (Table 2.2). The annually resolved correction performed the worst, with more than 50% of pixels returning missing values in each visible band and a high value of averaged *STD* after using temporal methods. Therefore, we selected monthly-resolved R_{wt} to calculate the dominant wavelength and K_d of shallow water in Tauranga Harbour.

Table 2. 2 The STD and n of the R_{wt} in visible bands after monthly, seasonal and annual correction, respectively.

Band	Evaluator	Monthly	Seasonally	Annually
Blue	*STD*	0.012	0.011	0.012
	n	17.98%	35.62%	54.06%
Green	*STD*	0.011	0.010	0.013
	n	16.28%	27.21%	50.18%
Red	*STD*	0.007	0.006	0.008
	n	15.15%	34.61%	52.69%

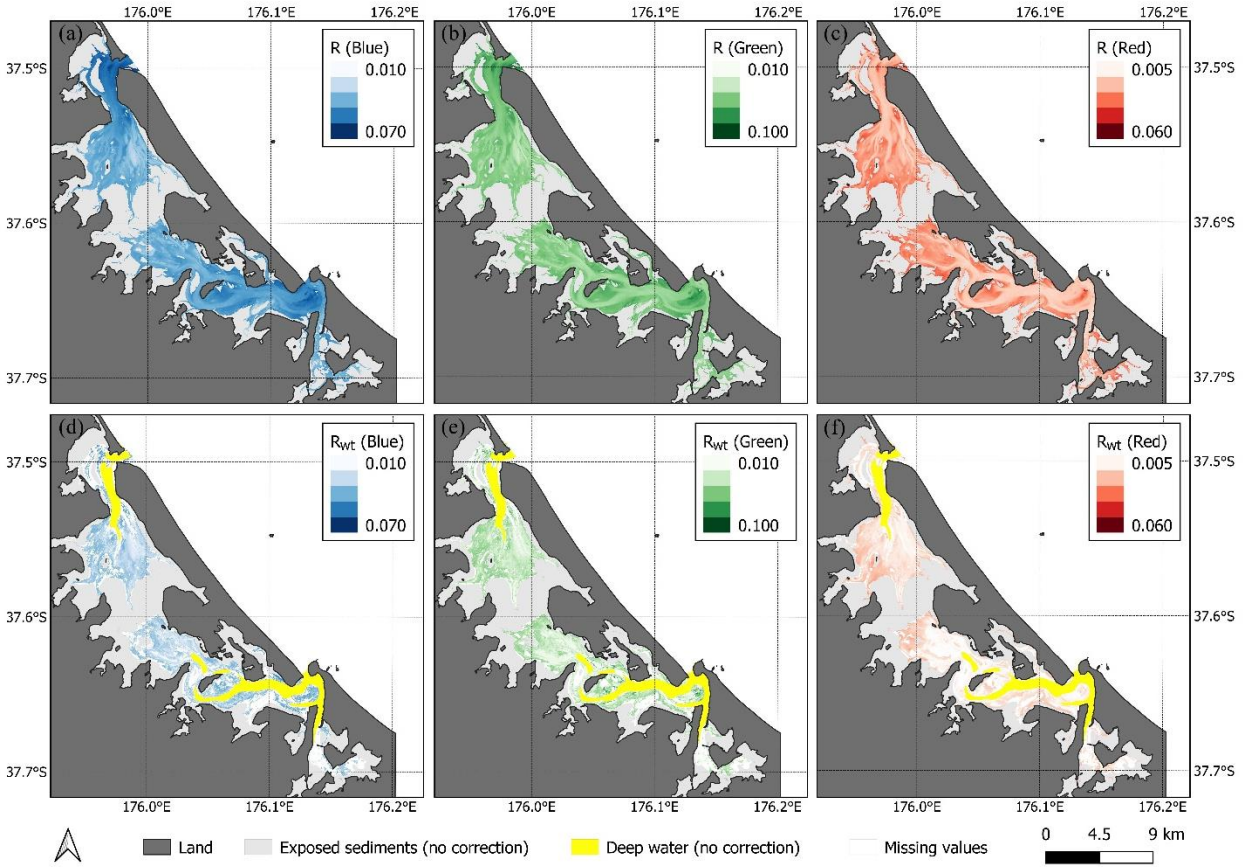

Figure 2. 8 Maps of averaged reflectance of blue, green and red from the selected four images in inundated regions before (a–c) and after (d–f) correction using the temporal method (applied monthly). The reflectance before the correction was averaged over four images in February 2019, so it could be better compared to the corrected maps, which are based on four images collected at different water depths. Reflectance in emerged (exposed sediment) regions and optically deep channels did not need correction, which are marked in grey and yellow, respectively. The missing values due to nonuniform input data are marked in white.

Correcting for seabed reflectance using the temporal method changed the signals substantially in most regions, removing the patterns in R caused by the effect of R_b (the uncorrected images showed patterns associated with underwater channels (Figure 2.8)). Although in regions of large spatial variations (such as near the interface of sediment and water), the method was less effective, some original signatures of the seabed were still evident. The corrected R_{wt} in shallow water was reduced to a similar range as that of the deep channels (Figure 2.8), where no correction is needed, which also contributed to a reduction in *STD*. Sometimes large seagrass meadows in shallow water made it difficult to obtain R_{wt} because R_b varied too much. The pixels that were difficult to correct (where a solution to Equation 3 could not be found) were either close to a deep channel or surrounding irregular seabed features (missing values in Figure 2.8).

The dominant wavelength of shallow water decreased by ~20 nm after correction using the temporal (applied monthly) method, from yellow (reflecting the influence of the generally sandy bed) to a greener colour (compare Figure 2.9b&c). The corrected colour of shallow water was close to that of deeper channels near the entrance, where the bottom was assumed not to contribute to water reflectance (Figure 2.9d). The exposed sediments had fairly homogeneous optical properties with a dominant wavelength of ~570 nm (Figure 2.9a).

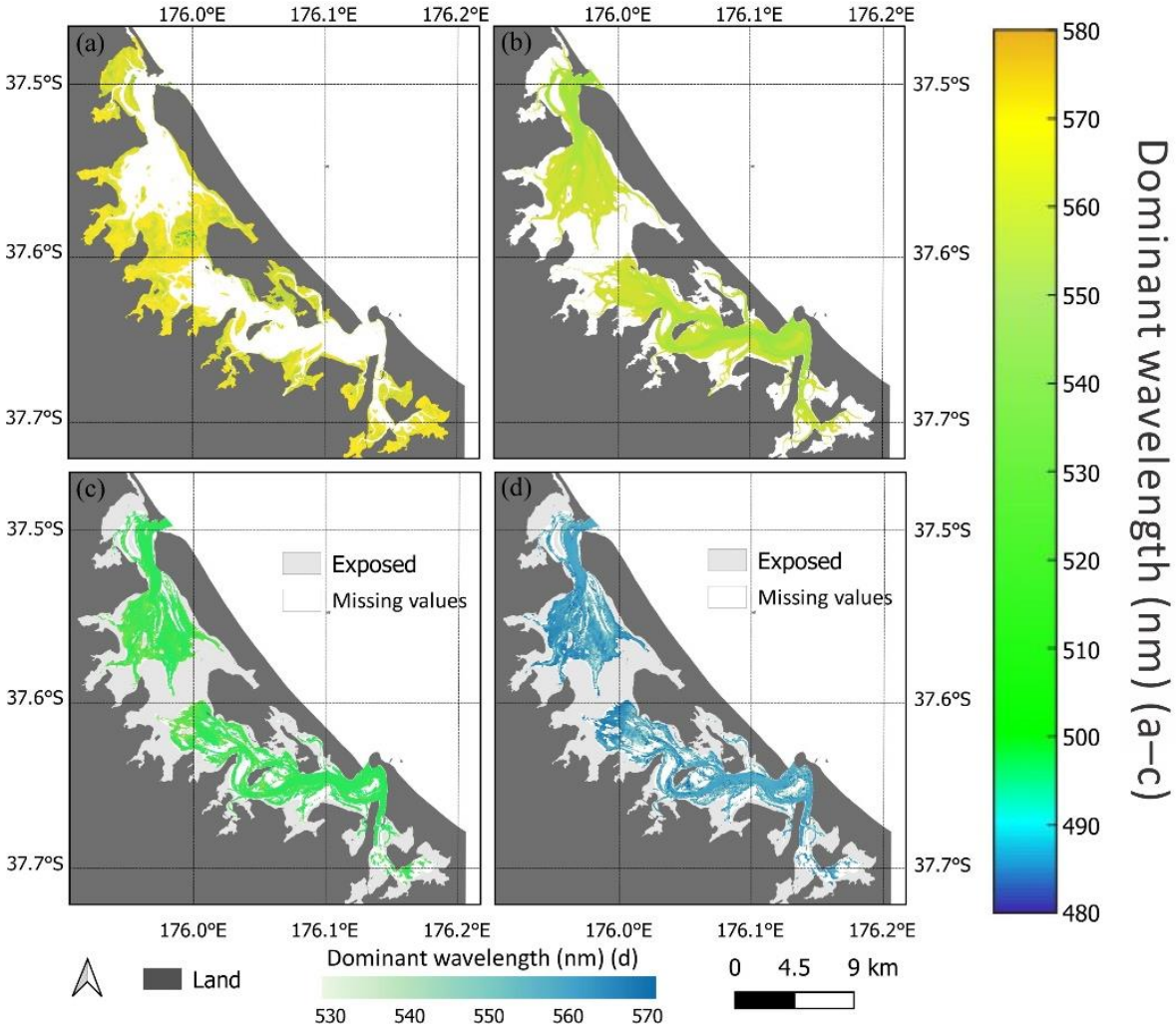

Figure 2. 9 The dominant wavelength of exposed sediments (a) and underwater regions before (b) and after correction with the temporal method (applied monthly) in January 2019 (c,d). (a) The colour of exposed sediments not needing correction (the area of which varies with tidal state). (b) The monthly averaged dominant wavelength of the shallow and deep water prior to any correction. (c) The colour after correction of the optically shallow regions (deep water pixels are not corrected, R_w~R), where the colour scale (right) reflects the true dominant wavelength. (d) The same data as in (c), only with a different colour scale for readability (scale at the bottom). Consistent with Figure 2.8, the exposed regions and missing values are marked in grey and white, respectively.

2.3.2.2 Correction with the spatial method

The spatial method (R_{ws}) decreased the original spatial resolution (10 m) depending on the size of the tile used to fit Equation (3). We tested the optimal number of pixels to use

in fitting the Sentinel-2 image on 5 February 2019 at high tide. The optimum resolution of the spatial method was 60 m, where the *STD* of corrected reflectance was also minimal relative to other resolutions with a low missing data rate (Table 2.3). The 40-m or 80-m resolved corrections provide similar results and are useable when a higher or lower resolution of data is needed, respectively. The 100-m resolved correction was poorer, with *n* of 21.89%, 23.54% and 21.29% in each visible band (Table 2.3). Therefore, in this study, we used a 60-m resolved correction to remove the seabed reflectance and calculate the dominant wavelength and K_d.

Table 2. 3 The STD and n of the R_{ws} in visible bands using four different tile sizes with spatial method (40, 60, 80 and 100 m), respectively.

Band	Evaluator	40 m	60 m	80 m	100 m
Blue	*STD*	0.012	0.008	0.012	0.011
	n	16.35%	19.67%	20.18%	21.89%
Green	*STD*	0.014	0.013	0.011	0.012
	n	15.72%	17.31%	18.65%	23.54%
Red	*STD*	0.010	0.009	0.011	0.010
	n	17.19%	18.85%	20.72%	21.29%

Although the spatial method generally showed good performance in shallow water, the results might be missing or biased in the regions where the input reflectance of the seabed varies substantially. These regions included the interfaces between exposed sediments and shallow water, between shallow water and deep water and between vegetation and sediments or water. In shallow water, the corrected reflectance in each band was significantly reduced, by 13% (blue), 25% (green) and 23% (red), relative to the uncorrected one (Figure 2.10).

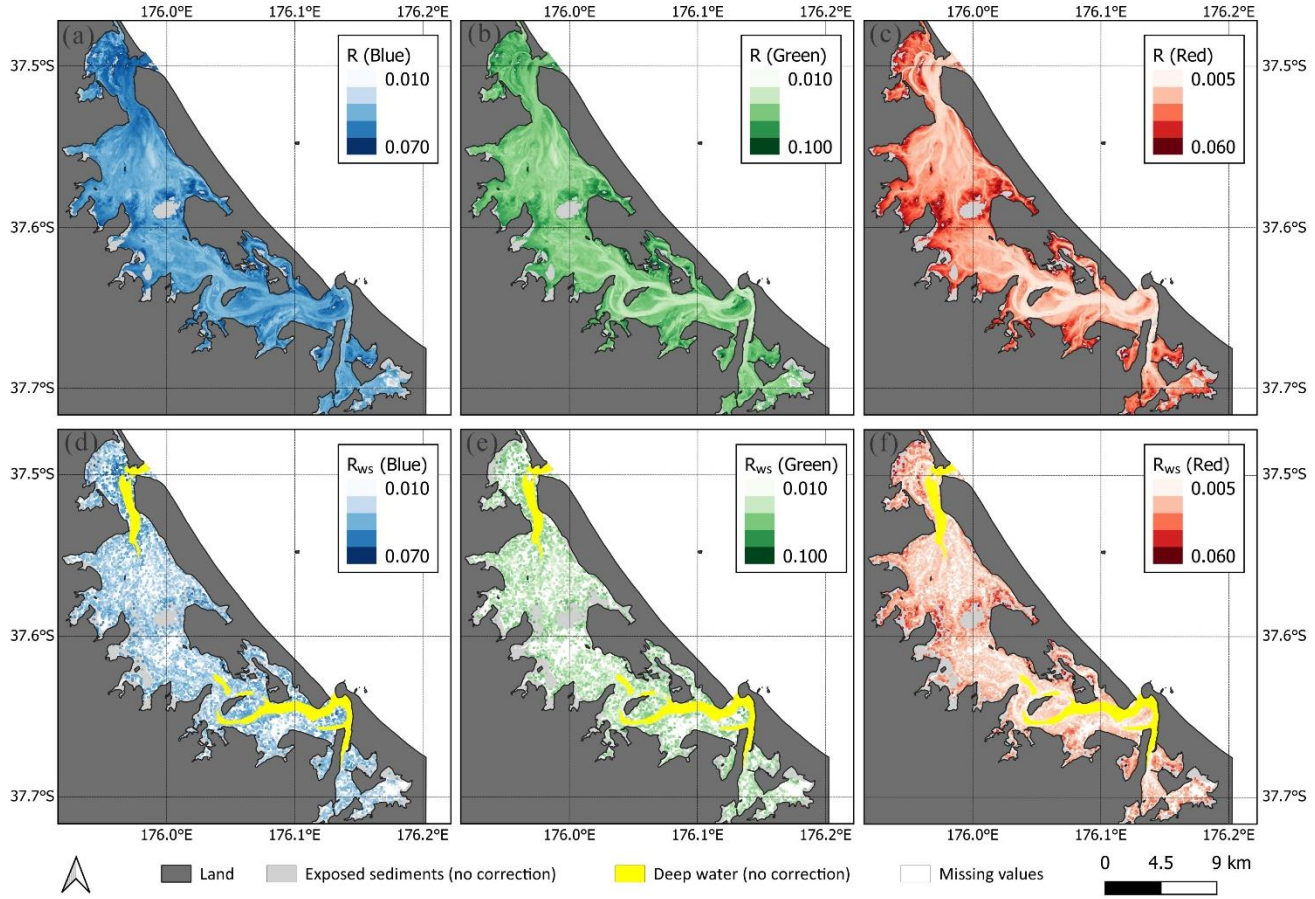

Figure 2. 10 Maps of blue, green and red band reflectance in inundated regions before (a–c) and after (d–f) correction using the spatial method (with a 60-m tile size). The reflectance before correction was derived from the Sentinel-2 image on 5 February 2019 at high tide. Reflectance in emerged (exposed sediment) regions and optically deep channels did not need correction, which are marked in grey and yellow, respectively. The missing values due to nonuniform input data are marked in white.

The area of the exposed seabed (reflectance values not needing correction) was small in this example (compared to Figure 2.9) because high tide covered the sediments (Figure 2.11a). The colour of shallow water regions after correction was significantly different from that before correction. In the uncorrected image (Figure 2.11b), the seabed morphology was clearly evident, with the shallow regions differentiated from the green channels; these patterns disappeared after correction (Figure 2.11c). When the corrected image was replotted using a finer resolution colour scale (Figure 2.11d), the intersection between channels and shallow water regions might show a slightly erroneously high value of the dominant wavelength. This might result from a drop in the number of uniform data points used in the processing to estimate the true water reflectance. The deep channel was not substantially affected by the seabed reflectance, and so it did not need correction (Figure 2.11d).

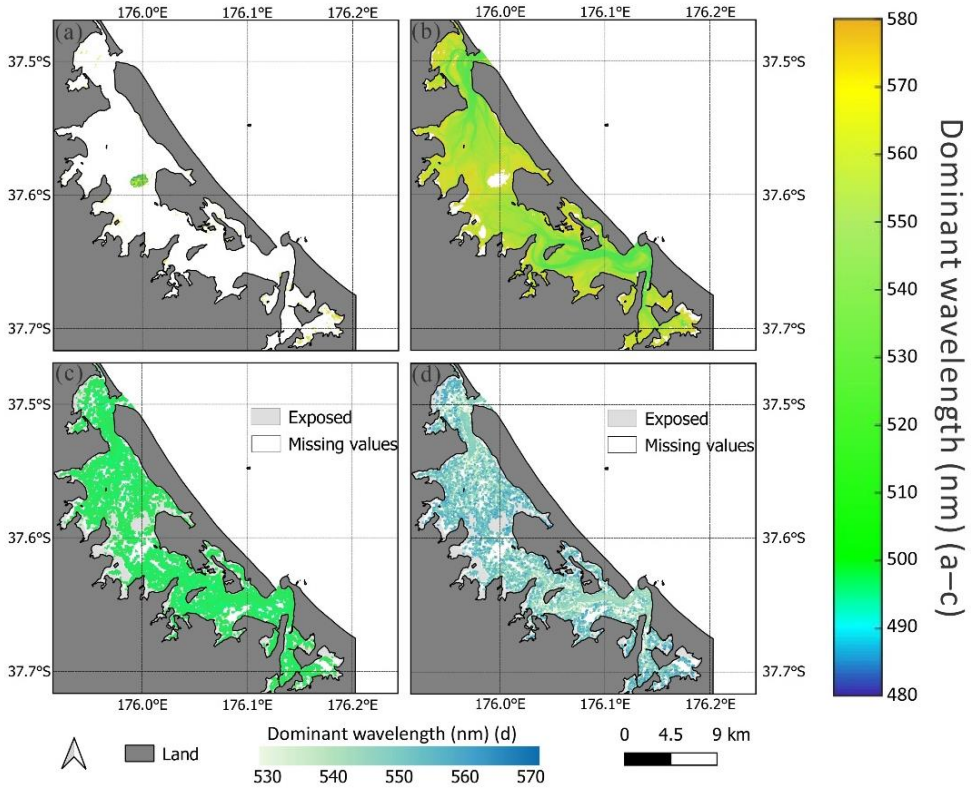

Figure 2. 11 The dominant wavelength of sediments and underwater regions, corrected using the spatial method (with a 60-m tile size) in Tauranga Harbour on 5 February 2019 (a case with a high tide). (a) The colour of exposed sediments along the coastline and mangroves in the middle harbour. (b) The dominant wavelength of shallow and deep water regions before correction. (c) The colour of shallow water regions after correction with the scale of the true dominant wavelength (R_w~R in the deep channels). (d) The colour of the water regions after correction with a different colour scale for readability. Consistent with Figure 2.10, the exposed regions and missing values are marked in grey and white, respectively.

The effect of our bottom correction on dominant wavelengths can be visualised using chromaticity coordinate plots (Figure 2.12). The spatial and temporal methods showed consistent results, comparing the dominant wavelength before and after correction. The dominant wavelength ranged between 520 nm and 578 nm and between 540 and 580 nm for uncorrected data, and from 521 nm to 574 nm and from 572 nm to 540 nm after correction with the temporal and spatial methods, respectively (Figure 2.12). The scatter using the spatial method declined partially because the spatial method decreased the spatial resolution (Figure 2.12a), while results from the temporal method were not affected in the same way (Figure 2.12b). In both plots, some points

collected in shallow water with a dominant wavelength over 570 nm before correction likely showed the effect of seabed reflectance on the true water reflectance, considering their colour was almost the same as exposed sediments. There were clusters of points at the dominant wavelength of 560 nm~570 nm before correction. After correction using both methods, the dominant wavelength of these pixels returned toward the greener region (<565 nm) and the majority of pixels from shallow water cluster around the dominant wavelength of between 540 and 560 nm. The lower limit of watercolour before and after correction is close because seabed reflectance did not need correcting in deeper channels (520 nm~540 nm). Some pixels from the shallow water region showed a similar colour to the deep water after correction, which meant the seabed reflectance was effectively removed.

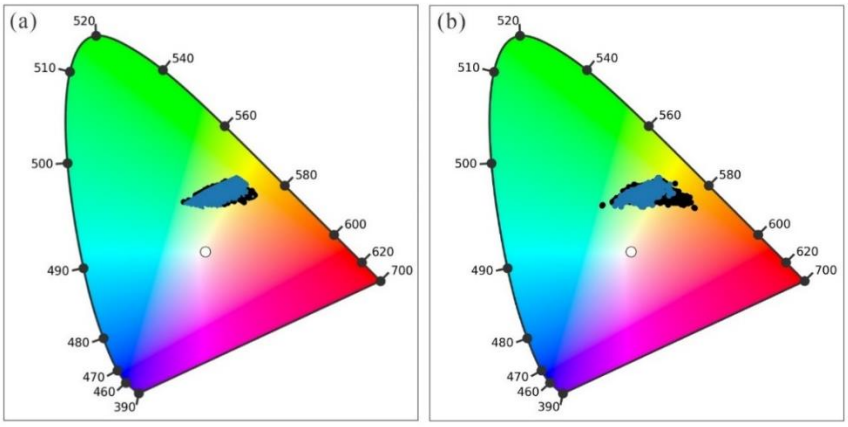

Figure 2. 12 The chromaticity coordinates of reflectance at each inundated pixel (shallow water and deep water) for Tauranga Harbour before (black) and after (blue) correction using the temporal (monthly) (a,b) spatial method (60 m) has been applied. The selected Sentinel-2 image(s) were the same set as used in Figure 2. 9 and Figure 2.11.

2.3.2 The diffuse attenuation coefficient (K_d)

The K_d values derived after the application of both spatial and temporal correction methods to the visible bands shared similar features. Here we show K_d (Blue) as an example (Figure 2.13). The missing values mainly came from pixels in the deep channels

(it was only possible to estimate K_d where the seabed can be detected, Equation 1) and exposed sediments. K_d (Blue) usually had a minimum value (~0.12) in the pixels close to the deep channels, which reflected the probability that turbidity would be low and clarity high in areas that were more flushed with open ocean water. Conversely, the K_d (Blue) tended to be higher at the margins of shallow water and exposed sediments. These regions were usually close to the surrounding sub estuaries and river mouths, where sediment was stirred into the water column by wave action, or delivered to the estuary by the river.

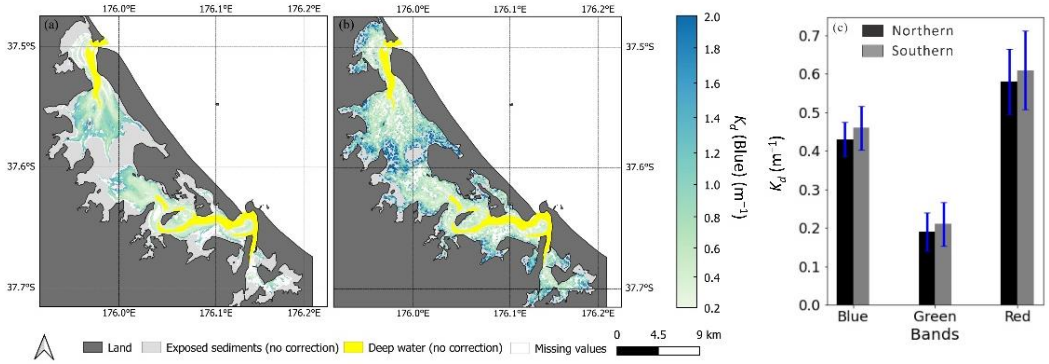

Figure 2. 13 Estimated K_d (Blue) based on the temporal method (applied monthly) (a) and the spatial method (with a 60-m tile size). (b) The images selected corresponding to Figure 2.8 and Figure 2.10, respectively. The exact number of images used for each pixel in the temporally corrected map varied due to tidal conditions. (c) The averaged K_d values (±standard deviation) for each visible band derived from shallow water regions after correction in the northern harbour (black) and southern (grey) harbour.

In order to assess the ecological relevance of the satellite-derived K_d, K_d in each visible band was then compared to the *in situ* measured $K_{d\ PAR}$ (the measurement location is shown in Figure 2.1). Although the correlation between K_d from each visible band and $K_{d\ PAR}$ is usually estuary-specific, depending on turbidity/chl-a concentrations, the fairly high correlation (Figure 2.14) between the *in situ* $K_{d\ PAR}$ and K_d (Blue) might indicate

that K_d (Blue) could be used as a proxy for $K_{d\ PAR}$ for routine ecological monitoring over large regions.

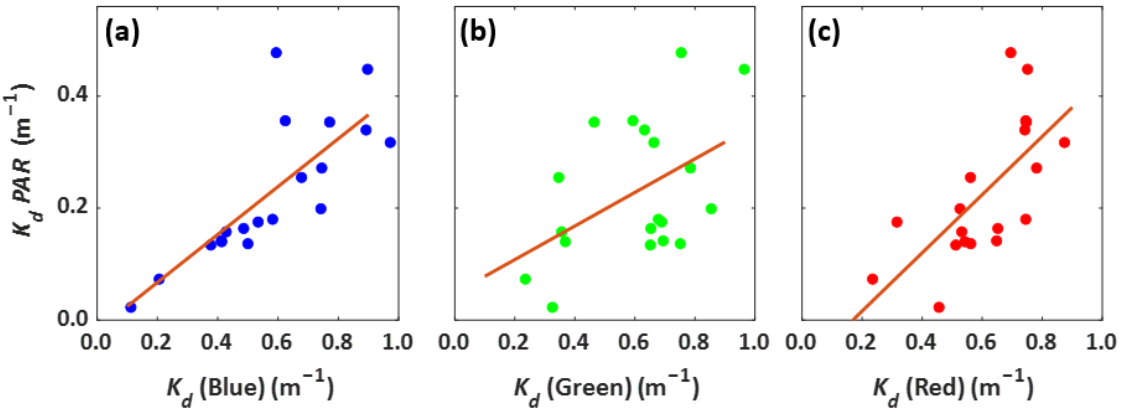

*Figure 2. 14 The correlations between K_d (Blue) (**a**), K_d (Green) (**b**), K_d (Red) (**c**) derived from the spatial method (tile size: 60 m) and $K_{d\ PAR}$ with the r^2 values of 0.66, 0.23 and 0.47, respectively ($p < 0.05$). $K_{d\ PAR}$ was measured in situ (Flowers et al., 2023) on 26 February and 12 March 2020, coinciding with a Sentinel-2 overpass.*

2.3.4 Monthly variations in watercolour and K_d

Monthly variations of shallow and deep reflected water colour over a three-year period showed an apparent seasonal fluctuation, whereas, by comparison, the exposed sediments had near-stable optical properties using a combination of the temporal (monthly) and spatial method (60 m) (when image number was fewer than four per month, we used the spatial method instead and averaged the results for that month) (Figure 2.15a & b). The dominant wavelength decreased to a minimum in winter and returned to the maximum in summer, which meant that the watercolour became greener in summer than in winter (the colour scale on the left of Figure 2.15a,b reflected true colour). The southern Harbour had a slightly greener water colour in shallow and deep water regions (Figure 2.15b), but the overall water colour in Tauranga Harbour was still stable from 2018 to 2020.

We found that diffuse attenuation was mainly affected by location, suggesting that tidally driven variation in light-attenuating material was small relative to tidal conditions. K_d of the southern harbour was higher in the blue, green and red bands than that of the northern harbour (Figure 2.13c), meaning a generally lower-light state. The red and green bands of both harbours had the largest and smallest values of K_d, respectively. The K_d in the band red also had the greatest standard deviation in both harbours. The seasonal fluctuation of K_d (Blue) was small, but the values tended to increase in spring and autumn (Figure 2.15c). The tide conditions seemed to have a weak effect on K_d. The K_d value of ebbing water tended to be higher than that of flooding water (Figure 2.15d).

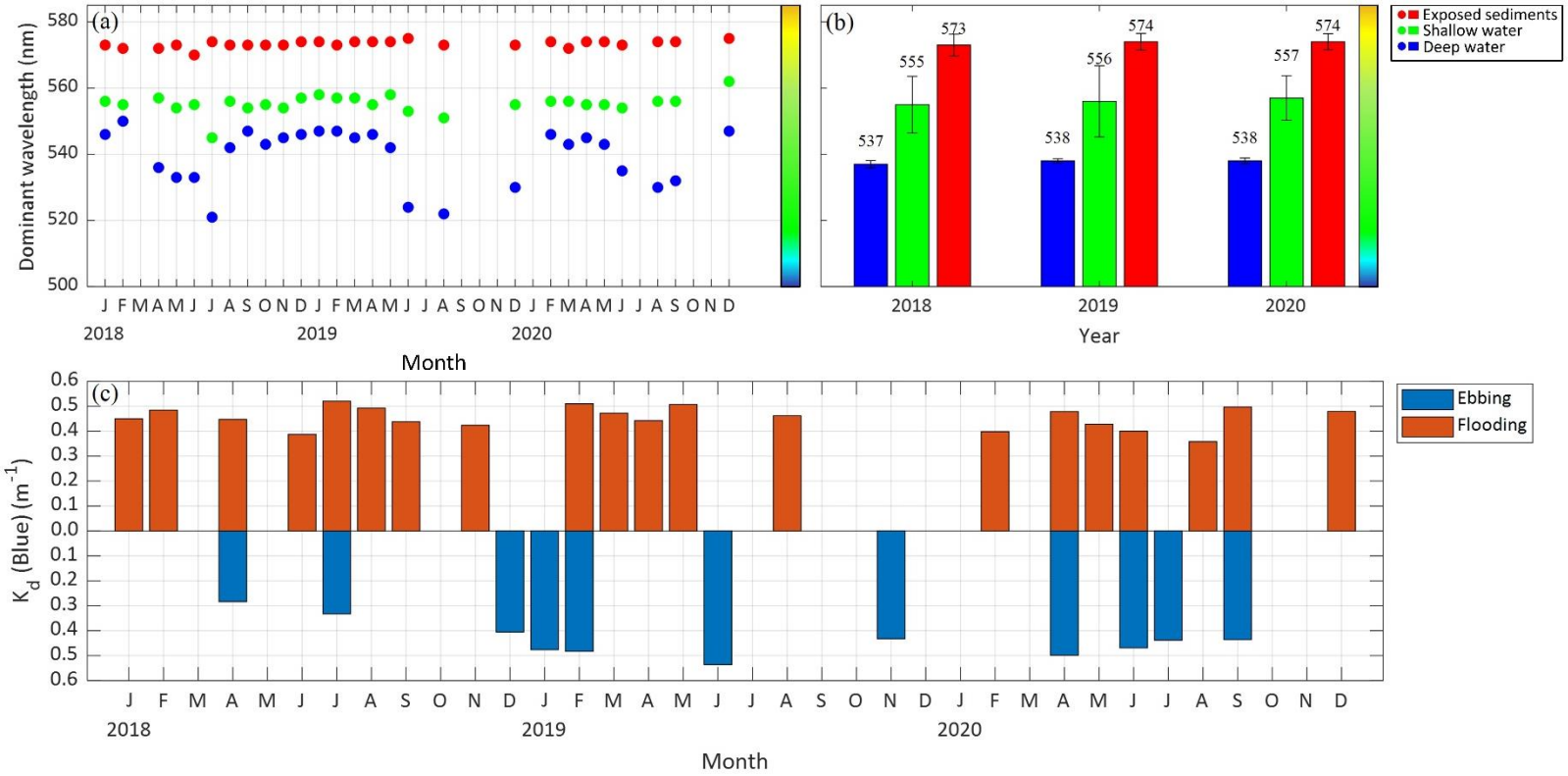

Figure 2. 15 The dominant wavelength of deep water, shallow water and exposed sediments in Tauranga Harbour from 2018 to 2020 using the temporal method (applied monthly), with the spatial method used when there were fewer than four images available in a month (with a tile size of 60 m). (b) Histograms of the annually averaged dominant wavelength of deep water, shallow water and exposed sediments from 2018 to 2020 in the northern and southern harbours. (c) The monthly-resolved K_d (Blue) of shallow water from 2018 to 2020, separated by ebbing/flooding (brown/blue) conditions in Tauranga Harbour. (d) Histograms of the annually averaged K_d Blue measured during ebbing/flooding tides (brown/blue). All panels: Missing values indicate the unavailability of low cloud coverage Sentinel—two images for those months.

2.4 Discussion

In this study, we developed a new application of Lyzenga's model to provide detailed measurements of watercolour and K_d from satellite reflectance measurements of shallow intertidal estuaries by removing the effect of seabed reflectance. The fraction of reflectance accounted for as the bottom signal by our method was the greatest in shallow water and decreased with water depth in a manner consistent with the law of exponential light attenuation in water (Figure 2.16). Note that the error depends on K_d (high K_d weakens the signal from the bottom at the surface), and the example shown here is for our case study. Compared to traditional geostatistical methods for creating maps of water quality (e.g., inverse distance weight interpolation applied to *in situ* measurements, which are more suitable when water quality does not vary spatially substantially), this application can provide a more accurate representation of a large region by accounting for substantial spatial variations in water quality. Therefore, the ecological information provided by this new measurement is useful in these settings to underpin management actions such as setting loading limits for estuaries and monitoring the general health of waters.

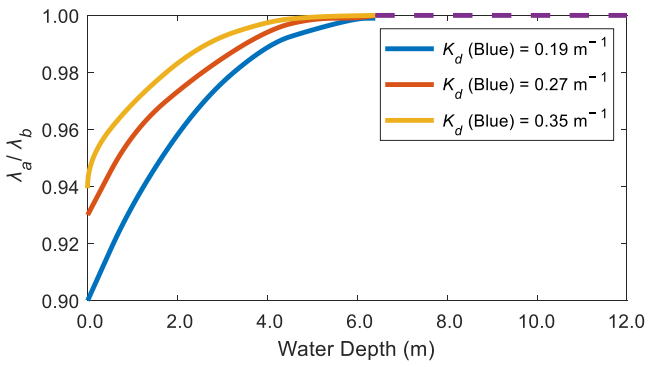

Figure 2. 16 The ratio of the dominant wavelength of water after (λ_a) and before (λ_b) correction with the spatial method (with a 60-m tile size) against water depth from three locations. At depths > 6.4 m (purple dashed line), the dominant wavelength did not need correction.

We propose that water colour corrected for bottom effects is a useful measure for water quality monitoring because it integrates the effect of suspended particles and coloured dissolved substances in the water column, including chl-a (Boyer et al., 2009), CDOM (Brezonik et al., 2005) and suspended particular matters (SPM) (Bowers et al., 2004). The dominant wavelengths reached a peak (shift toward green) in summer (Figure 2.14a), which was consistent with the patterns observed in the *in situ* chl-a concentrations in Tauranga Harbour (Scholes, 2014). Though the concentrations of CDOM, SPM, salinity and suspended sediments varied seasonally (Bowers et al., 2004), chl-a is usually the principal colourant in low-level turbidity estuaries (Lunetta et al., 2009). We found averaged dominant wavelength values of shallow and deep water in the green part of the spectrum (528 nm and 545 nm, respectively) (Figure 2.15b), confirming the importance of phytoplankton pigments for optical water quality in Tauranga Harbour. Moreover, the dominant wavelength in the yellow to red part of the spectrum in the upper fringes of the inundated regions (Figure 2.9 and Figure 2.11) was consistent with CDOM and SPM loading from rivers and sub-estuaries as well as bottom sediment resuspension driven by waves (Cussioli et al., 2019; Lehmann et al., 2018; Lunetta et al., 2009). Note that because of the requirement in our method of a set of proximal pixels with uniform reflectance, the bottom correction using the spatial method could not be applied at the edge of subtidal and intertidal regions where high variation of chl-a and CDOM concentrations occur (Clark et al., 2018). These both cause significant local variations in bottom reflectance and the water depth correction.

Another ecologically relevant parameter that can be derived from satellites is the diffuse light attenuation rate, which governs the photosynthetic rate of inundated areas and thus the productivity of microphytobenthos and submerged seagrass. The variation of K_d responds to multiple drivers and reflects temperature, the input of sediment and the hydrodynamic regime,

which the resolution of our remotely sensed data allows us to explore. Our results showed an increasing trend of K_d in spring, likely associated with phytoplankton blooms triggered by temperature increases, which usually bring elevated chl-a concentrations depending on the cell size and pigments (Fujiki & Taguchi, 2002) (Figure 2.13). For the remaining seasons, SPM and CDOM generally dominated the turbidity, which would also affect K_d (Gall et al., 2019). In autumn, K_d remained similar to the spring value because CDOM contributes to higher absorption coefficients and compensates for the loss of chl-a due to the degradation of organic matter that is added to the CDOM pool at the seafloor (Lund-Hansen et al., 2004).

The maps of K_d (Figure 2.13) showed that location (northern versus southern harbours) and tidal state are the two main drivers of differences in diffuse attenuation in the shallow water regions of the harbour. Considering Tauranga Harbour has several sub-estuaries, the introduction of extra CDOM from the river mouths might create a gradient toward the estuary mouth (observed in Cussioli et al., 2018). This might explain the higher K_d of pixels at the landward margins compared to those close to the deep channels (Figure 2.13a&b). Generally, the more urbanised southern harbour had a higher K_d (Figure 2.13c). About 45% of sediments were introduced to the harbour from the Wairoa River annually, and therefore this region showed a high value of SPM and K_d (Parshotam et al., 2022). The dredged navigational channel in Stella Passage also yielded 25% of sediment loads to the southern harbour and likely had more resuspended sediments from port activities like ship movement (Gall et al., 2019). The K_d difference between ebbing and flooding water might result from tidal differences in the resuspension and transport of suspended solids caused by tidal currents and waves (Figure 2.13c) (Davies-Colley & Healy, 1978). K_d associated with ebbing tides tended to be higher than that of flooding tides because the ebbing tidal currents drained off the shallow water regions where wave-induced bed shear stress is higher (Cussioli et al., 2019).

The primary production of seagrass and microphytobenthos is not only affected by the total amount of light (light quantity) but also the distribution of energy with wavelength (light quality). Light quality can be affected by the source of sediments (Cussioli et al., 2020). Our results allow us to assess K_d at three different wavelengths (Figure 2.14), so we can make spatial and temporal estimates of light quality, ultimately allowing an understanding of the implications of, for example, terrestrial run-off events.

Limitations

Our study describes a method to determine the bulk characteristics (Figure 2.15) of an estuary using satellite remote sensing. Our method can be used to complement *in situ* monitoring for management purposes. Although we did not validate the results due to the difficulty of obtaining direct measurements of K_d, when we made estimates of K_d derived from images from similar adjacent days, the results were consistent (the same was true of the dominant wavelength; details are provided in Figure 2.12 and Supplementary material S1). The variation of K_d between these images remains small over a short temporal scale and within the same season. *In situ* measurements of K_d (PAR) by Cussioli et al. (2020) also show that K_d does not vary over short timescales. The good correlation between K_d (Blue) and K_d (PAR) also supported the potential of using K_d (Blue) to estimate K_d (PAR) in ecological studies (Figure 2.14).

An assumption of the method is that the seabed and water properties do not change substantially between the collections of pixels that are used to optimise Equation 3. To test the effect of these assumptions, we provided additional modelling in Supplementary material S2 where random noise was superimposed on known values of K_d and R_w, and then Equation 3 was optimised to determine how well the correct values of K_d and R_w could be retrieved. The magnitude of the

error caused by lack of homogeneity was within 10% as long as variations over the set of proximal pixels were less than 10%. The temporal and spatial patterns (or clusters in water and seabed properties (Dimitriadis et al., 2021)) can also increase non-uniformity in the input proximal pixels in our model and increase *STD* and *n* (Dimitriadis et al., 2021). For example, in the temporal methods, if the selected temporal resolution is too long (e.g., annually), long-range variations in the water cycle can contribute to outliers and confuse Lyzenga's model, and therefore is not an optimal time resolution to use (a shorter one is better).

In the intertidal regions, our estimates of R_b were based on direct satellite observations and were therefore spatially explicit at pixel resolution and capable of detecting variations caused by, e.g., seagrass beds. However, in the subtidal regions, R_b depended on the *in situ* measurements used to create a model (in our case, the median particle size), which was fairly sparse. Future work will develop better ways to model this and address this weakness. The effect of poor knowledge of R_b was explored in Supplementary material S2, where we showed that underestimates of R_b in shallow water could lead to large errors in R_w and K_d, (a bias of 5% could lead to an error of ~15%), whereas in deeper water (>2 m), the error is much lower. We did not use pixels with seagrass to develop our model. If the method was extended to R_b of seagrass regions, extrapolations of relationships developed for the intertidal to the subtidal may not account for potential species composition differences. In addition, seasonal variations in growth characteristics (e.g., in *Ulva* and seagrass) (Liu et al., 2022) and other environmental cycles would not be accounted for in the subtidal R_b. This bias shown in Supplementary material S2 would be particularly relevant to seagrass beds due to their lower reflectance in visible bands.

The method will not work well in areas with a very small intertidal range where R_b cannot be measured directly in the shallower waters and used to design a subtidal model. With additional

work, it will be possible to develop models based on radiative transfer equations, for example, as provided by software packages such as “Hydrolight”. In the intertidal regions, the errors of the model for estimating R_b for permanently inundated areas originated from the precision of the median particle size extraction and whether the seabed was covered by seagrass. The model was developed using the reflectance of unvegetated exposed pixels because, in our case study, seagrass did not grow subtidally. The existence of subtidal seagrass would create a bias in deeper water; however, the correction becomes quickly unnecessary at these depths. A more sophisticated classification of the sediments may increase the accuracy of the median particle size values used in the regression model. Several machine-learning-based detection techniques (e.g., Ha et al. 2020 and Liu et al. 2022) can provide the spatial distribution of vegetation in the exposed regions, which could be used to provide values of R_b for seagrass regions in order to extend our method for use in sites with subtidal seagrass. We also assumed that R_b did not change before and after flooding, an assumption that might also introduce errors because the dry and wet sediments might have different reflectance in each band (Verpoorter et al., 2014).

This method cannot be applied to images that have been histogram stretched or contrast-enhanced because this kind of image manipulation would skew the optical relationship between targets and measurements used to develop Equations 7–9. In addition, the spatial method correction requires remote sensing images with a high original spatial resolution. The use of images with a lower resolution, e.g., 20 m or 60 m, increases the mixing of nonuniform reflectance and generates more missing values in the correction process. The images from a medium-resolution spectral imager, such as MODIS and Sentinel-3, are not suitable for the spatial method in these types of estuaries.

2.5 Conclusion

In this paper, we propose corrections that exploit changes in water depth, either spatially (for good temporal resolution) or temporally (for good spatial resolution), to remove the effect of seabed reflectance on water surface reflectance. For the perpetually inundated regions, the relationship between reflectance in different visible bands and the median particle size was established using exposed information, which was then used (with the inundated sediment texture) to estimate the water bottom reflectance of each underwater pixel needed for correction. The most suitable spatial and temporal resolutions for corrections were 60 m and monthly or seasonally, respectively, within the water depth of 6.4 m. The good correlation between K_d (Blue) and $K_{d\ PAR}$ indicated that satellite-derived information could be used to estimate the production of light-dependent inundated estuarine plants. Future work will be directed towards applying this methodology to other estuaries in New Zealand to evaluate their primary production level and predict the changes if turbidity or water depth fluctuates.

Supplementary materials

S1 Consistency check on K_d

In order to overcome the difficulty of a lack of direct measurement of K_d to use in validation, we conducted a consistency check on the K_d maps from adjacent satellite revisiting days. Here, we first took 1 and 31 January 2021 and 20 February 2021 as examples. These images were scanned at high tides (~0.36 m) and low wind speeds (~2 kts). These three images showed a very similar distribution of K_d with mean values of 0.45 m^{-1}, 0.42 m^{-1} and 0.50 m^{-1}, respectively (Figure S1).

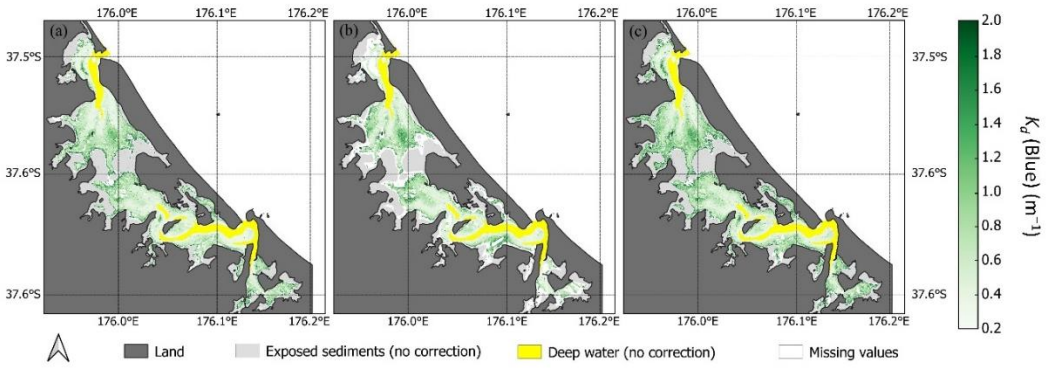

Figure S1 Examples of K_d maps derived from images from the same month with similar conditions ((a) 1 January 2021, (b) 31 January 2021, (c) 20 February 2021). Reflectance in emerged (exposed sediment) regions and optically deep channels did not need correction, which are marked in grey and yellow, respectively. The missing values due to nonuniform input data are marked in white.

Additionally, in order to avoid arbitrary selection on images, we calculated the mean values of K_d from all adjacent days (less than 30 days) in each season. Due to the availability of remote sensing imagery, the number of images selected for consistency checks might be different in each season. The variation of K_d was small, which meant the consistency of this model was fairly high.

Table S1 The consistency check of K_d derived from adjacent days in each season from 2020 to 2021.

Seasons	Number of Images	Mean Values
Summer	3	0.45, 0.42, 0.50
Autumn	2	0.42, 0.40
Winter	4	0.36, 0.38, 0.36, 0.40
Spring	5	0.48, 0.5, 0.46, 0.52, 0.56

S2 Ascertaining the sensitivity of the model to assumptions

There were two major assumptions that might affect the accuracy of the results significantly. Firstly, the assumption that water properties do not vary substantially over the set of proximal pixels with different water depths is used to optimise Equation 3. Here, we use Band Blue as an example. In order to evaluate the accuracy of the model used in this study in water depths less than 2 m, where the seabed effect is greatest, we used three groups of synthetic data where we assumed a constant R_w and K_d over the set of proximal pixels and then superimposed known levels of random variation on these variables (Figure S3). The error was then quantified as the difference between the known value of R_w and K_d and the one derived by optimising Equation 3. The result showed the model could still provide low-error results when the standard deviation of R_w was within 10%, even if the K_d of these regions varies as well (where K_d was modelled with a mean of 0.8 m^{-1} and a standard deviation of 0.2, encompassing the differences between blue and green bands (red attenuates quickly, and so is less relevant) (Figure S2).

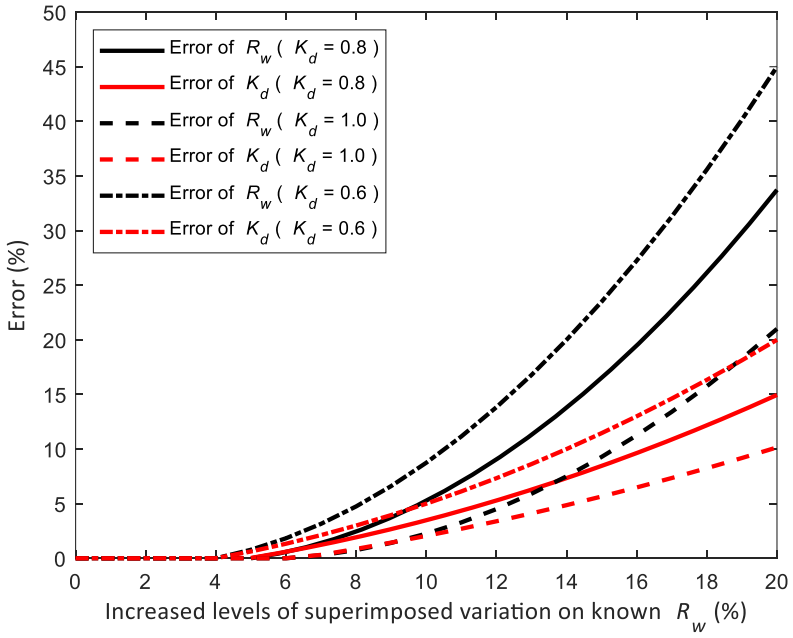

Figure S2 The errors K_d and R_w estimated from synthetic tests (see text) averaged over water depths less than 2 m.

To study the second assumption, we repeated this modelling to evaluate how poor knowledge of R_b leads to errors in R_w and K_d within 2 m (a) and between 2 m and 6 m (b) of water depth, using R_b values that range from 50% too small to 50% too large. The overestimated R_b did not affect the values of R_w and K_d greatly (Figure S3). Although the underestimated R_b could strongly bias the result, the variation of R_b in Tauranga Harbour was actually very limited (0.083 ± 0.03 for >2 m and 0.095 ± 0.01 for <2 m) and unlikely to be biased to that extent.

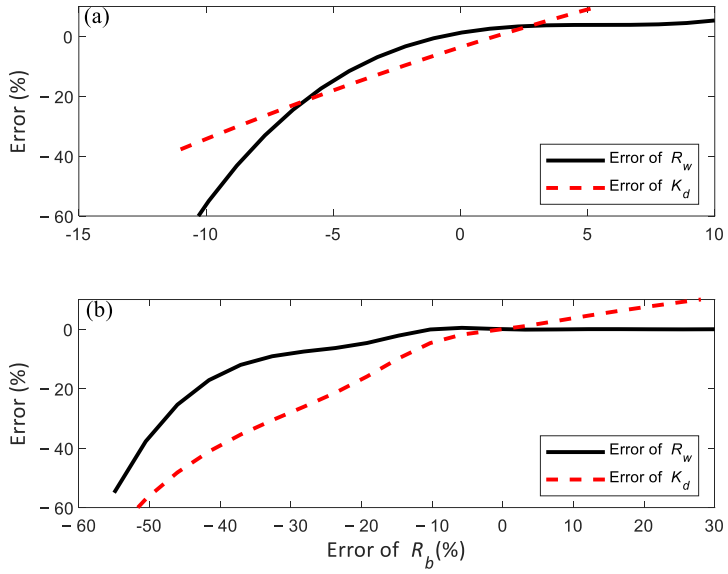

Figure S3 The errors of R_w and K_d averaged for water depths of <2 m (a) and between 2 m and 6 m (b) are caused by an error in the value of R_b.

Chapter 3

Scaling up Benthic Primary Productivity Estimates in a Large Intertidal Estuary using Remote Sensing

Shao, Z., Bryan, K. R., Lehmann, M. K., Flowers, G. J., & Pilditch, C. A. (2023). Scaling up benthic primary productivity estimates in a large intertidal estuary using remote sensing. *Science of The Total Environment*, 167389.

Seagrass in the northern Tauranga Harbour

(Source: Zhanchao Shao)

Contribution of authors

Chapter 3 presents the paper entitled “Scaling up benthic primary productivity estimates in a large intertidal estuary using remote sensing”, which was published in Science of the Total Environment in 2023.

Zhanchao Shao designed the fieldwork and collected the seagrass samples with Professor Karin Bryan and other members of the Coastal Marine Group, University of Waikato. Zhanchao Shao was also responsible for machine learning programming, model setup and paper writing. Professor Karin Bryan, Dr Moritz Lehmann and Professor Conrad Pilditch edited the drafts along with providing helpful guidance on data processing and analysis. Georgina Flowers kindly provided the useful parameters of photosynthesis-irradiance curves to help calculate benthic productivity.

Abstract

As two main primary producers in temperate intertidal regions, seagrass and microphytobenthos (MPB) support estuarine ecosystem functions in multiple ways including stabilizing food webs and regulating sediment resuspension among others. Monitoring estuary productivity at large scales can inform ecosystem scale responses to environmental stressors (climate change, pollution and habitat degradation). Here we use a case study to show how Sentinel-2 data can be used to estimate estuary-wide emerged and submerged gross primary productivity (GPP) on intertidal flats by coupling a new machine learning model to map seagrass and unvegetated habitats with literature-derived photosynthesis-irradiance ($P - I$) relationships. The model consisted of (1) supervised classification with random forest to delineate seagrass and unvegetated areas and (2) artificial neural network (ANN) regression to predict % seagrass coverage. Our seagrass delineation by supervised classification had an overall accuracy of 0.96, while the ANN regression on seagrass coverage provided high predictive accuracy (R^2 = 0.71 and RMSE = 0.11). The estimated GPP showed seagrass contributed slightly more to intertidal benthic productivity than MPB in the case-study estuary over the 3-year study period. This model can be used to predict the response of seagrass and MPB GPP to sea level rise, which shows that the future state may be very sensitive to increased turbidity. For example, by the year 2100, the model shows a sharp decline in productivity with sea level rise, assuming current turbidity trends, (loss of up to 52–53 % for seagrass and 23–45 % for MPB, a function of whether shoreward migration of seagrass is incorporated). However, GPP under conditions of unchanging turbidity (and no seagrass migration), exhibits minimal negative impact of sea level rise (loss of 3 % for seagrass and increase of 29 % for MPB). Therefore, controlling water turbidity might be an efficient solution to maintaining the current GPP as the sea level rises.

3.1 Introduction

Estuaries and shallow coastal lagoons in temperate regions are regarded as one of the most productive marine systems in the world (Heip et al., 1995). In these ecosystems, seagrass meadows and microphytobenthos (MPB) dominate primary production and play important roles in regulating sediment resuspension (Reidenbach and Timmerman, 2019), recycling carbon and nutrients (Duarte et al., 2013) and stabilizing intertidal food webs (Jankowska et al., 2019). Anthropogenic effects accompanied by continuing coastal squeeze in the intertidal have degraded the contribution of seagrass and MPB to ecosystem functioning (Orth et al., 2006). Efforts to manage these effects and restore primary productivity are impeded by a lack of fast-response monitoring data collected at scale.

Estimating the gross primary productivity (GPP) of seagrass and MPB is relevant because it plays a major part in the biogeochemical cycles of intertidal ecosystems (Staehr et al., 2012). GPP is generally modelled as a function of photosynthetically active radiation (PAR) in estuaries dominated by seagrass and MPB (Thrush et al., 2012). In turn, light availability is strongly related to turbidity levels and solar irradiance during submergence and emergence respectively (Miles & Sundbäck, 2000). As fine sediments can be held in suspension for prolonged periods, increased input of terrestrial sediments can increase water-column turbidity and thus reduce seafloor light availability (Mangan et al., 2020). Changes in nutrient supply may also affect primary producers depending on their growth response curves and storage capacities (Grover et al., 1997), and sometimes sensitivity to light and nutrients act in tandem. For example, seagrass is well adapted to oligotrophic environments where turbidity is relatively low because seagrass can take up nutrients from the sediments (Evrard et al., 2005). The actual contribution from seagrass and MPB to the carbon budget in coastal ecosystems is still

relatively unknown, mainly due to the unavailability of GPP estimates at the ecosystem scale (Legge et al., 2020).

As a key indicator of ecosystem functioning, modeling the GPP of the dominant primary producers in an intertidal ecosystem, including spatial and temporal variations at scale, can yield comprehensive insights into responses to different environmental stressors that alter light levels and biomass distribution. Although the loss and migration patterns of seagrass are challenging to observe over large scales without satellite remote sensing (e.g., Short and Neckles, 1999), in situ point measurements of GPP, such as those using benthic chambers (Flowers et al., 2023), diel-change techniques (Miles & Sundbäck, 2000), or eddy covariance techniques (Rodil et al., 2019), provide critical data for extrapolating GPP to whole regions. The heterogeneity of the spatiotemporal distribution of MPB in unvegetated areas also complicates large-scale GPP quantification. However, these in situ measurements, including photosynthetic-irradiance (P-I) curves, are essential for understanding the photosynthetic responses to environmental changes and for developing accurate models of GPP. Such models can enhance our understanding of changes driven by sea level rise and climate change (Hope et al., 2020). Many in situ studies have shown that intertidal vegetation suffers under limited light conditions (e.g., Rullens et al., 2022). Therefore, better maps of GPP for seagrass and MPB at large scales, derived from near real-time satellite data and validated with in situ measurements, would enable a deeper understanding of widespread stressors, such as turbidity and changing light conditions, on food webs. This approach would help identify and characterize shifting production hotspots and at-risk areas of productivity for conservation, thereby forming an effective tool to map the health of estuarine ecosystems.

An efficient tool for monitoring at scale is spaceborne remote sensing, especially open medium resolution (10–100 m) satellite imagery (e.g., Landsat and Sentinel-2). Free and open access of this data means that it represents a cost-effective option for mapping large and continuous changes in seagrass and MPB coverage. The most prevalent technique for evaluating MPB production in unvegetated areas is using the normalized difference vegetation index (NDVI) as a proxy for benthic chlorophyll-a biomass (e.g. Barillé et al., 2011; Daggers et al., 2018; Van der Wal et al., 2008). Difficulties in delineating seagrass using satellites are primarily caused by the lack of a unique spectral signature within the complement of spectral bands of the satellite (Ball et al., 2014). However, these difficulties can be mitigated by employing advanced algorithms. For instance, supervised classification using a maximum likelihood algorithm trained directly on reflectance data is widely used to distinguish seagrass and non-seagrass areas with acceptable accuracy (~60%), after applying radiation calibration and atmospheric correction to the reflectance measurements (Ha et al., 2020). New indices aimed at detecting seagrass from visible-band remote sensing reflectance, such as the depth-invariant index (DII) (Thalib et al., 2018), bottom reflectance index (BRI) (Sagawa et al., 2010), and relative water depth index (RWDI) (Hafizt et al., 2017), provide more accurate results when seagrass is distributed in the subtidal because they reduce the water-column effect on surface reflectance. The use of machine learning (ML) classifiers, such as support vector machines, random forest, and rotation forests, has significantly improved the accuracy of remotely-sensed seagrass mapping to over 85% (Ha et al., 2020; Traganos and Reinartz, 2018b). These ML algorithms benefit from integrating raw spectral information with derived multi-band indices, enhancing their ability to identify important elements in the data. While spectral unmixing algorithms rely heavily on spectral differences and are affected by water column depth, ML algorithms, when combined with additional indices, offer improved classification outcomes. Nevertheless, there is potential for empirical thresholding algorithms that could eliminate the need for ML if

multiple indices are used effectively. Despite the advancements in detecting seagrass extent, only a limited number of studies have explored the potential for estimating vegetation productivity using spectral indices and environmental variables (e.g., Vahtmäe et al., 2021). Therefore, developing algorithms to estimate GPP based on vegetation coverage derived from satellite data would provide substantial insights into the ecosystem state.

The objectives of this study were to develop a novel model to predict the spatial distribution of seagrass and unvegetated flats coverage by combining remote sensing data and machine learning and to use this as a basis for estimating temporal changes to system-wide benthic primary productivity. The study was conducted in a 218 km2 temperate intertidal estuary (Tauranga Harbour, New Zealand). A field survey which recorded the seagrass coverage data was carried out to train the machine learning seagrass coverage model. In this study, we aimed to (1) to fill an important technical gap on how to upscale empirical photosynthesis-irradiance curves, derived from limited sampling information to a spatial distribution map of productivity needed to manage complex heterogeneous estuaries and; (2) show how this technique could be the basis of studies on the drivers of current and future changes to seagrass and MPB GPP.

3.2 Methods and materials

3.2.1 Study area

This study was conducted in the intertidal and shallow subtidal of Tauranga Harbour (Figure 3.1) which has relatively extensive seagrass (*Zostera muelleri*) coverage (22.5 % of the whole Harbour area) and variable benthic light availability associated in part with the semidiurnal

tidal regimes (Mangan et al., 2020; Tay et al., 2011). The remaining seagrass-free intertidal unvegetated areas provide a suitable substrate for MPB to thrive (Morelle et al., 2020). Chlorophyll-a levels in the water column are generally low in the Harbour (0.71–2.23 μg L^{-1}) and trending downwards, thus is currently unlikely to be threatened by excessive phytoplankton blooms and eutrophication (Zygadlo, 2021). Therefore, suspended sediment is the primary factor that controls light attenuation in the Harbour. Annually over 124 t km^{-2} of fine sediments from multiple sources, such as agricultural activities and urban development (Hicks, 2019), are introduced to the Harbour each year (Bricaud et al., 1981; Matheson and Schwarz, 2007), which may reduce benthic primary production and seagrass and limit the depth distribution of seagrass (Pratt et al., 2014; Cussioli et al., 2019).

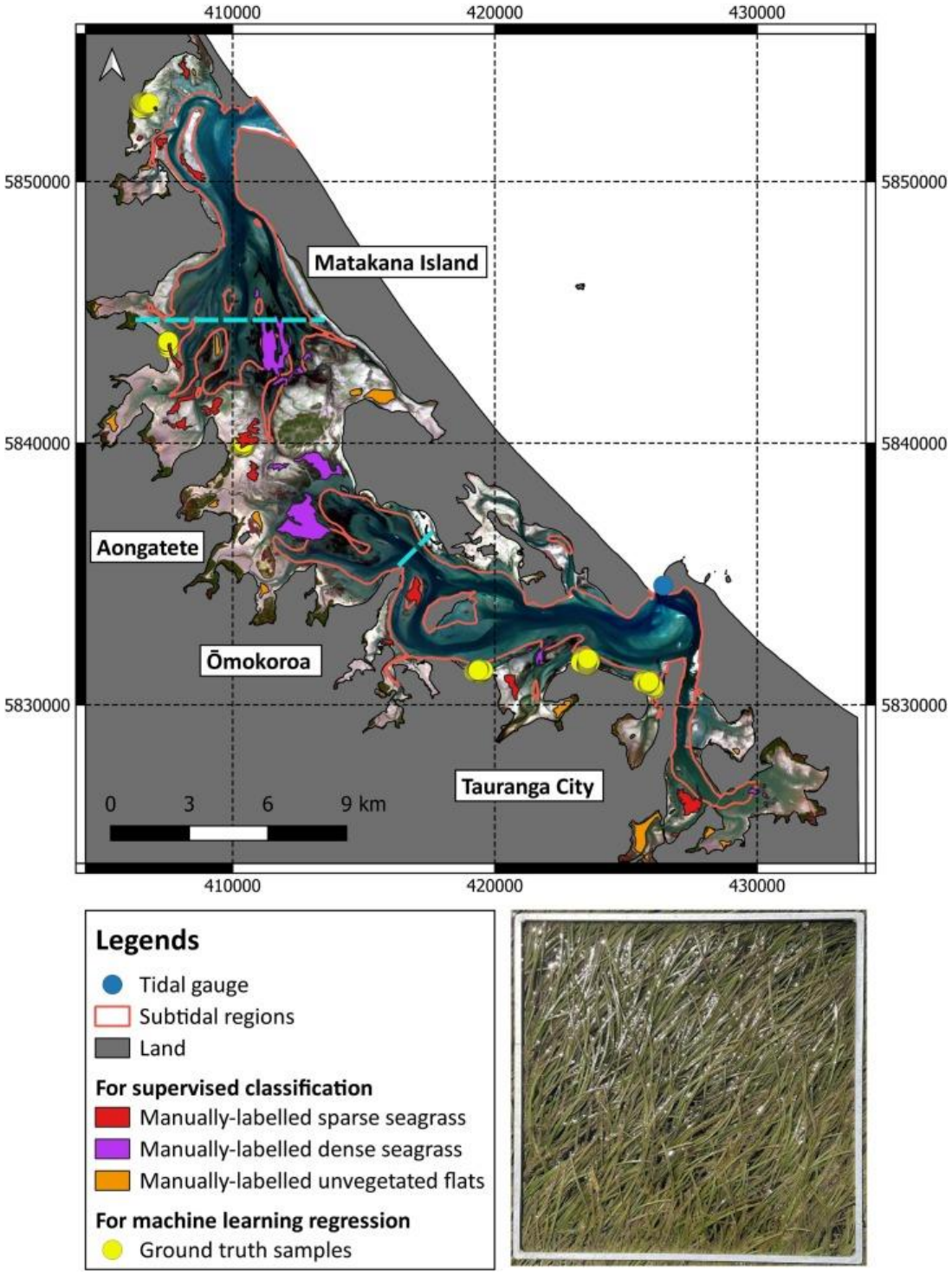

Figure 3. 1 Map of in situ sampling sites with an example of a quadrat photo collected at the Ōmokoroa site (inset). Areas of manually-labelled pixels (coloured regions) used for supervised classification (N = 163,342) and ground truth samples (yellow circles) for machine learning regression (N = 500, collected at 6 sites) in Tauranga Harbour are marked. The light blue dashed lines divide the Harbour arbitrarily into three parts: northern, middle, and southern. The delineation of the subtidal regions is based on tide levels derived from local gauges.

3.2.2 Mapping seagrass coverage and unvegetated area using machine learning

Here we define "seagrass coverage" as the % of an area covered with seagrass, where the area can be a photo quadrat or a remotely sensed pixel (10 m × 10 m resolution for the Sentinel-2 data used for this study). Machine learning and photo quadrats were used to develop an algorithm to convert between the Sentinel-2 images and seagrass % coverage in each pixel. The algorithm was developed in two steps. Firstly, supervised classification based on Sentinel-2 visible and near-infrared bands (Band 2, 3, 4 and 8) using a random forest machine learning classifier was used to detect the presence of seagrass or unvegetated flats. This step used images taken at low tide only (< −0.38 m relative to mean sea level) to avoid biases on machine learning due to light attenuation in water (Sagawa et al., 2008). Secondly, once pixels with seagrass present were identified, the reflectance and indices of pixels from these areas were used in combination with ground-truth data (field survey described below) to finalize the algorithm for predicting percentage seagrass coverage within these pixels. For this, three widely used methods that have achieved high accuracies in estimating coastal vegetation coverage (e.g. Cooper et al., 2019 & Pham et al., 2018) were trialled: artificial neural network (ANN), support vector regression (SVR) and random forest regression (RFR).

3.2.2.1 Required data and pre-processing

An atmospheric corrected Sentinel-2 image (L2A) with low cloud and shadow coverage from low tide on 25th Feb 2022 was selected for supervised classification (Section 3.2.2.2) and to build machine learning models to predict seagrass % coverage (Section 3.2.2.3). Labelled pixels (N = 163,342) were used for supervised classification and were collected by manually digitizing image regions (shown in Figure 3.1) associated with areas of sparse and dense seagrass and unvegetated flats and combined with existing maps from Park (2020).

We also carried out a field survey to collect ground truth points for the % coverage prediction algorithm at the end of the peak summer growth period of seagrass (March 2nd, 2022). The assessments of seagrass % coverage were based on high-resolution photographs of 500 quadrats (0.5 m × 0.5 m) collected along transects at 6 sites at low tide (yellow circles, Figure 3.1). The quadrats were collected over the widest possible spatial range (to maximize the diversity of training data), opting for spacing between quadrats that was greater than the 10 m × 10 m dimensions of the Sentinel-2 pixels. Quadrat locations were chosen in expanses of homogeneous seagrass that were greater than the resolution of Sentinel-2, to maximize the correspondence between the RGB signature and the % coverage. Although when the trained model is applied to detect % coverage in pixels from new images, in particular in sparse seagrass, it is possible that this signature corresponds to either small patches (smaller than the pixel resolution) or genuinely sparse seagrass. Garmin Etrex loggers were used to measure and calibrate the geocoordinates of these samples with an accuracy of 2 m. All seagrass photos were processed by Coral Point Count with Excel extensions (CPCe) software, designed to measure substrate coverage in a picture (Kohler and Gill, 2006), to calculate the seagrass % coverage. The complete machine learning model was later applied to 18 L2A images scanned at low tides from 2019 to 2022 covering different seasons, to assess spatiotemporal variations in seagrass % coverage.

3.2.2.2 Delineating seagrass and unvegetated regions using supervised classification with random forest

Random forest is an ensemble learning method which operates by building a number of decision trees, which is then optimized by comparing the outcomes to the ground-truthing or labelling data (Breiman, 2001). Since the principle of random forest is to average the results across multiple trees, the variance between models is averaged to provide a more robust

prediction (Hastie et al., 2009). In our model, input variables were the reflectance in Sentinel-2 visible bands (Blue R_b, Green R_g, Red R_r) and the near-infrared band (R_{NIR}). R_{NIR} was included to help detect the seagrass in the subtidal regions (Traganos and Reinartz, 2018a, Traganos and Reinartz, 2018b). Each leaf on the decision tree represents the reflectance signature associated with the presence/absence of seagrass, with more detailed trees allowing a greater degree of refinement in the reflectance signatures associated with presence/absence. Datasets were randomly split into training/validation (70 %) and testing (30 %). Fivefold cross-validation was applied to the training/validation portion to obtain the optimum values for hyper-parameters used in the random forest. To assess the model's accuracy when applied to different images, we randomly selected 200 pixels from each of these other images. These additional images were manually labelled in the same way as the training data, and predicted classes were validated using this dataset.

In order to evaluate the performance of supervised classification, four variables were used: accuracy; precision; recall; and F1-score (Equations 1 – 4):

$$\text{Accuracy} = \frac{\text{TP} + \text{TN}}{\text{TP} + \text{TN} + \text{FP} + \text{FN}} \quad (1)$$

$$\text{Precision} = \frac{\text{TP}}{\text{TP} + \text{FP}} \quad (2)$$

$$\text{Recall} = \frac{\text{TP}}{\text{TP} + \text{FN}} \quad (3)$$

$$\text{F1} - \text{score} = \frac{2 \times \text{Recall} \times \text{Precision}}{\text{Recall} + \text{Precision}} \quad (4)$$

where TP, TN, FP, FN are true positive, true negative, false positive and false negative, respectively.

3.2.2.3 Estimating seagrass coverage using machine learning regressions

In the second stage of the modelling, R_b, R_g, R_r, and R_{NIR} from the pixels covered by seagrass were then used to develop machine learning regression models to estimate % coverage. We also included normalized difference vegetation and water index (NDVI & NDWI, Equations 5 & 6) as input data, which has been shown to be sensitive to seagrass coverage (Hossain et al., 2019).

$$\mathrm{NDVI} = \frac{R_{NIR} - R_r}{R_{NIR} + R_r} \tag{5}$$

$$\mathrm{NDWI} = \frac{R_g - R_{NIR}}{R_g + R_{NIR}} \tag{6}$$

Because very few studies have tried to use machine learning to estimate seagrass % coverage based on its spectral properties, we trialled three different techniques (ANN, SVR and RFR) to find the optimal model (using Google Colaboratory and TensorFlow, Scikit-learn and Random Forest Regressor, respectively).

3.2.2.3.1 Artificial neural network (ANN)

The ANN model is a supervised decision-based deep learning technique, which simulates the human brain processes and works as a quantitative predictive model for linear and nonlinear prediction (Yegnanarayana, 2009). The information (reflectance in each band and indexes) from input layers was passed to two hidden layers. In the connections between the hidden layers,

and between the hidden layer and the output layer, weights and activation functions are summed to pass the information through the network. The output layer returned an exact number representing the percentage of seagrass cover in each target pixel. The selection of activation functions, numbers of hidden layers and nodes determine the accuracy of results. However, for most models, two hidden layers can represent an arbitrary decision boundary to arbitrary accuracy with rational activation functions, and thus approximate any smooth mapping to any accuracy (Goodfellow et al., 2017). In the present study, we optimized the activation function, node numbers and learning rates used in the hidden layers. The learning rate is the degree to which the activation function weights are changed between iterations.

3.2.2.3.2 Support vector regression (SVR)

SVR is a supervised learning algorithm used to predict discrete values by training nonlinear system models (Vapnik et al., 1996). Because it is based on a structural risk minimization principle and statistical learning theory, SVR has the potential to provide better performance than ANN under similar training conditions even if the training samples are limited (Kim et al., 2014). Kernel functions are used to separate and transform the input data, and therefore the accuracy of the model is controlled by the choice of kernel function (Mountrakis et al., 2011). In this study, we tested two kernel functions (linear and Gaussian radius bias) at different regularization levels (parameter C) and Gamma to obtain the optimal model.

3.2.2.3.3 Random forest regression (RFR)

RFR is an extension of random forest classification (used in Section 3.2.2.2), which uses the ensemble learning method for regression. Due to using predictions from multiple machine learning algorithms, RFR is highly likely to produce more precise predictions than a single

model (Breiman, 2001). By adjusting the tree numbers, maximum tree depth and minimum number of samples at a leaf node, the most appropriate parameters were set to estimate the seagrass % coverage with reflectance in each visible band.

3.2.2.3.4 Selecting the optimal model

For all three models, we randomly selected 80 % of the data for training, 10 % for validating and the remaining 10 % for testing. The loss function, mean square error (MSE) (Equation 7) and coefficient of determination (R^2), were used to determine the optimum parameters for each model using the training and validation data. The overall fit was evaluated by comparing the root mean square error (RMSE) (Equation 8) and R^2 of predicted and observed seagrass percentage cover using the testing data.

$$\mathrm{MSE} = \frac{1}{n}\sum_{i=1}^{n}\left(X_{obs} - X_{pre}\right)^2 \tag{7}$$

$$\mathrm{RMSE} = \sqrt{\frac{1}{n}\sum_{i=1}^{n}\left(X_{obs} - X_{pre}\right)} \tag{8}$$

where X_{obs} is the observed seagrass % coverage and X_{pre} is the predicted % coverage. In order to evaluate the model's performance on the different dates, we compared the model derived results with published seagrass % coverage data collected at different dates in the same estuary (Flowers et al., 2023; Park, 2020).

3.2.3 Modelling gross primary productivity in Tauranga Harbour

In order to model the GPP of seagrass and MPB in Tauranga Harbour, we used published *in situ* relationships between rates of photosynthesis and light (*P – I* relationships). We assumed that seagrass and MPB were the only two benthic primary producers in the intertidal region and that their production is more limited by light than by, for example, temperature or nutrients. Adding on a literature-derived temperature dependence would not likely increase the difference between summer and winter productivity substantially because the annual air/water temperature variations (16 ~ 23 ℃) are not enough to have significant effects on GPP (Flowers et al., 2023). Therefore, ignoring temperature in this case study would not add further understanding of the spatial complexities and scaling that we aim to demonstrate here.

GPP calculated using *P – I* relationships was scaled by estimated proxies of seagrass or MPB biomass. For seagrass, the modelled GPP at each pixel was scaled by the % coverage derived from machine learning as an indicator of productive biomass. Seagrass % coverage was mapped for each image in the collection, and so changed with season. MPB was assumed to occupy all the pixels where no seagrass was detected (unvegetated areas) and the pixels where seagrass occurred but did not cover the entire pixel, in which case MPB occupied the remaining fraction of the pixel. In those areas, MPB GPP was scaled by the estimated chlorophyll-a concentration within that pixel; chlorophyll-a has been shown in many studies to be a good indicator of MPB biomass in estuaries (Jacobs et al., 2021). A significant empirical linear regression between *in situ* chlorophyll-a measurements and satellite-derived NDVI was used to produce a Harbour-wide map of chlorophyll-a from NDVI (see Supplementary material 1).

The photosynthetic response (P, μmol C m^{-2} h^{-1}) of seagrass and MPB to variation in light intensity (I) was modelled using (Equation 9) (Webb et al., 1974):

$$P = P_{max}\left(1 - e^{-\frac{\alpha I}{P_{max}}}\right) \quad (9)$$

where α is the initial slope and P_{max} (μmol C m^{-2} h^{-1}) is the maximum potential photosynthetic rate for each species. α and P_{max} may vary depending on whether the habitat is submerged or emerged (Flowers et al., 2023). When submerged, the diffuse attenuation coefficient for photosynthetically active radiation ($K_{d\,PAR}$) and light intensity (I_0) at the water surface control the amount of light absorbed at a specific depth (z) (Equation 10). Light intensity data were derived from hourly measurements at Tauranga Airport (downloaded from the CliFlo data portal https://cliflo.niwa.co.nz/) and were used in calculations of productivity. Tidal levels extracted from local tide gauges (see Figure 3.1) and a digital elevation model, created by combining airborne LiDAR data and single and multibeam data collected by the Port of Tauranga, were used to calculate the water depth at each pixel in the Sentinel-2 images. Water depth helps to distinguish tidal zones and whether a pixel is emerged or submerged at the time of image acquisition.

$$I = I_0 e^{-k_{d\,PAR}\,z} \quad (10)$$

Although there is no direct method to measure $K_{d\,PAR}$ using satellite reflectance, Shao et al. (2022) tested empirical linear regressions between $K_{d\,PAR}$ and K_d associated with blue light, which was derived from an application of Lyzenga's model (Lyzenga, 1981) to reflectance measured in shallow water. This method was used to extract $K_{d\,PAR}$ from the Sentinel-2 imagery.

Data from Flowers et al. (2023) was used to parameterise Equation 9, and to derive a relationship to scale seagrass GPP by % seagrass coverage and MPB GPP by sediment chlorophyll-a concentration. Flowers et al. (2023) evaluated the P_{max} and α for both seagrass

and MPB-dominated habitats in Tauranga Harbour seasonally over two years by measuring changes in GPP as a function of light intensity using benthic chambers during submerged and emerged periods (Table 1). Although both P_{max} and α varied somewhat between sample dates we used the seasonally averaged values which provided a very good fit to the empirical data assuming they were applicable to all regions of the Harbour.

Table 3. 1 In situ measured seasonally averaged (± 1 SD) P_{max} and α for seagrass and MPB at emergence (n= 7 sampling events over two years) and submergence from Flowers et al. (2023).

	Seagrass		**Sandflat**	
	Submerged	**Emerged**	**Submerged**	**Emerged**
P_{max}	6240 ± 540	4519 ± 418	3485 ± 484	1194 ± 98
α	32.4 ± 5.1	22.5 ± 6.2	13.5 ± 2.7	8.0 ± 3.0

P_{max} – photosynthetic maximum (μmol C m^{-2} h^{-1}), α – photosynthetic efficiency μmol C m^{-2} h^{-1} (μmol photons m^{-2} s^{-1}) $^{-1}$.

To account for the spatial/temporal variations in % seagrass coverage and chlorophyll-a content derived from the satellite images we used empirically derived relationships to adjust P_{max} for changes in primary producer biomass. Using previously published data we fitted quantile regressions (90th percentile; Q90) to measurements of GPP and primary producer biomass (see Supplementary material S2):

$$P_{max\ seagrass} = \begin{cases} 54.8 \times SGC + 2372.0\ (Submerged) \\ 119.5 \times SGC - 1298.5\ \ (Emerged) \end{cases} \quad (11)$$

$$P_{max\ MPB} = \begin{cases} 30.4 \times Chla + 2086.5 & (Submerged) \\ 1574.0 & (Emerged) \end{cases} \quad (12)$$

where SGC is % seagrass coverage and Chla is chlorophyll-a concentration. Equations 11 and 12 were then used together with Equations 9 and 10 to upscale GPP to the whole Harbour. Other factors including light, temperature, macrofauna activity etc contributed to the variability of GPP under the Q90 lines (Figure S2). For the Q90 relationships between GPP and chlorophyll-a, additional published measurements were added to increase degrees of freedom (Pratt et al., 2014; Flowers et al., 2023; Mangan et al., 2020). The relationship between emerged MPB GPP and chlorophyll-a was not significant, so was set as the 90th percentile of all emerged treatments. GPP in seagrass treatments was corrected for the contribution of MPB prior to fitting the Q90 regression. Note that to accommodate self-shading at high % seagrass coverage (e.g. Carstensen et al., 2016; Clavier et al., 2011), we assumed that P_{max} remained constant when the seagrass coverage was over 80% (mainly in the subtidal areas) but neglected the effect of seagrass shading on MPB productivity. The seagrass canopy (*Zostera muelleri*) is short and thin in New Zealand (10 cm in length and 0.1~ 0.4 cm in width, Morrison et al., 2014) and % seagrass coverage over 80% was very rare (see Results and Figure S3), and so neglecting the effect of shading of seagrass on MPB was unlikely to introduce significant errors to the results.

In Equation 10, I_o and z vary a lot with time (due to tide, season and weather), whereas $K_{d\ PAR}$ does not vary substantially within one season (Shao et al., 2023). In addition, Sentinel-2 image availability limited satellite-derived information to longer timescales. A flow diagram showing the steps which were taken to develop maps of productivity is shown in Figure 2.

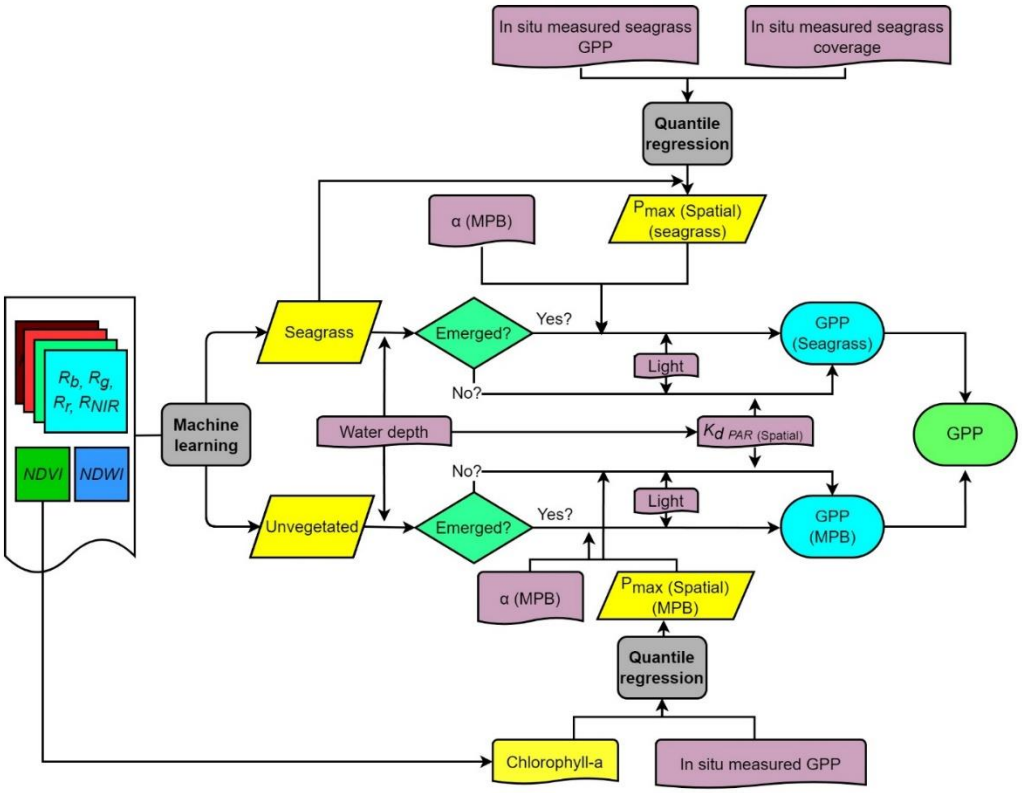

Figure 3. 2 The flow chart showing how the GPP of seagrass and MPB were calculated after the seagrass and MPB coverage maps were obtained by image classification.

3.2.4 Predicting the GPP responses of seagrass and MPB to climate-related stressors

The spatially-resolved GPP model can be used to explore future pathways, which we highlight by examining changes that might occur with sea level rise. Although the impact of sea level rise and climate change will be site-specific (Oppenheimer & Hinkel, 2018), projections indicate that a substantial rise in turbidity is likely, due to more frequent severe storms/floods and extra coastal erosion, which both deliver more fine sediment to the estuary and enhances sediment resuspension within the estuary increasing K_d (Björk et al., 2008; Heyes et al., 2004). Here we established a response model to simulate the changes of intertidal GPP associated with sea level rise and accompanying turbidity changes (Scenario 1-present day turbidity;

Scenario 2-increasing turbidity). The distribution of seagrass and MPB were initially assumed to remain the same, but z and K_d (Equation 10) are adjusted using the New Zealand Representative Concentration Pathways (NZ RCP 8.5, 1.1 m sea level rises by 2100) (Van Vuuren et al., 2011) and nominal linear increase in light attenuation (K_d increased 0.37 m^{-1} per 25 cm sea level rise). Projected changes to K_d were derived from global potential trends reported in the literature, and transformed from total suspended solid concentration (Davis et al., 2016; Ogston & Field, 2010; Pitarch et al., 2021). We also trialled a version (Scenario 3) in which seagrass was allowed to migrate to more suitable areas. To determine future suitable areas, the relationship between current average seabed light intensity and current seagrass coverage was used. MPB was assumed to occupy the area unoccupied by seagrass after migration. The current relationship between average seabed light intensity and chlorophyll-a distribution was used to scale MPB GPP in its new location (see Supplementary material S3 and Figure S4 for more details). Although the GPP response model is highly simplified, it can be used to inform more detailed studies (such as to identify key parameters or areas of particular sensitivity).

3.3 Results

3.3.1 Performance of machine learning methods

The supervised classification of seagrass presence/absence using random forest reproduced the verification data with high precision (>0.85) and confidence (F1-Score > 0.89) with optimized settings for hyper-parameters (Table 2). The selected values for hyper-parameters including the number of trees, minimum sample split, minimum sample leaf and maximum tree depth were 280, 4, 4 and 9, respectively. The model returned the highest precision (0.97) in predicting dense seagrass due to its distinct spectral signatures. The precision for sparse seagrass regions

was slightly lower because of its similarity to bare sediments, especially when the seagrass coverage ratio is extremely low and in very shallow water. To assess the model's accuracy when applied to the remaining images, we randomly selected 200 pixels from each of these other images. These additional images were manually labelled in the same way as the training images, and predicted classes were validated using this dataset. The outcomes demonstrated that despite being trained on data from a single day, the model achieved good accuracy when applied to other images.

Table 3. 2 Performance results of supervised classification with random forest for different habitat classes based on the image scanned on 25th Feb 2022 and all remaining images.

Scanning date	Class	Overall accuracy	Accuracy	Precision	Recall	F1-Score	Support (Sample numbers)
25 Feb 22	Sparse seagrass	0.96	0.91	0.86	0.91	0.89	20912
	Dense seagrass		0.98	0.97	0.97	0.97	32301
	Unvegetated flats		0.93	0.92	0.94	0.93	16178
Rest	Sparse seagrass	0.88	0.81	0.78	0.81	0.80	1085
	Dense seagrass		0.92	0.89	0.88	0.91	1676
	Unvegetated flats		0.84	0.83	0.85	0.82	839

The optimum values of hyper-parameters for each machine learning regression developed to predict seagrass coverage (% cover) were confirmed by comparing the MSE and R2 values of

validation datasets. (Table 3.3). After each regression model had the optimal parameters, the best technique from the three methods to predict the seagrass coverage was then determined by comparing the performance of the three models when applied to the testing dataset (Figure 3.3).

Table 3. 3 The optimum values of hyper-parameters were selected for ANN, SVR and RFR.

Model	Hyper-parameters	Optimum values	Validations	
			MSE	R^2
ANN	Activation function	Rectified linear unit (Relu)	0.023	0.625
	Number of hidden layers	2		
	Number of neurons	10		
	Learning rate	0.01		
SVR	Kernel function	Radial basis function (rbf)	0.024	0.612
	Gamma	0.1		
	C	13		
RFR	Number of estimators	20	0.021	0.644
	Max depth	10		
	Min samples leaf	1		
	Min samples split	4		

Both the ANN and SVR models provided precise results with high correlations (R^2 = 0.711 & 0.723) and low RMSE (0.111 & 0.126) between measured and predicted data (Figure 3.3). The lowest performance was observed for RFR with the R^2 value and RMSE of 0.709 and 0.129, respectively (Figure 3.3). Considering the minimum detectable threshold was 9 % with ANN (compared to 16 % with SVR and 7 % with RFR) and also considering other performance statistics (Table 3.3), we selected the ANN regression to predict the seagrass coverage in

regions classified as having seagrass present in Tauranga Harbour. When the ANN regression was applied to other images, the estimated seagrass coverage was consistent with the values collected in the field (Figure 3.3d). This good performance (R^2 = 0.69 & RMSE = 0.06) indicated that the ANN model was appropriate for predicting % seagrass coverage of the Harbour.

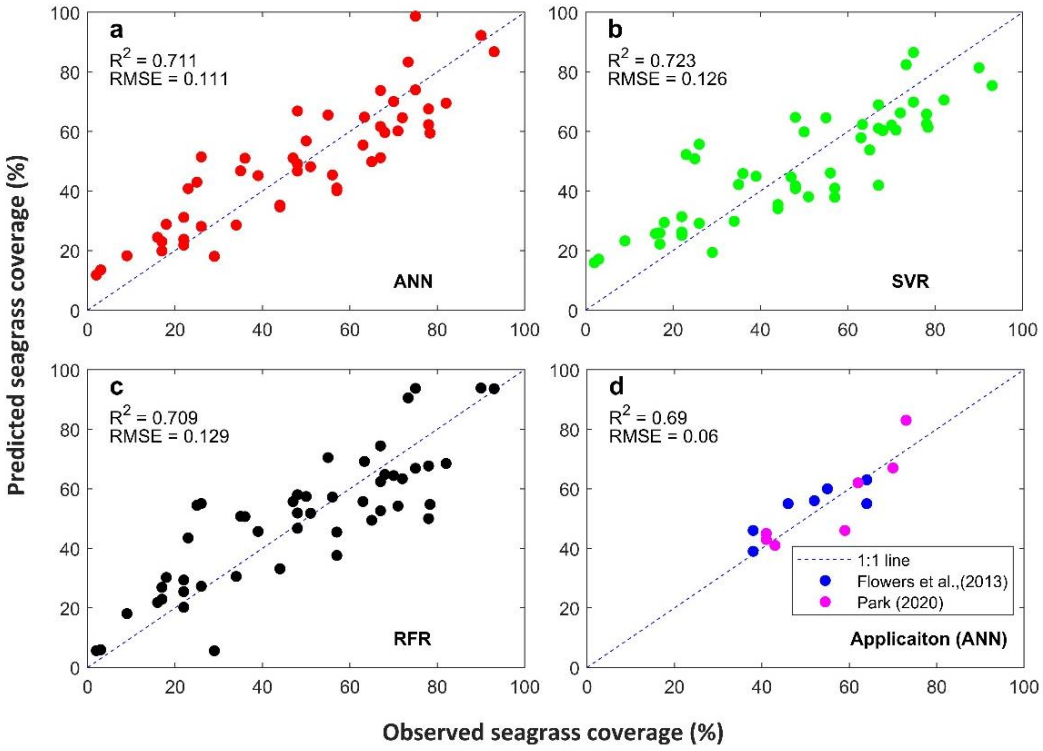

Figure 3. 3 Comparisons of in situ measured and predicted seagrass coverage derived from the (a) ANN, (b) SVR and (c) RFR and (d) accuracy assessment when the ANN model derived estimate was compared to in situ measurements (Flowers et al., 2023; Park, 2020).

3.3.2 Seagrass and unvegetated tidal flat distribution

The classification map derived from the random forest method showed that sparse seagrass, dense seagrass and unvegetated flats respectively occupied 10.5, 15.3, and 16.7 % of the area of the whole Harbour (Figure 3.4b). It also showed large seagrass meadows, especially in the middle of Tauranga Harbour where dense seagrass thrived (Figure 3.4b). Additionally, the

classified map indicated high-coverage seagrass thriving in shallow subtidal areas. These thriving areas were also well represented in *in situ* samples from the field survey (Figure 3.1). Sparse seagrass was mainly distributed in the mid-intertidal.

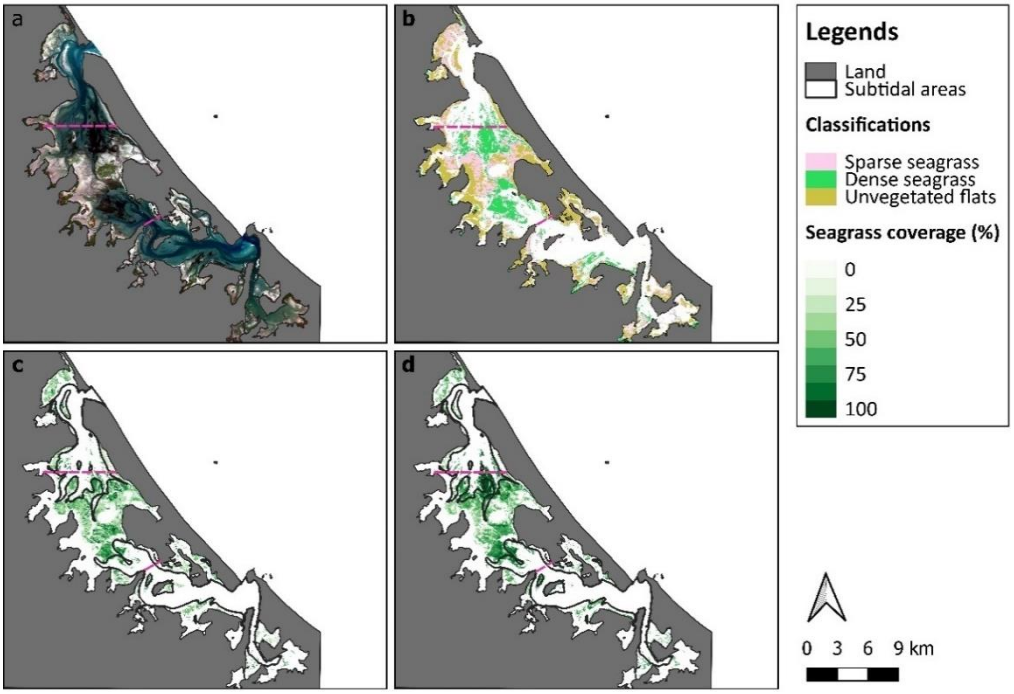

Figure 3. 4 The maps of (a) original satellite data from Feb 24, 2022 at low tide; (b) spatial distribution of dense seagrass, sparse seagrass and unvegetated flats after classification using random forest; and seasonal variations in seagrass coverage in winter (c) and summer (d) after regression using ANN. The data were derived from images taken on Aug 3rd 2021 (c) and Feb 24th 2022 (b & d). The magenta dashed lines arbitrarily divide the Harbour into three parts: northern, middle, and southern.

The extracted seagrass % coverage maps, trained using ANN, provided more detailed spatiotemporal changes in both the subtidal and the intertidal between summer and winter (example shown in Figure 3.4c & d). At the end of summer, although the area where seagrass grew in the subtidal regions was small, the seagrass % coverage in these regions reached the highest (over 70 %) of the whole Harbour. Most of the thriving seagrass meadows were distributed in the middle Harbour and % coverage declined from subtidal/intertidal areas

toward the coastline (Figure 3.4d). The northern Harbour had a greater area of seagrass (245.7 ha and the % coverage was higher (by 10 %) than in the southern Harbour. In winter, the seagrass area tended to decrease to a minimum, especially in the middle of the Harbour, likely due to restricted photosynthesis at lower light levels. Although seagrass still existed in winter in the other regions of the Harbour, the % coverage was significantly lower than in summer (by at least 10 %).

Although both classification (presence/absence) and regression (% coverage) methods are of similar utility for understanding seagrass trends, the regression method is likely to yield more precise results due to its capacity to provide sub-pixel detail on coverage (Figure 3.5a & b). In the case of classification, the seagrass area is calculated by simply adding the pixels occupied by seagrass (adding dense and sparse classes together) and multiplying this number by pixel area (Figure 3.5b). In the case of regression, the seagrass area in each pixel is calculated using the % cover, and then the area of seagrass of all pixels is summed (Figure 3.5a). In both cases, the area unoccupied by seagrass is allocated to unvegetated (MPB occupied area). The seasonal statistics derived from the % coverage (Figure 3.5a) and the presence/absence models (Figure 3.5b) show comparable interannual variations of the seagrass and unvegetated area over three years where imagery was available. The sum of the intertidal and subtidal seagrass area reached the minimum (1296 ha) in spring 2019, after which an increasing trend occurred (Figure 3.5a). From 2019 to 2022, the seagrass area (inter- and subtidal) recorded its largest expansion (493 ha) between Spring 2021 and Summer 2022. The interannual patterns of change were also evident in the data derived only using supervised classification (so not incorporating within-pixel coverage) (Figure 3.5b) while the changes for unvegetated flats were generally opposed. Note that the subtidal seagrass area (shown as a separate line) also varies substantially from year to year, and is particularly large in spring 2019 (Figure 3.5a& b).

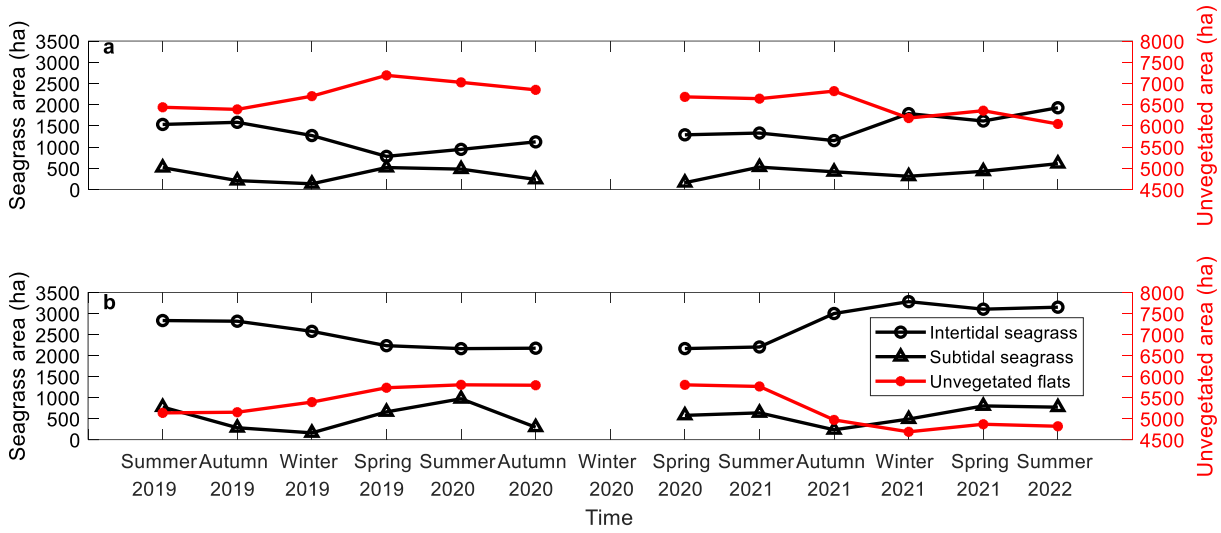

Figure 3. 5 The extent of seagrass and unvegetated flats in the intertidal regions of Tauranga Harbour from 2019 to 2022, as determined by the % coverage map (a) and supervised classification map (where dense and spare were amalgamated) (b). In a, the fraction of pixel area occupied by seagrass is calculated and then summed over all pixels and in b the number of pixels occupied by seagrass are summed and then multiplied by the area of a pixel. Winter 2020 was not present due to the unavailability of good-quality remote sensing images in this season. Note that although unvegetated and intertidal seagrass are evaluated over the same intertidal area, subtidal seagrass is evaluated separately.

3.3.3 Gross primary production of seagrass and MPB

The maps of GPP for seagrass in the Harbour showed spatial clusters (hotspots) and strong variations with time consistent with the coverage maps. These hotspots were mainly distributed in the subtidal regions of the middle Harbour and surrounding intertidal areas where the GPP values reached the highest (1.25–1.58 g C m^{-2} d^{-1}) in summer (Figure 3.6b). A clear decline in productivity from hotspots to upper intertidal regions occurred. This decline ended in the supratidal regions where seagrass did not grow or in turbid shallow water where intolerably high $K_{d\ PAR}$ values occurred and thus limited light availability. Compared with the northern and middle Harbour, the southern Harbour contributed the least to productivity due to limited seagrass distribution in both winter and summer (Figure 3.6a & b). The distribution of GPP in the Harbour mainly corresponded to the coverage of seagrass (Figure 3.4).

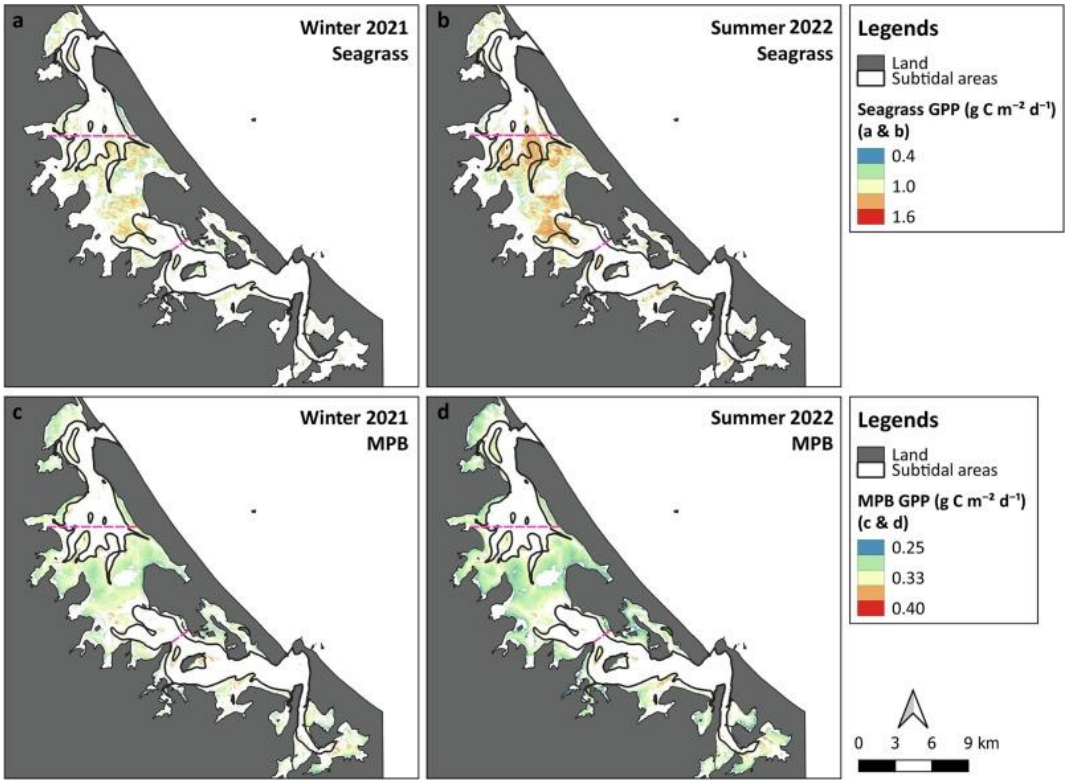

Figure 3. 6 The spatial distribution of seagrass (a and b) and MPB (c and d) GPP in winter and summer, respectively. The magenta dashed lines divide the Harbour into three parts: northern, middle, and southern.

In the large unvegetated intertidal areas, MPB GPP was much less productive than seagrass. The productivity declined shoreward as the probability of exposure increased (lower P_{max} when emerged, Equation 12). The MPB GPP usually declined to a minimum (0.24 g C m^{-2} d^{-1}), which generally occurred in the regions where seagrass thrived (e.g. middle Harbour). The maximum MPB GPP was observed in the lower intertidal regions close to the middle Harbour and the southern Harbour (Figure 3.6c & d). These regions usually had the highest chlorophyll-a concentrations and relatively low elevations which means MPB was submerged for longer and P_{max} would be significantly higher than that when emerged.

The dominant contributor to the total GPP in Tauranga Harbour depended on location and season. Between winter 2019 and autumn 2020 (also autumn 2021), both seagrass and MPB

contributed similar amounts to the entire Harbour productivity (Figure 3.7a) In the remaining seasons, seagrass contributed the highest productivity (56–65 %). In terms of location, the middle region was the most productive in the Harbour (accounting for 62 % ~ 66 %) due to its high coverage of seagrass (Figure 3.7b). Seagrass and MPB took turns to become the dominant contributor in the northern Harbour (Table 3.4). In the middle Harbour, seagrass was the dominant contributor, and exhibited minimal seasonality (Table 3.4). Conversely, MPB GPP derived for the southern Harbour was highest (52–64 %) due to fairly large unvegetated sandflats in these regions (Figure 3.4). In general, the GPP of the entire Tauranga Harbour had a clear seasonal spatial variation.

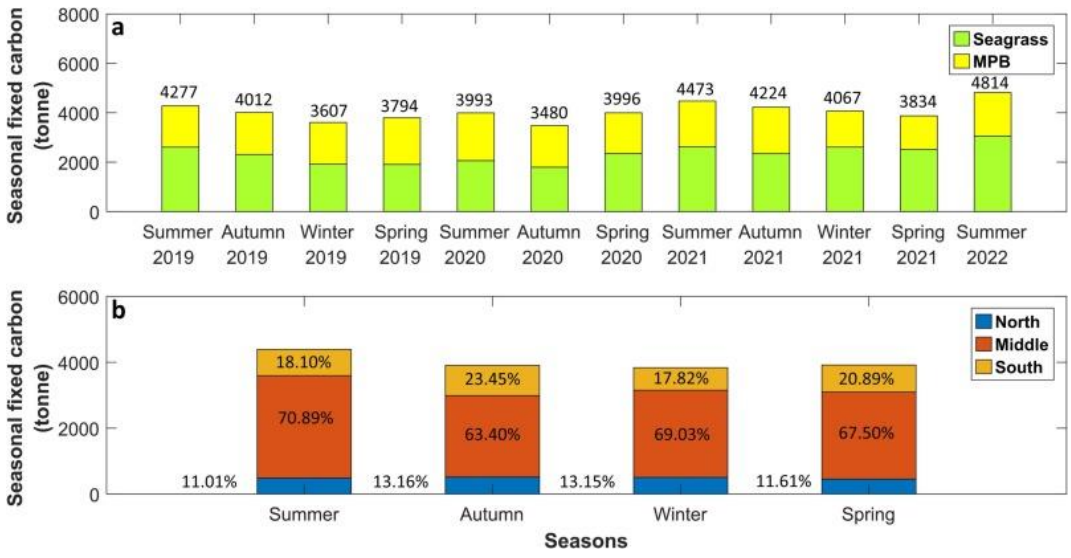

Figure 3. 7 The variation of productivity (fixed carbon) with season from 2019 to 2022. (a) The averaged contributions to the entire Harbour from seagrass and MPB (b) and from the northern, middle and southern Harbour.

3.3.4 Future responses of seagrass and MPB

The response model shows how the Harbour-wide productivity estimates could alter with changes in turbidity and water depth. Assuming no migration of seagrass the response models show that with just sea level rise (Scenario 1, Figure 3.8) MPB productivity could be enhanced

(by 31 %) and barely impacts seagrass GPP (− 2.2 %). The increase in MPB GPP with sea level rise is because productivity increases substantially when it spends less time emerging (Flowers et al., 2023). With sea level rise and increased turbidity (Scenario 2) MPB GPP initially increased until it was submerged too much of the time, triggering a decline in GPP due to the increased turbidity and decreasing seafloor light sea levels rise (Figure 3.8). Unlike MPB, seagrass GPP was predicted to drop substantially (−51 %) by the year 2100 which meant they would no longer dominate Harbour GPP even in summer. However, the potential migration of seagrass habitat as sea level rises along with increased turbidity can cause a big difference in predicted productivity, particularly for seagrass (Scenario 3, Figure 3.8). Seagrass initially shows a rapid increase in productivity as it migrates shoreward to the present upper intertidal area, which was previously occupied by MPB reducing MPB production (relative to the case with no migration). Nevertheless, MPB still maintained a slow increase in their GPP despite the expansion of seagrass. This was because the elevated productivity associated with the additional time MPB was submerged compensated for the smaller habitats. As sea level continues to rise, turbidity and water depth restrict light availability substantially, the productivity of both seagrass and MPB will suffer a decline by the end of this century.

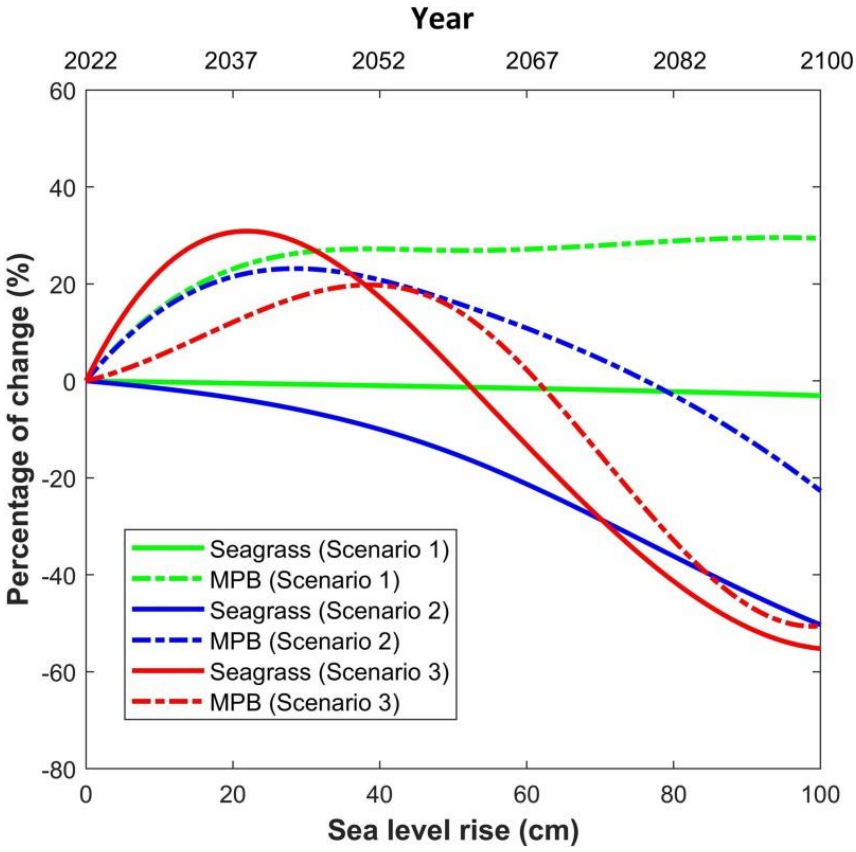

Figure 3. 8 The relationships between the sea level rise (year) and the rate of change of seasonally fixed carbon from seagrass and MPB without (Scenario 1) and with increasing turbidity (Scenario 2) and with allowing expansion of seagrass meadows (and including the effect of varying turbidity) (Scenario 3).

3.4 Discussion

In this study, we demonstrate how seagrass coverage derived using machine learning and remote sensing can be used as a basis for estimates of seagrass and MPB GPP over large complex estuarine systems. With the use of remote sensing imagery, this model can identify productivity hotspots in inaccessible areas, deal with patchy environments and upscale the results from sparse *in situ* measurements to create broad-scale assessments. By using these detailed seagrass coverage maps with a locally-informed $P - I$ model, and changing the environmental parameters in the model (i.e. light intensity, light attenuation, water depth), GPP distribution can be predicted and used to project the potential impact of future responses to

environmental conditions (e.g. turbidity changes and sea level rise) by changing diffuse attenuation coefficients and water depth. In addition, by retraining the classification on other input spectral information, this model could be extended to detect other types of seagrass (e.g. Thalassia, Syringodium and Halodule) in other estuaries and/or for different seasons because of their different reflectance in red and NIR bands (Thorhaug et al., 2007). Therefore, the spatial GPP results provided by this model can underpin management actions aimed at, for example, selecting sites for restoration in the intertidal or monitoring the general health status of vegetation in estuaries and potentially as a basis for understanding changes to blue carbon storage. In Tauranga Harbour, restoring seagrass to all intertidal areas of the Harbour to achieve the same GPP as the middle Harbour could potentially result in a twofold rise in the amount of carbon fixed by the Harbour.

Although machine learning techniques have been used to detect presence/absence in previous studies, here we extend these techniques to estimating percentage coverage, producing promisingly accurate spatially-resolved seagrass distribution results. Supervised classification using random forest provided an overall accuracy of 0.96 (Table 3.2), which was substantially higher than using maximum likelihood, support vector machine or convolution neural network (e.g. Ha et al., 2021a; Scarpetta et al., 2022). This is likely because random forest can maintain accuracy by automatically estimating missing data and balancing the errors from biased classes (Breiman, 2001). For % coverage prediction, all three models returned relatively good results although RFR performed the least well compared to ANN or SVR when the % coverage is low (the % coverage values around 0.29 decreased the accuracy) (Figure 3.4). Due to the introduction of % coverage, the seagrass area derived from this model is more nuanced, allowing the characterisation of small seagrass growth hotspots relative to the direct use of supervised classification (Ha et al., 2021). Although subtidal training data were not collected

for seagrass coverage and high attenuation could potentially change the spectral information of submerged seagrass, the accuracy of subtidal estimates was confirmed (the difference was −4.8 ± 9.1 %) by comparing intertidal seagrass detected at mid-tide (when submerged) and low tide (when emerged) using images from adjacent dates (Figure S5). Tauranga Harbour has very little subtidal seagrass, and the existing subtidal seagrass is mostly distributed in shallow water. Therefore, errors arising from water column effects are unlikely to significantly impact the results.

The machine learning derived estimates of seagrass and MPB GPP were relatively consistent with the literature. Our seasonally averaged seagrass GPP (1.52 ± 0.14 g C m^{-2} d^{-1}, estimated from Figure 5a & 7) was similar to *in situ* measurements (0.64–1.87 g C m^{-2} d^{-1}, transformed from hourly measurements) collected in 3 estuaries across New Zealand (Bulmer et al., 2018). Globally, our values also correspond to the estimates generated from similar temperate environments (0.9–1.28 g C m^{-2} d^{-1}; Erftemeijer et al., 1993; Moriarty et al., 1985). At an annual scale, the unvegetated flat GPP we estimate was 105 ± 9 g C m^{-2} $year^{-1}$, similar to that calculated by Migné et al. (2004) (110 g C m^{-2} $year^{-1}$) and close to the range reported by Méléder et al. (2020) (3.7–94 g C m^{-2} $year^{-1}$). Generally, MPB GPP in the harbour (0.27–0.31 g C m^{-2} d^{-1}) was somewhat higher than other sites in Europe (e.g. 0.08–0.11 g C m^{-2} d^{-1}, Jacobs et al., 2021) but the latter estuaries are muddier and likely more turbid than in New Zealand, which could significantly restrict the primary production (Douglas et al., 2018).

The GPP model developed in this study is useful to determine the dominant primary producer in the Harbour, and to investigate the potential contributing factors to the existing hotspots. The P_{max} values for MPB were lower than those of seagrass during both tidal states (submerged and emerged), and in both habitats, P_{max} was lower during emergence (Flowers et al., 2023). Season and location are the two main factors controlling the spatial distribution of intertidal

GPP. Seagrass was more likely to dominate the gross primary production in the whole Harbour in warm seasons and its dominance is trending upward in recent years due to its higher P_{max} and expanding areal distribution (even now extending to subtidal areas) (Crawshaw et al., 2023). The expansion is likely because Tauranga Harbour water temperatures have been increasing in winter which would increase the growth of seagrass (Lee et al., 2007) even though temperature is not included in our model, temperature would correlate with reduced light intensity in winter and spatial patterns are likely driven by variations in light availability caused by emergence/submergence time and turbidity (Gattuso et al., 2006).

Upscaling from *in situ* measurements, the model neglects a number of ecophysiological adaptations in both seagrass and MPB as well as their interactions with the surrounding environment (Keyzer et al., 2020; Repolho et al., 2017). For example, seagrass has morphological plasticity as an adaptation to limited light conditions (i.e. changes in pigment compositions, Davey et al. (2018) and Ferguson et al., 2016) and chronic temperature increases (i.e. reductions in leaf and shoot coverage, York et al. (2013)). Seagrass has the capacity to up-regulate productivity to compensate for insufficient GPP during submergence while MPB does not possess this feature (Drylie et al., 2018). Neglecting these effects is likely to result in an underestimation of the seagrass GPP. However, considering that Tauranga Harbour currently remains relatively stable with respect to turbidity and temperature, most seagrass and MPB receive sufficient light for photosynthesis. Therefore, the missing GPP is not expected to significantly alter the overall GPP values.

The GPP model can provide some insight into the potential impact of sea level rise and climate change on the current seagrass and MPB GPP distribution (Figure 3.8 and Figure S6). Obviously, such a simple model neglects many effects such as changes to hydrodynamic conditions, morphology and potential habitat gains and losses. Nevertheless, the model can

highlight hotspots that are expected to experience a substantial decline in GPP due to sea level rise and climate change (such as the middle Harbour, Figure S6). The future GPP distribution maps suggest that seagrass and MPB might migrate shoreward to access improved light conditions (Figure S6), as shown in other studies (Short and Neckles, 1999). Indeed, when we allowed the seagrass in the model to migrate to better light conditions, seagrass productivity was enhanced. Our model highlights the important role of future turbidity changes on rates of GPP, although in reality, resuspended sediments caused by storms in the future may make it difficult to detect trends caused by sea level rise (Pu et al., 2014). The model projections suggest that the soft sediment ecosystems in Tauranga (consisting of seagrass and MPB) were highly sensitive to changes in turbidity, as are many low-nutrient/high light systems (Pratt et al., 2014). Such behaviour is an example of the non-linear feedback that drives environmental conditions in estuaries. For example, our higher-turbidity projections show stable MPB productivity for a long period of time, but ultimately a decline after 60 years (Scenario 2, Figure 3.8), showing how the dependency between water depth and turbidity can show rapid changes over short time frames. Although the model only includes changing turbidity, turbidity inputs in Tauranga are associated with the introduction of nutrients, generally occurring during high catchment run-off winter months (Tay et al., 2011). This highlights the complex relationship between turbidity and nutrients that often occur in estuaries, where turbidity changes could trigger a cascade of ecological impacts. Although the reduced turbidity scenario clearly shows better outcomes for seagrass and MPB productivity, reduced turbidity would be associated with reduced nutrient loading (Statham, 2012), and therefore may ultimately limit productivity in a low-nutrient environment like Tauranga Harbour.

The model presented in this study shows how a large-scale, rapid, and relatively precise assessment of the gross primary productivity (GPP) of the dominant primary producer species

can be undertaken in an intertidal estuary using remotely-sensed information. The model has many simplifying assumptions, for example, that literature-derived parameters of $P - I$ curves are consistent everywhere in the Harbour and productivity scales with % coverage (seagrass) and chlorophyll-a (MPB) with no sensitivity to other environmental factors. In a future study, more drivers could be included in the model to improve the accuracy of prediction like temperature (positively affects metabolic rates), salinity (impacts the osmotic pressure in the cells), oxygen (supplies metabolism) and nitrogen and phosphorous (necessary nutrients), all of which will contribute to productivity (Pratt et al., 2014).

3.5 Conclusion

In this study, we show how freely available remote sensing information and machine learning can be used as a basis of a model to estimate the seagrass distribution and coverage, which in turn was used as a basis for designing a spatially-resolved GPP model. Compared to the *in situ* measurements, the seagrass coverage was accurately predicted ($R^2 = 0.71$, RMSE = 0.111). By referencing the $P - I$ curves for seagrass and MPB, this model was extended to provide a spatial map of GPP with the input of water depth, solar irradiance and $K_{d\,PAR}$. We show the utility of our model by applying it to a complex case-study estuary (Tauranga Harbour) and found that the dominant contributor to the GPP in the entire Harbour depends on both location and season. Projections using this simple model describe how sea level rise and climate change might affect the dominant role of seagrass within this estuary as a result of increasing turbidity. As such, for Tauranga Harbour, controlling water turbidity will be critical to prevent losses of GPP from sea level rise and climate change.

Supplementary materials

S1 Estimating MPB chlorophyll-a concentration

Previous studies indicated that NDVI (normalized difference vegetation index) can accurately predict chlorophyll-a concentrations in the unvegetated flats (e.g. Daggers et al. 2018). Therefore, by establishing an empirical relationship between NDVI and *in situ* measured chlorophyll-a concentration from Flowers et al. (2023) and Park (2020) (Figure S1). We were able to create a spatial distribution map of chlorophyll-a concentration.

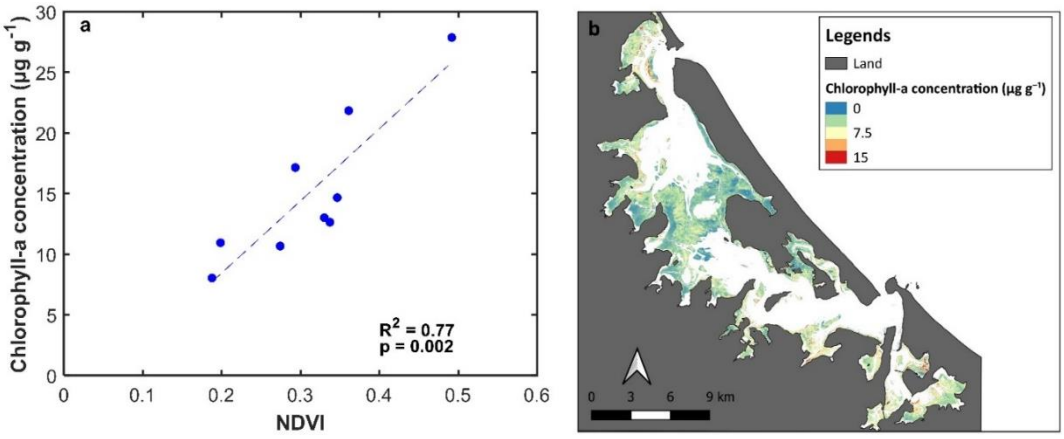

Figure S1 (a) The empirical regression between NDVI and in situ measured chlorophyll-a concentration (μg g^{-1}). (b) The spatial distribution of chlorophyll-a concentration based on the empirical regression (a), where the NDVI has been weighted by (1-seagrass % coverage) (2022 summer image).

S2 Estimating seagrass P_{max} and MPB P_{max}

In order to obtain the spatial distribution of P_{max}, we employed quantile regressions (Figure S2) between literature-derived seagrass coverage (%) and GPP (Flower et al., 2023). It is important to note that the recorded seagrass GPP encompassed a significant proportion of MPB GPP (seagrass coverage varied within the range of 38% to 64% (Figure S3), with the remaining

fraction occupied by MPB as evidenced by the chlorophyll-a content of the sediments from these treatments). Therefore, we refined the seagrass GPP calculation by excluding the MPB contribution (as detailed in Equation S1) based on the $P - I$ curve developed for unvegetated flats, with parameters listed in Table 1.

$$GPP_{seagrass} = GPP_{in\ situ} - (1 - CSG) \times GPP_{MPB\ PI} \quad (S1)$$

where $GPP_{MPB\ PI}$ was derived from the MPB $P - I$ curve. $GPP_{in\ situ}$ and CSG are the recorded seagrass GPP and seagrass coverage, respectively.

Quantile regressions from Q50 to Q90 were then tested to establish the best relationship between true seagrass GPP and coverage at submergence and emergence. Both Q90 regressions were found significant (0.011 when submerged and 0.000 when emerged, Figure S2).

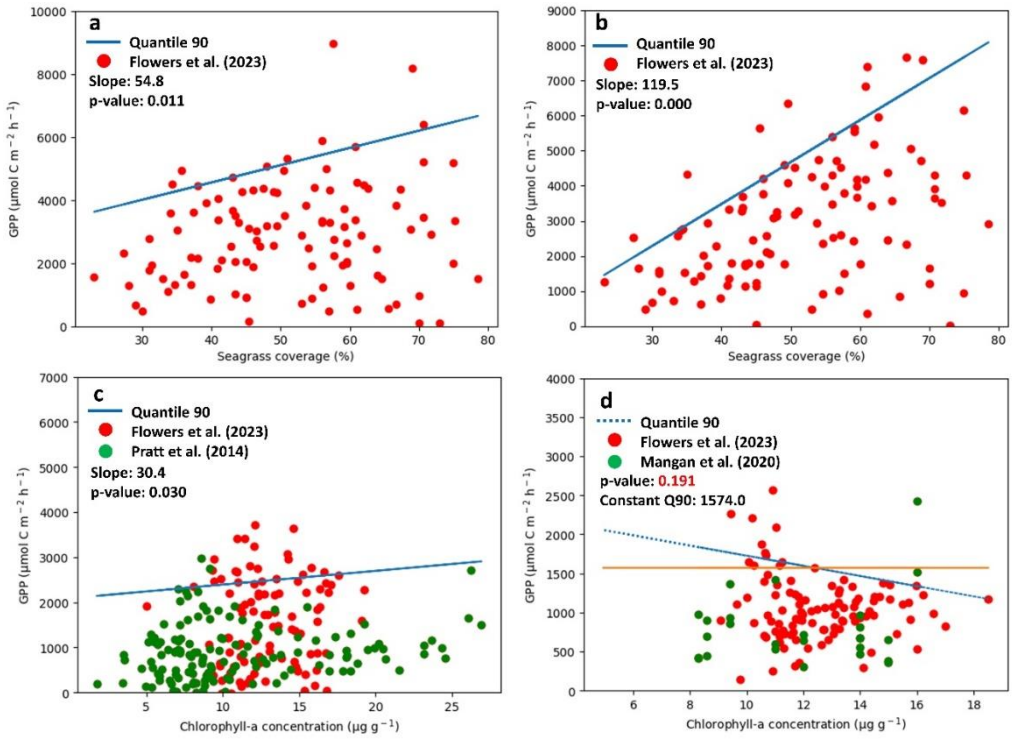

Figure S2: Q90 regressions between literature derived seagrass coverage (%) and GPP when submerged (a) and emerged (b) (from Flowers et al., 2023). Q90 regressions between literature derived MPB Chlorophyll-a and GPP when submerged (a) and emerged (b) (from Flowers et al., 2023, Mangan et al., 2020, Pratt et al., 2014).

By combining the Q90 regressions and machine learning derived seagrass coverage maps, we upscaled the literature-derived point measurements to the entire Harbour. We also investigated the cumulative probability distribution of the seagrass % coverage mapped over the whole Harbour (using summer 2019), to examine whether these data had the same range as those used in the Q90 regression. The results revealed that only 5% of seagrass coverage surpassed 80%, indicating minimal impact on seagrass GPP estimates if P_{max} remains constant beyond this threshold (Figure S3).

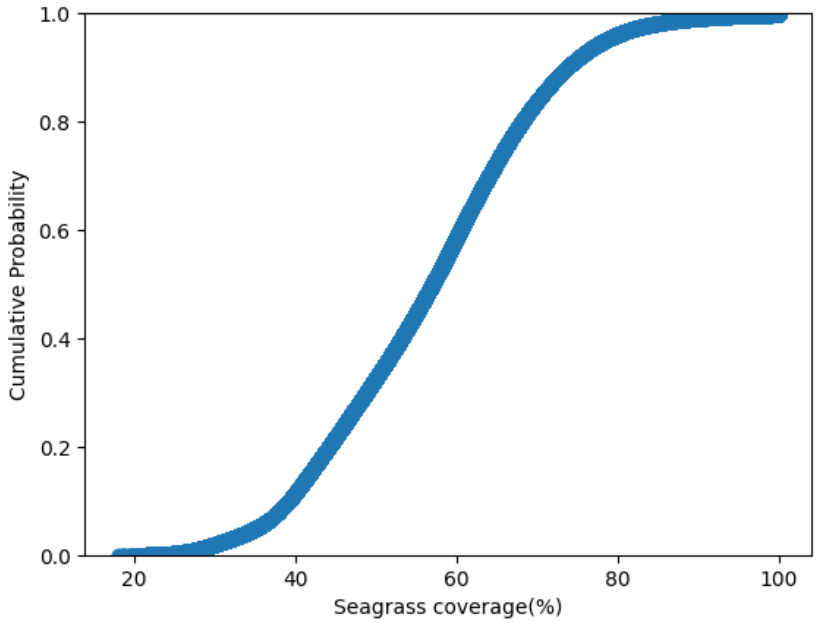

Figure S3: The cumulative probability function of the machine learning derived seagrass coverage (%) in 2019 summer.

Similarly, to the seagrass method, quantile regressions from Q50 to Q90 were tested to establish the best relationship between chlorophyll-a concentration and MPB GPP (Figure S2).

More literature derived data were included in the analysis (Flower et al., 2023; Mangan et al., 2020; Pratt et al., 2014) to improve the degrees of freedom.

S3 Estimate of migration

Although the expansion of seagrass habitats as sea level rises is unknown, to provide insight into how this might change future predictions, we assume that seabed light intensity is the primary control on the distribution of seagrass habitat (coverage) and MPB chlorophyll-a. Therefore, we used the current seasonally averaged seagrass % coverage and chlorophyll-a concentration to establish the relationships with current seabed light intensity (Figure S5). Future seabed light intensity was then used to determine future seagrass distribution (with the remaining area occupied by MPB). MPB productivity was scaled with estimated future chlorophyll-a. Additionally, we assumed that seagrass could only expand from the existing meadows to surrounding areas (pixels) at ~20 m^2 per year (averaged value derived from *in situ* measurement, Matheson et al., 2022).

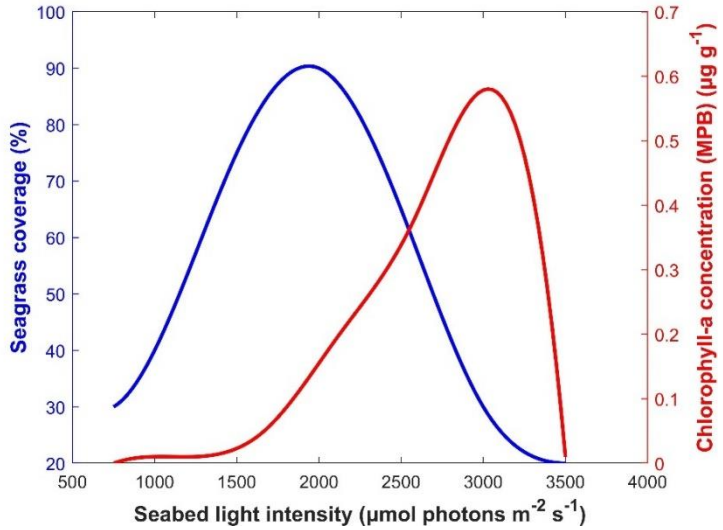

Figure S4 The observed relationship between seasonally averaged seabed light intensity and seagrass coverage and MPB Chlorophyll-a concentration, fitted to observations on Feb 24th, 2022.

S4 Comparison between the detected seagrass coverage maps

In order to validate the accuracy of the predicted seagrass coverage, we compared intertidal seagrass detected at mid-tide and low tide using images from adjacent dates.

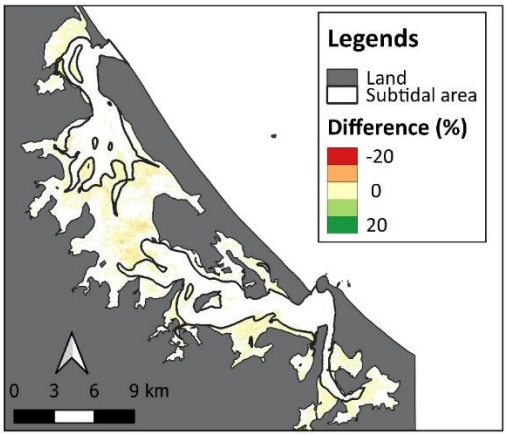

Figure S5 The difference between the detected seagrass coverage at a low tide and middle tide on the adjacent days (September 7 and 19, 2021).

S5 The spatial distribution of percentage changes of seagrass and MPB

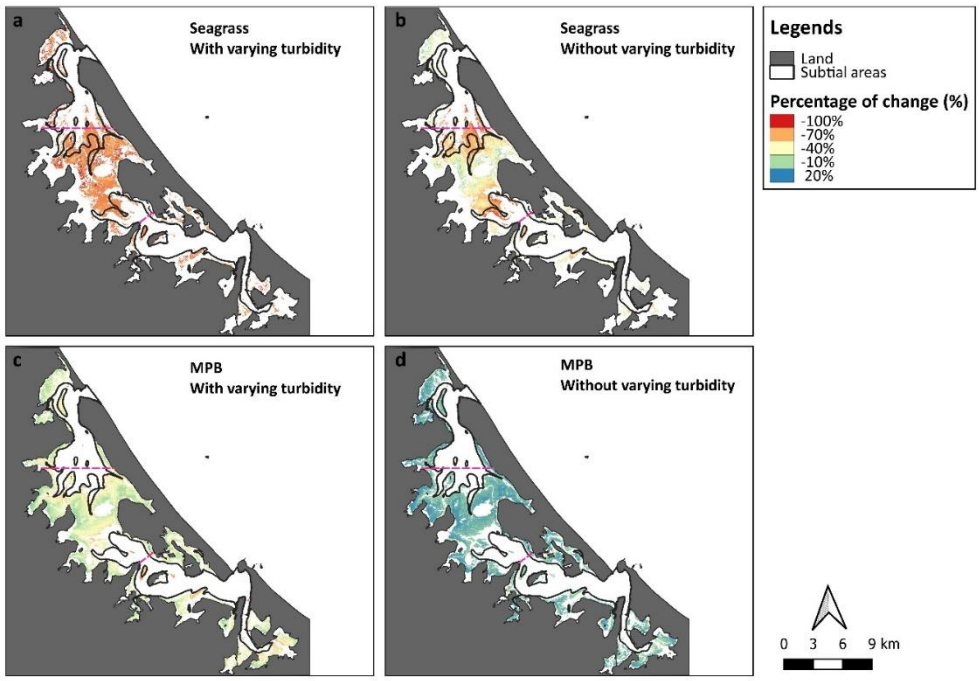

Figure S6 The comparisons at each pixel in the intertidal between the GPP of seagrass and MPB at the present and when a 1 m increase in sea level occurs with/without varying turbidity due to sea level rise and climate change, respectively.

Chapter 4

Toward Improved Estimates of Suspended Sediment Delivery to Fringing Estuarine Wetlands

Shao, Z., Bryan, K. R., Vetrova, V. Toward Improved Estimates of Suspended Sediment Delivery to Fringing Estuarine Wetlands. In preparation to submit to *Ocean Modelling.*

Ōhiwa Harbour

(Source: New Zealand Geographic)

Contribution of authors

Chapter 4 presents the paper entitled “Toward Improved Estimates of Suspended Sediment Delivery to Fringing Estuarine Wetlands”, which is in preparation to submit to *Ocean Modelling*.

Both Zhanchao Shao and Professor Karin Bryan were instrumental in the development of the model and the manuscript revision. In addition to this, Zhanchao Shao took charge of setting up the machine learning model in Python 3, as well as handling data processing and analysis. Professor Karin Bryan, along with Dr Varvara Vetrova, offered valuable feedback and assisted in refining the manuscript,

Abstract

As a dynamic component of the coastal ecosystem, suspended cohesive sediment in fringing regions influences geomorphological features, controls light availability, and serves as a transport medium for pollutants. Therefore, monitoring suspended sediment concentration (SSC) at scale is essential for understanding the resilience of wetlands and thus safeguarding the surrounding coastal ecosystem. In this study, a novel model was developed to enable continuous estimation of SSC in present and future estuarine environments, by combining intermittent satellite observations with numerical process-based modelling (Delft3D-Flow). Specifically, the prediction model consisted of two steps: (1) comparing the Delft3D-derived SSC with corrected satellite data and using K-means classification to categorise the differences into classes; (2) developing a random forest regression model for each class to predict the satellite-derived SSC using Delft3D-derived SSC and other physical parameters. The prediction model demonstrated impressive accuracy in predicting SSC testing data ($R^2 = 0.80$, MAE = 10.10), and was a substantial improvement on the SSC predictions derived solely from Delft3D simulations, assessed by comparing to a short-term deployment of *in situ* sensors (49% improvement). Different ways of accounting for incoming SSC supply to fringing wetlands (C_0) in elevation models show strong sensitivity to method. Therefore, using a real-time observation-based model such as our prediction model may result in a step change in accuracy in estimates of sediment budgets for coastal wetlands.

4.1 Introduction

In estuaries and coastal lagoons, suspended sediment concentration (SSC) plays a critical role in controlling light attenuation and dynamics of net erosion-accretion, impacting benthic primary productivity and contributing to shaping seafloor geomorphology (Elias et al., 2012; Miller & Zepp, 1979). Variations in SSC in the water column depend on both natural factors (e.g., river discharges, rainfall, tidal and wave action) (Wang et al., 2018) and anthropogenic parameters (e.g. land use, dredging and navigation) (Shin et al., 2013). By enhancing the accretion of mud flats, coastal vegetation helps maintain coastal resilience by controlling the balance between the supply of SSC to the coast and sedimentation (D'Alpaos et al., 2007). Moreover, in recent years, the escalating challenges of sea level rise and climate change have contributed to land degradation through the increased intensity of coastal flooding and erosion (Borrelli et al., 2020), ultimately associated with an upward trend of SSC in coastal waters (e.g. Asia and New Zealand, Neverman et al., 2023; Yunus et al., 2022). Therefore, there is increasing pressure to establish methods to provide continuous and accurate SSC predictive models for coastal regions on which to base effective mitigation and adaptation methodologies.

As a significant constituent of suspended sediment, the bio-physical interactions between fine-scale cohesive sediment and fringing areas during accumulation can ultimately determine the fate of the low-lying wetlands. The accumulation process begins with the transport of fine particles such as clay and silt (with particle diameter < 63μm) (Bordovskiy, 1965). The suspended cohesive sediment in the water column tends to flocculate and form larger aggregates, known as flocs, due to the inter-particle and physical-chemical forces of attraction and repulsion (Partheniades, 1962; Stone et al., 2021). The increased size of these flocs allows for faster settling and deposition in fringing environments such as mangrove and salt marsh

wetlands (Manning & Dyer, 2007) because the presence of their intricate root systems can cause frictional reductions, attenuating the incoming water velocities and trapping suspended flocs (Krauss et al., 2003; Lee et al., 2014). Over time, these deposited sediments consolidate, reducing in volume and increasing in density. This process is further influenced by microorganisms and plant roots, which stabilize the sediment and restrict seabed erosion (Lee et al., 2014; Roskoden et al., 2020) with higher exposure temperatures and durations increasing erosion thresholds (Nguyen et al., 2019). Therefore, for vulnerable low-lying coastal wetlands, the rate of sediment deposition is a major control on surface elevation and thus on resilience to the effect of sea level rise (Krauss et al., 2014).

In order to quantify the importance of SSC and sediment accumulation on wetland resilience, a combination of local measurements and model simulation is the most common approach. Surface elevation tables (SET) and sediment core analysis are widely used *in situ* methods for smaller-scale assessments (Thomas & Ridd, 2004). These local results provide accurate cohesive fraction accumulation rates and function as validation for large-scale modelling of the coastal environments (Thomas & Ridd, 2004). Popular spatially and temporally-resolved models include Regional Ocean Modelling System (ROMS) and Delft3D, which were developed for hydrodynamic simulations over deep bathymetry (Shchepetkin & McWilliams, 2005) and shallow flows in coastal areas (Roelvink & Van Banning, 1995), respectively. ROMS emphasizes the interaction of cohesive sediments with broader oceanographic processes, such as currents, eddies, and thermohaline structures (Sherwood et al., 2018). Conversely, Delft3D was more developed around the detailed behaviour of SSC occurring under various estuarine and nearshore hydrodynamic conditions (in the flow Flow or Wave modules) and incorporating a range of relevant sediment characteristics (Lesser et al., 2004). Delft3D has a strong focus on the interactions between physical processes directly affecting

sediment transport, such as turbulence, wave-current interactions, and bed shear stress (Lesser et al., 2004). A significant impediment to these highly-resolved models is the availability of calibration and verification data needed to ensure accuracy, particularly of the suspended sediment modelling components. Other more simple modelling approaches have been used to quantify the accumulated sediments in the coastal wetlands over large scales based on the zero-dimensional mass balance equation during each tidal cycle (French, 1993; Krone, 1987). These models are aimed at understanding long-term sediment accumulation at a specific point, which is presumed to represent the sediment dynamics of the entire marsh platform (Kirwan & Temmerman, 2009; Morris et al., 2002; Temmerman et al., 2003; Temmerman et al., 2004). Although the computation efficiency of these models is attractive, the assumptions needed to simplify their structures are not well tested.

Spaceborne remote sensing equipped with high-resolution sensors is one of the efficient tools for monitoring SSC at a large scale. With appropriate correction on the reflectance of optically shallow water, spaceborne remote sensing equipped with high-resolution sensors is one of the efficient tools for monitoring coastal SSC at a large scale with appropriate correction on water reflectance. As a consequence, remote sensing is increasingly used to monitor the overall water health including sediment conditions, particularly after the launch of large-swath ocean colour satellites (i.e., Landsat, Sentinel-2, Terra and Aqua) (Groom et al., 2019). Although the incoming/outgoing tides and seafloor returns can significantly bias the signals in the coastal fringing regions, several correction techniques (such as using Hydrolight and Lyzenga's model) are available to obtain true water reflectance in visible bands and thus allow observations of light attenuation (Lyzenga, 1981; Mobley & Sundman, 2008; Shao et al., 2022). By building empirical relationships with *in situ* measurements, the corrected visible bands and near-infrared band (NIR) can be used to quantify and analyse the spatial and temporal variations of surface

SSC in turbid coastal environments (Doxaran et al., 2009; P. Li et al., 2019; Zhang et al., 2014). With the implementation of machine learning (e.g. convolutional neural network) on retrieval algorithms, the accuracy of estimating SSC based on reflectance has significantly improved (Han et al., 2018). The relatively straight forward detection of shorelines using remote sensing makes it possible to record substantial and obvious changes in coastlines due to sediment accretion and erosion (Fan et al., 2018). However, due to the limited hydrodynamic and geomorphic information conveyed by remote sensing, there are very few models using satellite imagery to provide instant accurate temporal and spatial predictions of SSC, which can be used to model sediment accumulation.

In this study, we address an important technical gap in how to evaluate the control of suspended sediment supply on estuarine wetland resilience. To achieve this, we developed a machine learning model that was trained on remote sensing imagery and also enhanced with process-based information for improved predictive accuracy. Specifically, we integrated basic spatially-resolved hydrodynamic and geomorphic data from numerical modelling (Delft3D), and bathymetric/topographic surveys to optimize the predictive model. The improvements provided by the machine learning model were then assessed in an application of simple models (0-point models)for settled/deposited sediments in a fringing mangrove wetland.

4.2 Methods and materials

4.2.1 Study area and required data

This study was conducted in Ōhiwa Harbour (-37.99°, 177.09°), which is a large intertidal estuary (approximately 26.4 km^2) enclosed by two barrier sand spits (Figure 4.1) in New Zealand. The Harbour is predominantly shallow with approximately 83% of its area composed

of emerged sand and mudflats during low tide (Park, 2005). Infilling and rapid changes in the Harbour are primarily driven by the introduction of sediments from the open coast, particularly through the harbour entrance where channelization occurs (Park, 1991). Close to the southern extent of their range, the dominant vegetation in the fringing wetland areas are mangroves (*Avicennia marina subsp. australasica*). Such mangrove environments have been shown to buffer the effects of storms by reducing erosion from wave action, slowing peak flows during flooding and enabling the additional deposition of sediment/nutrients in the intertidal regions (Mazda et al., 2002).

Figure 4. 1 Map of long-term in situ SSC sampling using Aquadopp and OBS3+ deployed by Bryan et al. 2023(Site 1 – 5) and short-term in situ SSC measurements (ML081799 & ML335393) collected by the Bay of Plenty Council as well as the locations of river discharges and sediment release points. The water depth of deep channels was retrieved at 11:16 AM, January 20th 2023 based on the Delft3D hydrodynamic model mentioned in Section 4.2.2.

This study used a combination of the Sentinel-2 Level-2A atmospheric corrected data products (downloaded from the European Space Agency) and the hydrodynamic and geomorphic results derived from a Delft3D-Flow model. A total of 47 Sentinel-2 images ranging from 2019 to 2022 at 10 m resolution with cloud coverage less than 5% were selected for the study. In order to calibrate parameters used in the Delft3D model, a field survey was carried out to collect *in situ* measured hydrodynamic and suspended sediment observations at Site 1 – 5 using Nortek Aquadopps equipped with optical backscatter sensors (OBS3+) from 19th April to 17th May 2021 (summarised here, with further detail provided in Bryan et al., 2023). The suspended sediment concentration in the water column derived from the sensors was calibrated in the laboratory with a mixture of native sediments collected through extensive grab sampling across the Harbour, which were also used to inform the numerical modelling configuration (Bryan et al., 2023 & La Croix, 2022). These *in situ* SSC measurements were used to tune the Delft3D model and to develop a relationship to convert satellite reflectance to SSC.

4.2.2 Methods

Figure 2 shows a flow chart of the approach used to develop a new predictive model for SSC. In Bryan et al. (2023), the Delft3D-Flow model was tuned using the *in situ* SCC measurements in the water column (locations shown in Figure 4.1), forming the basis of the new prediction model. Nine data points collected at Site 1 – 5 from the *in situ* observations, which matched up with the pixels when Sentinel-2 revisited, were used to develop a conversion between reflectance and SSC. Two machine learning techniques were involved in developing the prediction model: K-Means classification and random forest regression. The techniques were utilized for two purposes respectively: (1) to group pixels into clusters based on discrepancies between satellite and Deflt3D-Flow derived SSC data and (2) to develop prediction models trained on satellite imagery for each cluster with Deflt3D-derived SSC and other

geomorphic/hydrodynamic parameters using random forest regression (Figure 4.2). The discrepancies in step 1 were quantified by root mean square error (RMSE), as a measure of the difference between observed (satellite-derived SSC) and numerical modelling derived results. The predictive SSC model was then compared with other common ways of representing SSC in simple (e.g. 0-point) models to estimate sediment deposition in a fringing wetland region in Ōhiwa Harbour.

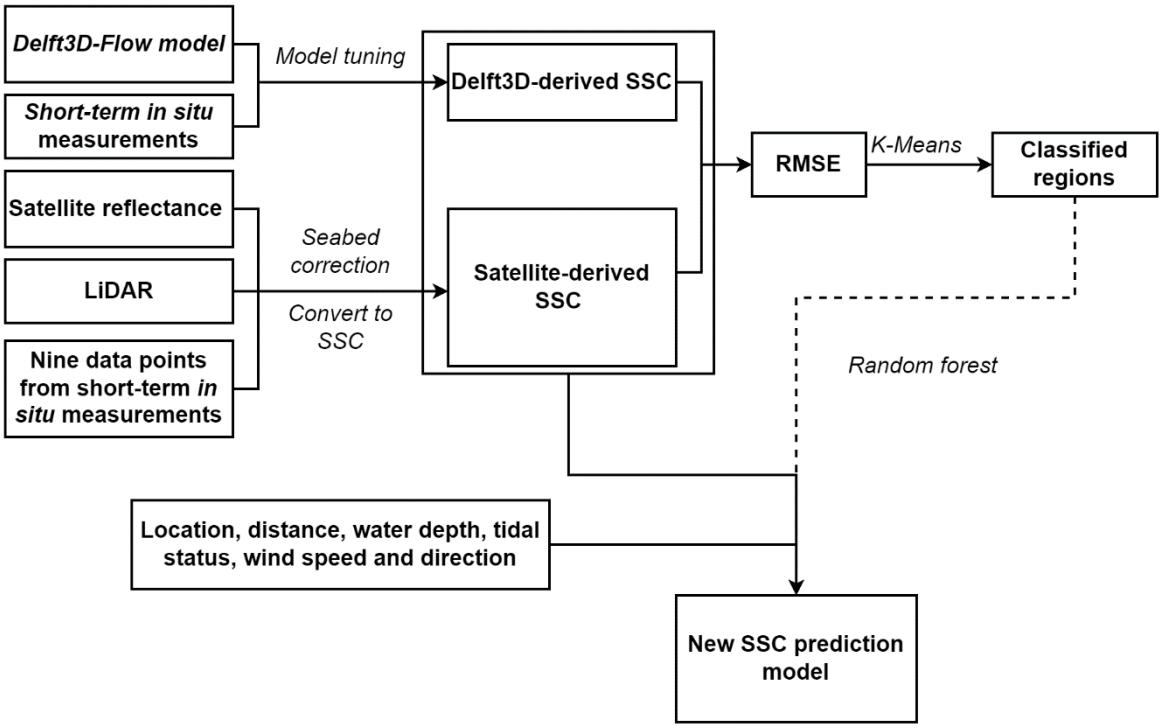

Figure 4. 2 The flow chart showing how the prediction model was developed based on numerical models and in situ measurements using machine learning.

4.2.2.1 Delft3D-Flow model setup and satellite data processing

In this study, we used a 2D depth-averaged approach — Delft3D-Flow model, which solves unsteady shallow water equations. The model was developed for a study on the sediment dynamics of Ōhiwa Harbour (Bryan et al., 2023), and consisted of two non-cohesive fractions

(sand) and two cohesive fractions (silt/mud), with spatially varying bed composition. The modelling of non-cohesive sediment involved specifying the median sediment diameter (D50) and bed density (Table 4.1). For the cohesive fraction, the parameter set included reference density for hindered settling, specific and dry bed density, fresh and saline settling velocity, and critical bed shear stress for both erosion and deposition (Table 4.1). The Engelund-Hansen sediment transport formulation was used (Engelund & Hansen, 1967), and parameters were confirmed using *in situ* observations of water level, current and SSC collected by Nortek Aqudopps and OBS3+ (location in Figure 4.1). Although hydrodynamic calibration yielded Brier Skill Scores of 0.59 – 0.92 (Bryan et al., 2023), spatial sediment calibration was more challenging. The difficulty arose from inadequate knowledge of the parameters required for configuring the sediment model, coupled with a lack of spatially-resolved calibration data (Bryan et al., 2023). Addressing this difficulty was the motivation for the new methodology presented here. Here we focused on the modelled cohesive sediment fractions (the two mud fractions) as a basis for an improved method to model SSC because these are key drivers of fringing wetland resilience and are more likely to be well detected by satellite reflectance.

Table 4. 1 Parameters set for the Deflt3D-Flow model to derive SSC.

Sediment types	Cohesive fractions		Non-cohesive fractions	
	Mud-1	Mud-2	Coarse sand	Fine sand
Reference density for Hindered settling (kg m^{-3})	1600	1600	1600	1600
Specific density (kg m^{-3})	2650	2650	2650	2650
Dry bed density (kg m^{-3})	500	500	1600	1600
Fresh settling velocity (mm s^{-1})	0.1	0.1	—	—
Saline settling velocity (mm s^{-1})	0.15	0.1	—	—
Critical bed shear stress for sedimentation (N m^{-2})	1000	1000	—	—
Critical bed shear stress for erosion (N m^{-2})	0.1	0.05	—	—

D50 (μm)	—	—	350	64

Band Red (665 nm) and Band Near Infrared (NIR, 833 nm) from Sentinel-2 were selected as a basis for spatially-resolved observations of SSC because of their strong correlation with sediment concentration in shallow (Caballero et al., 2018) and deep channels (Caballero et al., 2018; Isidro et al., 2018), respectively. Therefore, we established empirical relationships between reflectance in Band Red and SSC in the shallow water and between reflectance in Band NIR and SSC in the deep channels using the nine *in situ* data points from the short-term measurements. Due to the significant contribution from the seabed to the water reflectance (especially visible bands) in the shallow regions (water depth < 2m), we applied seabed correction on Band Red using modified Lyzenga's algorithms (Lyzenga, 1981; Shao et al., 2022). This seabed correction reduced the spatial resolution of the original data from 10m to 20m, which aligned with the Delft3D flow model grid size (20m). Band NIR was directly used to estimate SSC in the deep channels (without seabed correction) as the NIR reflectance remains constant in shallow water and decreases significantly afterwards due to the high frequency of the NIR electromagnetic waves and water absorption properties in this band (Filippucci et al., 2022; Gilvear et al., 2007). The satellite-derived SSC was then used as observed data for comparison with Delft3D-derived SSC, facilitating the development of the SSC prediction model.

4.2.2.2 Using machine learning to develop the prediction model

4.2.2.2.1 K-means clustering classification

In order to evaluate the spatial distribution of the difference between satellite and Delft3D-derived SSC, we calculated the root mean square error (RMSE) (Equation 1). Through the

process of classification, the areas requiring the same correction could be effectively grouped based on their RMSE values.

$$\mathrm{RMSE} = \sqrt{\frac{1}{n}\sum_{i=1}^{n}\left(SSC_{sat} - SSC_{Delft}\right)} \quad (1)$$

where SSC_{sat} is the satellite-derived SSC and SSC_{Delft} is the Delft3D-derived SSC.

In this study, we used K-means clustering to process classification on the RMSE map. K-means clustering is an unsupervised machine learning algorithm based on Euclidean distance, which aims to partition the data into optimal numbers of groups without prior assumptions about the error types (Sinaga & Yang, 2020). The selected method for determining the optimal number of clusters is the elbow method in which the within-cluster-sum of squared errors (WSS) are calculated (Sinaga & Yang, 2020). This method can identify the spatial patterns of RMSE derived from satellite and Delft3D SSC, which enables the characterization and categorization of different types of errors presented in the SSC maps (Sinaga & Yang, 2020). The selected 47 images ranging from 2019 to 2022 were used to calculate the RMSE to obtain the classifications.

4.2.2.2.2 Random forest

In order to predict SSC based on the Delft3D-derived results within each class defined by the K-means clustering, we used random forest regression. As a supervised learning algorithm, random forest combines the principles of decision trees and ensemble learning, which makes it particularly effective for both classification and regression (Breiman, 2001). Considering

both Delft3D and satellite-derived SSC might contain a certain number of outliers (clouds, shadows, exposed regions etc.), random forest is the optimal technique because of its low sensitivity to outliers. This is because random forest builds multiple regression trees independently by using different bootstrapped sample subsets and thus each tree relies on its subset (Steinberg & Colla, 2009). In this process, the robustness against anomalies or exposed regions is enhanced, as each tree is based on a unique subset of data, reducing the impact of outliers that may be present in one subset but not in others. In addition, random forest demonstrates robustness against overfitting as each node of a tree is partitioned based on a randomly selected independent variable from the entire set of variables. (Liaw & Wiener, 2002), which can substantially reduce the biases on the predicted SSC values.

In the prediction model using random forest, the input features included the SSC extracted at each grid cell from the Delft3D cohesive sediment transport model, the location of each grid cell (X, Y), the distance from each grid cell to the entrance of the Harbour, water depth, gradients in water level (calculated as the difference between two consecutive water levels at 10 min intervals), wind speed and direction (Figure 4.2). The location of the grid cell affects how cohesive sediments are transported, influenced by river inflow and anthropogenic activities. The distance is also highly related as cohesive sediment can travel long distances during a single tide, and cohesive sediment tends to deposit the furthest from the entrance (Whiting et al., 2005). Water depth and tidal height gradients effectively indicate the hydrodynamic conditions at each grid cell, indicating whether it is exposed or inundated and whether the tide is incoming or outgoing (Allen et al., 1980; Williams, 1970). Wind speed and direction can influence the surface waves and current patterns and thus result in sediment resuspension (Chao et al., 2008). Wind waves were not included in the Delft3D modelling, and

we hypothesise that these effects can be learned from the wind conditions, location and distance from the entrance, where the latter two would determine the fetch.

Datasets were randomly split into training/validation (70%) and testing (30%). Grid search with five-fold cross-validation was introduced to obtain the optimal values for two main hyperparameters of random forest (number of estimators and maximum depth). Two variables, mean absolute error (MAE, robust to outliers) and coefficient of determination (R^2), were used to evaluate the performance of the model when different values of hyperparameters were applied (Equations 2 & 3). Apart from the testing data, we also compared the cohesive SSC values from the prediction model with long-term measurements collected by the Bay of Plenty Council at two sites shown in Figure 1 and the SSC values from the five continuous *in situ* measurements (collected by Bryan et al., 2023, Figure 4.1) to evaluate the prediction model's overall performance.

$$\mathrm{MAE} = \frac{1}{n}\sum |y - \hat{y}| \tag{2}$$

$$R^2 = 1 - \frac{\sum (y - \hat{y})^2}{\sum (y - \bar{y})^2} \tag{3}$$

Where $\bar{y}$ represents the mean value of satellite-derived SSC and $\hat{y}$ represents a value of corrected data using random forest. Note that *in situ* measurements were used to tune the numerical model and to develop a conversion between the remotely-sensed reflectance and SSC, so only the comparison with the council's long-term measurements constitutes an entirely independent test of performance. Nevertheless, the comparison to *in situ* measurements is a measure of the new model's ability to capture temporal variability not already captured by

Delft3D A despiking algorithm (moving median, window size = 50) was applied to eliminate the outliers from the predictions from the new model (Arce, 2005).

4.2.3 Calculating the incoming cohesive sediments and accumulation

In order to determine the importance of our new predictive model to estimate the sediment accumulation in fringing mangrove areas accurately and thus understand the wetland resilience, we trialled four different approaches to applying simple (0-point) models and compared their results. In these trials, we used either the *in situ* measured, the Delft3D-derived or the new prediction model derived values to inform the appropriate value to use for incoming cohesive sediments supply to the fringing wetland in the simple models (C_0) (Table 4.2). Site 5 was selected for the trial as it was located seaward of the main mangrove-dominated fringing environment in Ōhiwa Harbour. The models were run for 23 days from April to May 2021.

Table 4. 2 Three trialled models using different assumptions on the incoming cohesive sediments and ebbing sediments.

Model name	The incoming cohesive sediments (C_0)	The ebbing cohesive sediments (C_1)	Data source	Reference
Krone's model	Constant	None	Short-term *in situ* measurements	Krone, 1987
Temmerman's model	Time-varying	None	Linear model based on water level and short-	Temmerman et al. 2003 & 2004

			term *in situ* measurements
Model $C_{out=0}$	Time-varying	None	Delft3D or the new prediction model
Model $C_{out\ variable}$	Time-varying	Time-varying	Delft3D or the new prediction model

Notes: "None" indicates that there is no sediment flux during ebb tides. The in situ measurements were from Site 5 (Figure 4.1) in Bryan et al. (2023).

The four models incorporated different assumptions on how C_0 and ebbing suspended sediment concentration (C_1) were evaluated (Table 2). Krone's model assumed that C_0 was constant for all inundation cycles and that there was no sediment flux during ebbing tides. We used the temporally averaged SSC derived from the short-term *in situ* measurements collected during flood tides (Figure 4.1, Bryan et al., 2023).

Temmerman's model assumed that C_0 was linearly related to vegetation inundation height recorded at high tide while still neglecting the export of sediment during ebbing tides (Equation 4):

$$C_0 = k(h_{HWL} - z) \quad (4)$$

where h_{HWL} is the water level at high tide (m), k is an empirical parameter (kg m^{-4}), and z is the elevation of the wetland surface (m). In this study, the value of k was calculated as 0.015 kg m^{-4} which was derived from the short-term *in situ* measurements at site 5 (which consisted of 46 high tides).

In the additional two new models, "Model $C_{out=0}$" was parameterised assuming that C_0 was time-varying. In this case, C_0 could be derived either from the Delft3D model or the new prediction model. The model also assumed that there was no flux of cohesive sediments from the wetland platform during ebbing tides. In contrast, the "Model $C_{out\ variable}$" was parameterised with both C_0 and C_1 time-varying. The variations of C_0 and C_1 were obtained using either the Delft3D model or using our new prediction model.

The results derived from each model were then transformed into the mineral sediment accretion (S) to understand the impact of different parameterisation methods on the sediment accumulation in the fringing environment (Equation 6):

$$S = \int_t^{\square} \frac{\omega_s C(t)}{\rho} \tag{6}$$

where $C(t)$ is the time-dependent depth-averaged suspended sediment concentration (SSC) (kg m^{-3}), ω_s (m s^{-1}) is the settling velocity of the suspended sediment and ρ (kg m^{-3}) is the dry bulk density of the deposited sediment (Temmerman et al., 2004). We upscaled the results to annual accretion by assuming the deposited amount remained the same and neglecting seasonal variations.

4.3 Results

4.3.1 Performance of K-means clustering

In order to obtain the spatial distribution of SSC extracted from the satellite images at the same time as the cohesive SSC extracted from the Delft3D model, reflectance in Band NIR and Red was compared to the short-term *in situ* measured SSC collected by Bryan et al. (2023). The

good correlations indicated that Band NIR and Red could be used as proxies for the spatial distribution of SSC (Figure 4.3).

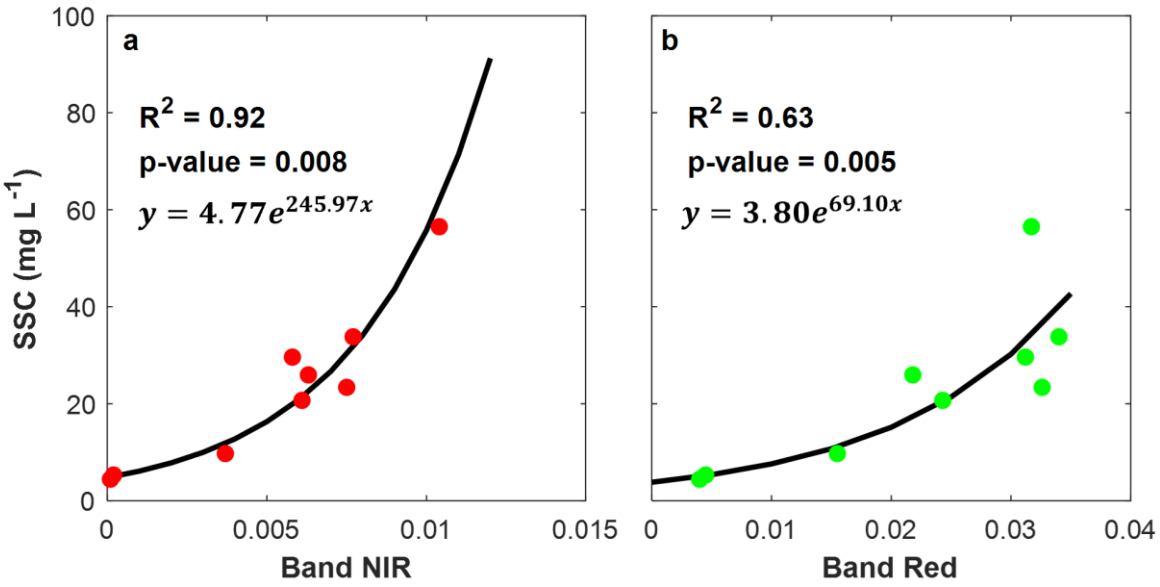

Figure 4. 3 The exponential relationships between (a) satellite-derived reflectance in Band NIR and SSC in deep channels and (b) reflectance in Band Red and SSC in shallow waters collected by Bryan et al. (2023).

The difference between satellite-derived SSC and Delft3D-derived SSC was used to determine the 4 main classes of error. Based on the RMSE of Delft3D and satellite-derived SSC, the K-means classifier identified an elbow point at K = 4, which suggested that the correction pattern in the Harbour could be categorized into four distinct classes (Figure 4.4a). The areas of shallow waters and exposed sediments were mainly classified as Class 1 & 2 as well as the shoal at the entrance of the Harbour. Class 3 contains relatively small areas at the interface of the water and land, for example in the north of the deep channel (Figure 4.4). Although encompassing a significant proportion of upper intertidal regions in the western part of the Harbour, Class 4 mainly consisted of the deep channels and their surrounding tributaries.

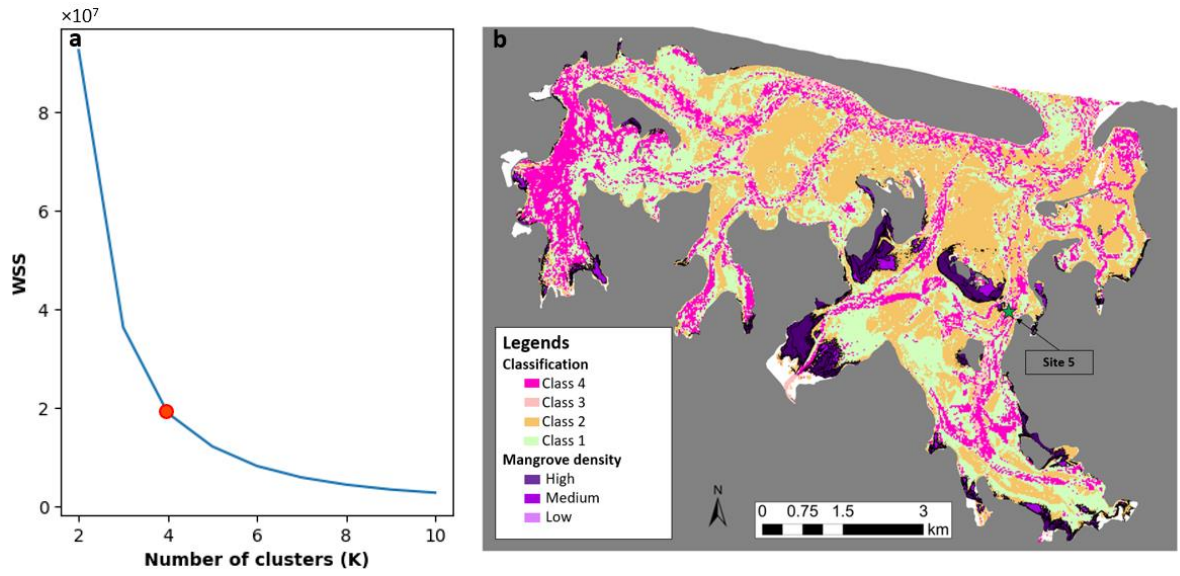

Figure 4. 4 The elbow method for optimal k-selection (a) and the map of classification based on the RMSE of Delft3D and satellite-derived SSC with mangrove distribution in the Harbour (b). In panel b, the white areas are the supratidal regions which have no significant suspended sediments. The mangrove distribution in the Harbour was mapped by training a classification based on manually labelled data (following Shao et al., 2023).

4.3.2 Performance of the random forest prediction model

After fivefold cross-validation, the optimum values of hyper-parameters for the random forest prediction model were confirmed by comparing the MAE and R^2 values of validation datasets (Figure 4.5). The optimum values for the number of estimators and maximum depth for Class 1 to Class 4 were as follows 140, 140, 160 160 and 60, 40, 60, and 50, respectively.

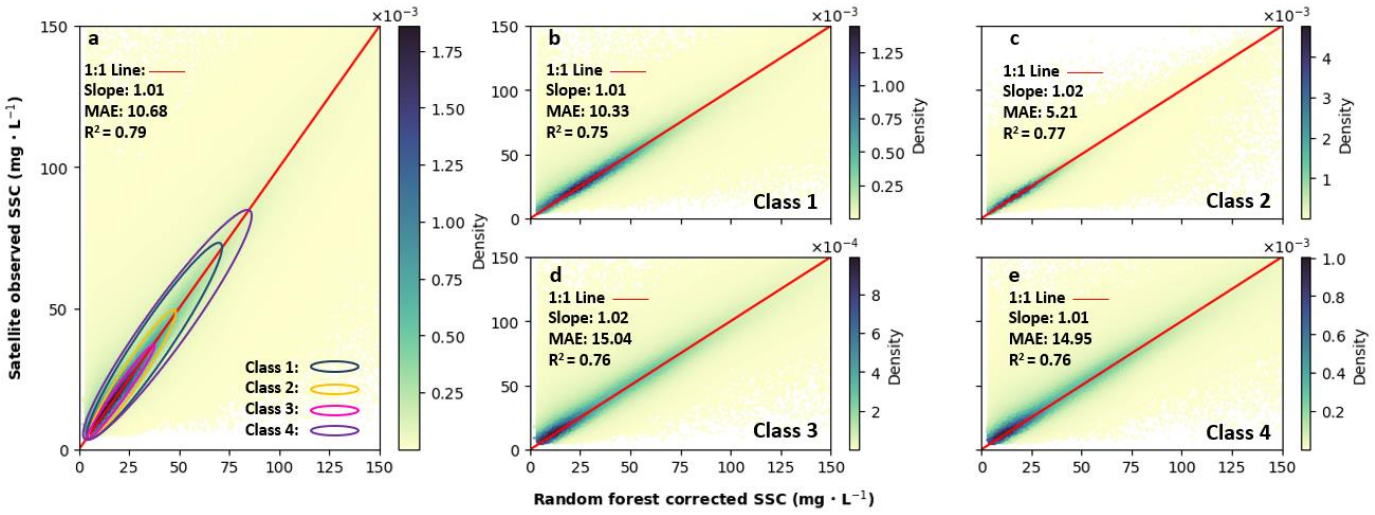

Figure 4. 5 Comparison between the satellite-observed SSC and corrected SSC, where the latter was predicted using the random forest model with all fivefold cross-validating data (a) and separate validating data in each class (b – e) categorized by K-means (Figure 4.4). The ellipses in panel a are generated based on data with 50% density in each class (b – e).

In testing, our prediction model demonstrated high accuracy in correcting the numerical model derived SSC, achieving good overall R^2 and MAE values when comparing corrected SSC with *in situ* measurements (Figure 4.6a). The best performance was observed in both Class 1 and Class 2 after removing the contribution of seabed reflectance from the water reflectance data. This process increased the homogeneity of the data, as indicated by the significantly lower MAE values (9.84 and 4.97 mg L^{-1}) than other sites. Class 3 had slightly higher errors compared to other classes, which consisted of deep channels but with some exposed area and the interfaces of sand and water at the upper intertidal regions. Those areas were barely scanned when the satellite revisited the region (Figure 4.4). Similar to Class 3, although Class 4 had a significant proportion of deep channels where uniform SSC could be observed, areas near the boundary introduced relatively high errors and reduced the general MAE of the entire region (Figure 4.4).

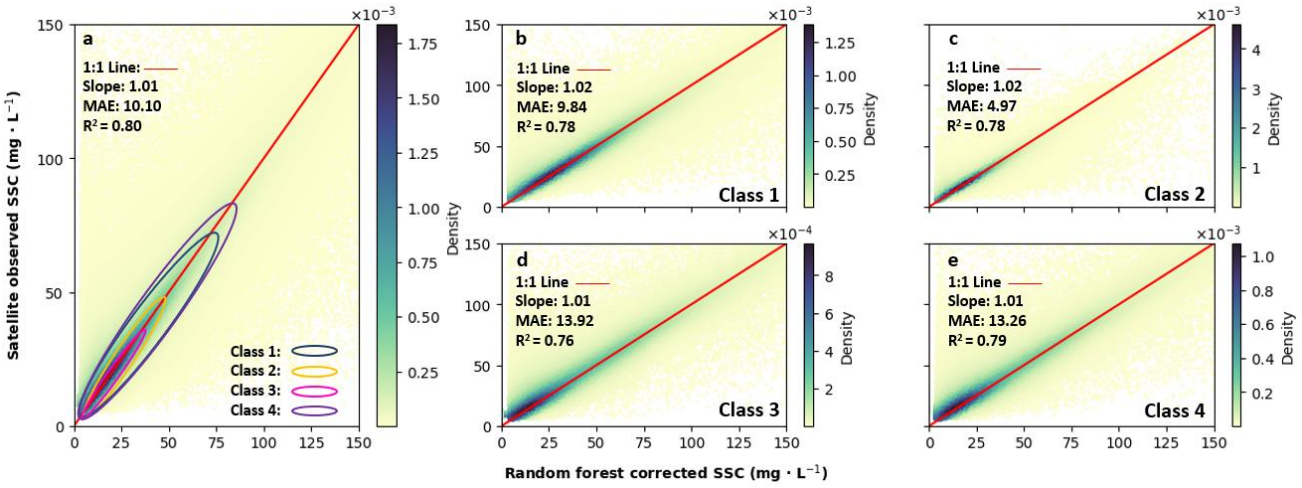

Figure 4. 6 Comparison between the satellite-observed SSC and corrected SSC using the random forest prediction model with all testing data (a) and separate testing data in each class (b – e) categorized by K-means (Figure 4.4). The ellipses in panel a were generated based on data with 50% density in each class (b – e).

The sensitivity of the prediction model was evaluated by measuring the average decrease in prediction accuracy, which reflects the model's responsiveness to specific variables (Table 4.3). The smallest contribution came from location and water depth while Delft3D-derived SSC, distance and water level gradient were found as the three main variables contributing to the prediction model. Class 3 and Class 4 shared the same importance for each variable, which was consistent with the similarity of their classification (deep channels).

Table 4. 3 The importance of selected features in the prediction model for each class.

Variables/features	Class 1	Class 2	Class 3	Class 4
Delft3D derived SSC	16%	15%	18%	18%
Location X	12%	12%	15%	15%
Location Y	6%	8%	6%	6%

Water depth	6%	8%	6%	6%
Distance	16%	17%	21%	21%
Water level gradient	18%	20%	17%	17%
Wind speed	13%	10%	7%	7%
Wind direction	13%	9%	10%	10%

By integrating Delft3D-derived SSC and other selected physical features, the prediction model provided accurate estimates of SSC over an extended period, which was essentially needed for predicting wetland resilience (Figure 4.7). While the prediction model initially struggled to provide accurate corrections at most sites on the first day (which is likely due to the Delft3D model, which forms the basis of the new predictive model still spinning up from initial conditions), it subsequently exhibited substantial improvement, as indicated by the low MAE values ranging from 5.73 to 17.31 mg L^{-1} (Figure 4.7). This performance surpassed the errors derived from the uncorrected (but calibrated) Delft3D model (9.53 to 18.98 mg L^{-1}). The MAE derived at Sites 1 and 5 were the lowest from Day 5 to Day 15 (under calm wind conditions) with slight overestimates thereafter (Figure 4.7a&e). Due to the significant overestimations in the first 3 days, Sites 3 and 4 displayed relatively weaker performance when compared to other sites (12.19 and 17.31 mg L^{-1} in MAE, respectively). However, the prediction model successfully captured the uptrend of SSC observed at Sites 2, 3 and 4. Due to the application of the despiking algorithm, the peak values were likely to be underestimated. The long-term SSC dataset collected by the council (Figure 4.1) also demonstrated the new prediction model's utility in long-term applications. According to the R^2 and MAE values (Figure 4.8), although the predicted SSC values were somewhat overestimated, the prediction model suggested a relatively high level of agreement with the long-term *in situ* measurements.

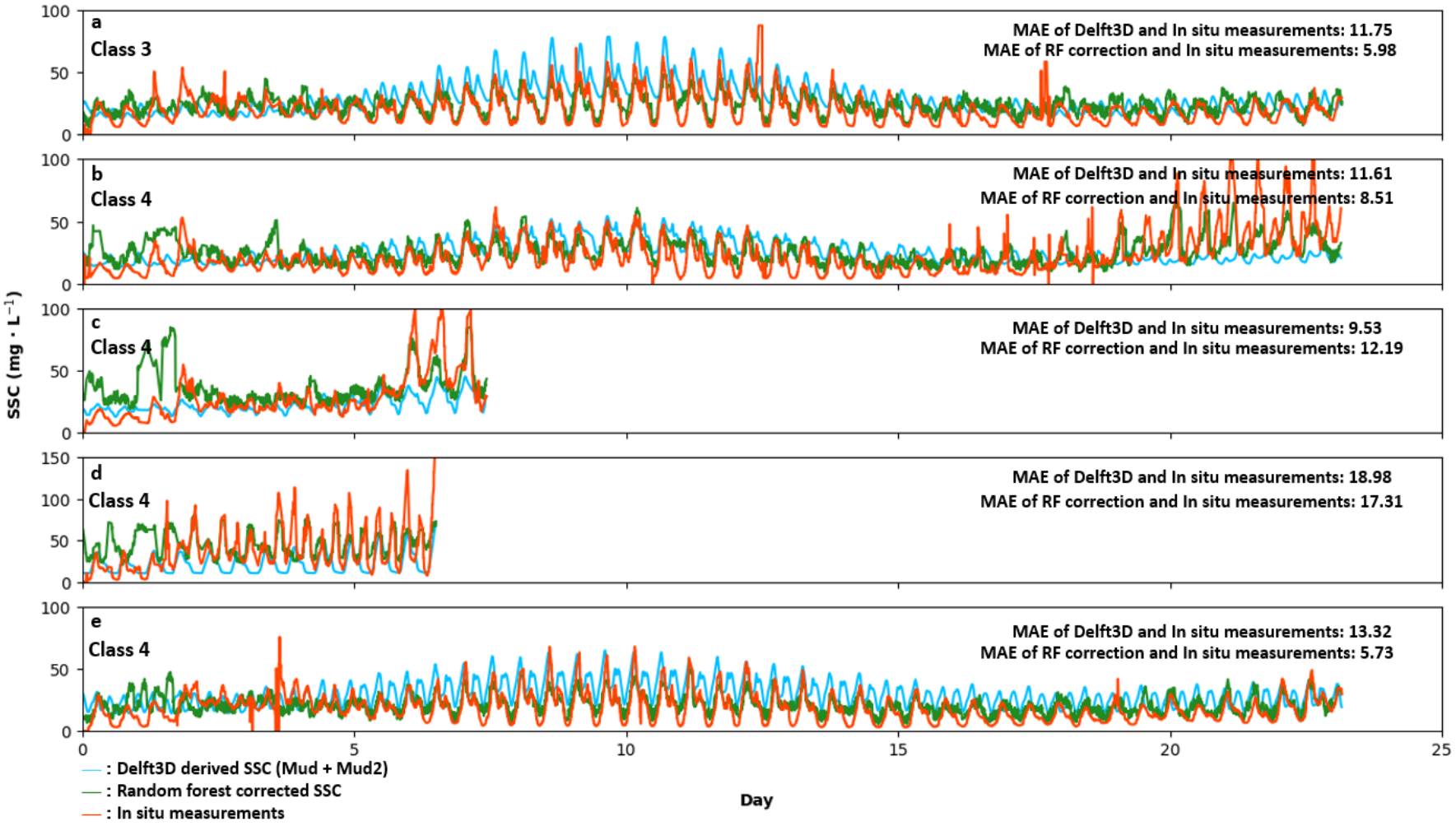

Figure 4. 7 Comparison among the Deleft3D derived SSC, corrected SSC using the prediction model and in situ measured SSC (Site 1 – 5, a – e) for the period at the beginning of the deployment.

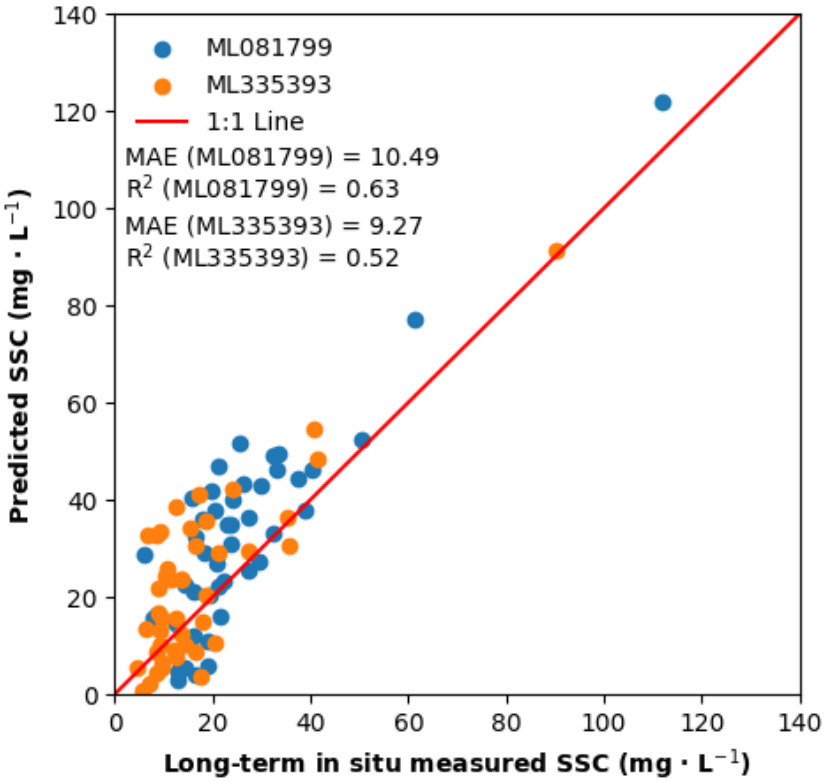

Figure 4. 8 Scatterplots of the SSC predicted using the new random forest-based predictive model and the long-term in situ measured SSC collected at the two sites in Figure 4.1 by the Bay of Plenty Council (from 2018 to 2022).

4.3.3 *Comparisons of C_0 and accumulated sediments using different methods*

After confirming the performance of the prediction model for *SSC*, the output was used to inform the way in which sediment delivery C_0 was parameterised in simple marsh elevation modelling. The results showed that the use of different models caused substantial differences in C_0 estimation, which further affected the understanding of sediment accumulation and consequently fringing wetland resilience. At this particular location in Ōhiwa Harbour, the way in which C_0 is parameterised is nearly an order of magnitude difference in sediment delivery to fringing wetlands, with the constant and the new predictive model showing lower delivery than the other two methods.

The variability in C_0 would lead to even greater differences when they were applied to different sediment accumulation models. In Krone's model, the use of a constant C_0 resulted in markedly lower sediment accumulation values (1.92 mm/yr) than in Temmerman's model and Model $C_{out=0}$ which assumed a time-varying C_0 and no exported sediments during ebbing tides. Temmerman's model, aligning with its higher C_0 in the linear model, projected the highest annual sediment accretion (3.7 mm/yr) (Figure 4.9). Conversely, the estimates from $C_{out\ variable}$ were the lowest among the four models, regardless of whether using Delft3D (1.37 mm/yr) or prediction model derived C_0 (1.13 mm/yr) (Figure 4.9b). This difference implied a significant export of sediment during ebbing tides, which was neglected in Krone's, Temmerman's and $C_{out=0}$ models.

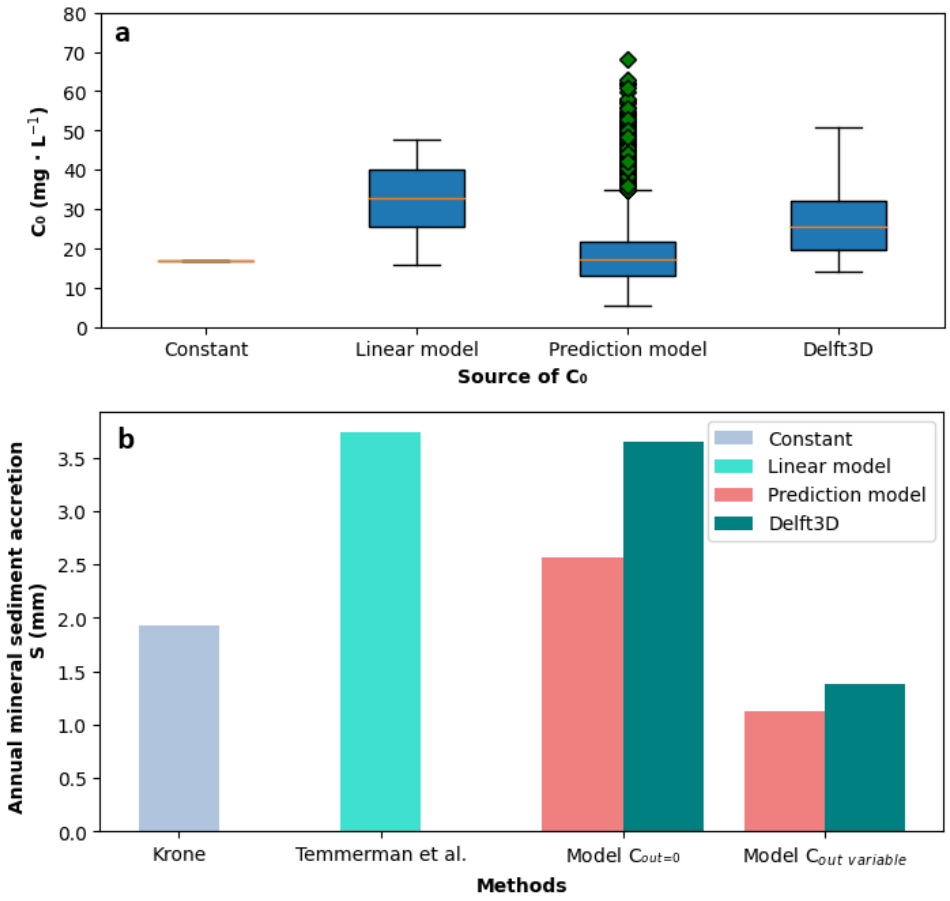

Figure 4. 9 (a) The boxplots of the estimated C_0 using different methods corresponding to Table 4.1 and (b) the estimated annual mineral accretion using C_0 from different methods.

4.4 Discussion

In this study, we demonstrate how to develop a robust machine-learning model to correct Delft3D-derived SSC data by incorporating satellite observations and environmental/physical parameters. With the use of numerical simulation, this model can provide accurate continuous spatial distribution maps of SSC at scale and thus supplement satellite observations (such as to fill gaps during cloudy conditions). In addition to filling in gaps using the prediction model in the hindcast mode, since the predictive model is driven by Delft3D model output, which in turn is forced by tides at the ocean boundary, river discharge and suspended sediment concentration, wind speed and direction, it could be nested inside catchment flooding and weather models to be run in more of a forecasting mode. Future SSC projections would inform the potential combined impact of sea level rise and climate change related changes to weather conditions. Combined with sediment accumulation algorithms, this model can also be extended to predict sediment transport over a period, estimate the settling of fine particles during flood tides and thus estimate the effect of sediment deposition on the resilience of fringing wetlands. Therefore, sediment dynamics information provided by this model can help underpin coastal management actions aimed at, for example, monitoring sediment transport at a large scale or evaluating the loading limits for the coastal environments. Understanding future SSC is also an important component in determining the wider-reaching implications of climate change to estuarine ecosystems, for example as a basis for predicting seabed light conditions which fuel primary productivity in estuarine settings (Mangan et al., 2020; Shao et al., 2024).

Although the approach of combining numerical simulation, remote sensing, and machine learning to predict SSC in intertidal estuaries is in a preliminary stage, this trial has

demonstrated the capacity to produce promisingly accurate SSC predictions based on the error classification map. While increasing the K values in our K-means clustering could lead to more detailed class distinctions, we chose to fix K at 4 in consideration of the bias-variance trade-off (Agarwal & Mustafa, 2004). At K = 4, the clustering model returned a relatively low WSS value, and the classifications exhibited a high consistency with the original geomorphic features of the estuary (Figure 4.4). After classification, despite the presence of outliers, the random forest model still achieved an accurate prediction of the testing data with the R^2 and MAE values of 0.8 and 10.10, respectively (Figure 4.6). This is probably because random forest algorithms can preserve accuracy by autonomously estimating missing data and counterbalancing errors in biased SSC values (Breiman, 2001). For the short-term continuous monitoring at five sites in the deep channels, the random forest prediction model produced relatively accurate SSC results with the MAE values ranging from 5.73 mg L^{-1} to 17.31 mg L^{-1}, which yielded a substantial improvement compared to Delft3D-derived SSC (errors were reduced by up to 49%) (Figure 4.7). Additionally, the random forest prediction model still outperformed (errors were reduced by up to 42%) in comparison with the alternative methods such as applying data assimilation in a similar estuary (Chen et al., 2022). However, a significant proportion of the errors were caused by data spikes during the initial days. These errors could be attributed to the contrasting trends between Delft3D-derived SSC and *in situ* measurements (Figure 4.7b and Table 4.3), or possibly to unusual features during that period (Table 4.3). By incorporating spatial features (such as location and distance), the random forest model produced a more nuanced prediction of the SSC data, enabling relatively precise estimations over the entire Harbour including in shallow waters.

Derivation of more accurate suspended sediment concentration is essential for predicting wetland resilience since modelled accumulation rates are very sensitive to the way in which new sediment is delivered to the wetland (C_0). Indeed, there are many recent studies predicting sediment accumulation in the fringing wetlands, conducted in an attempt to determine their resilience to sea level rise in various settings. These models vary substantially in the way in which they characterise processes such as consolidation (Gallegos et al., 2023), root biomass production (Schile et al., 2014) and channelization (Grossman et al., 2020). However, these models are also dependent on the assumption relating to incoming sediment supply (C_0). For example, the wetland accretion rate model of ecosystem resilience (WARMER), which incorporates hydrodynamics and marsh topography, demonstrated sensitivity to the variations of incoming sediment inputs (Swanson et al., 2014), aligning with the *in situ* observations by Stralberg et al. (2011). Other research also indicated that an increase in the flooding sediment supply could result in a twofold rise in the estimates of accumulated accretion when using the sediment accretion and migration model based on hydro-simulation and vegetation cover (Breda et al., 2021). Rather than setting C_0 as a constant (eliminating the dependency of C_0 on time) (Krone, 1987) or modelling C_0 by relating sedimentation to platform elevation (neglecting the export of sediments during ebbing tides) (Temmerman et al., 2003), our prediction model yielded relatively accurate temporal patterns in C_0, which were close to the *in situ* measurements (Figure 4.7 & 4.8). The difference between our new model and the other models we trialled caused a range in accumulation rates between 1 and 3.5 mm/yr, which is substantial when sea level rise in this area of New Zealand is estimated at 4.2 mm/yr (https://www.searise.nz/). In reality, such zero-point models do not incorporate processes such as attenuation of flows and energy across the marsh. Although more complex models still neglect incorporating biophysical feedback (e.g. Bouma et al., 2007), the

vulnerability and resilience of fringing environments to sea level rise derived from these models tend to be less biased than the zero-dimensional (0-D) models (Kirwan et al., 2016; Raposa et al., 2016).

The six ways that were trialled to estimate sediment delivery to fringing wetlands are each associated with different approximations of processes. The constant C_0 obviously neglects the variability induced by events in the estuary which cause greater localised (in time and space) sediment resuspension and seabed erosion (Krone, 1987; Storlazzi et al., 2011). Using a representative dataset to determine an appropriate constant C_0 would allow more accurate prediction, but if such measurements were available, it would be better simply to use a time-varying C_0 directly from observations. Although Temmerman's linear model related the sediment accumulation to inundation time and the distance to the marsh edge, the two main physical parameters that controlled sediment transport in the wetland were neglected: sediment properties and hydrodynamics (Temmerman et al., 2003). Applying such 0-D models in long large channels might lead to biases in sediment accumulations because velocity, total kinetic energy and suspended sediments attenuate significantly with distance from the marsh edge (Leonard & Croft, 2006; Zhang et al., 2019). The assumptions that there is no exported sediment used in Krone's, Temmerman's model and Model $C_{out = 0}$ will likely overestimate accumulation; for example, other studies (e.g. marsh wetlands in Poplar Island) observed significant amounts of outgoing sediment during ebbing tides (Fleri et al., 2019). Using a real-time model to estimate C_0 and C_1 seems an efficient and appropriate way to ensure the contribution of ebbing tides to the budget is incorporated.

In this study, we developed a new prediction model to estimate the incoming cohesive sediment concentration, which was less labour-intensive than obtaining sufficient

calibration and validation data to inform a dynamic sediment transport model while maintaining accuracy. The prediction model could be easily scaled up to multiple estuaries without the need to collect substantial *in situ* measurements (as long as long-term monitoring data are available to provide local conversions between satellite reflectance and SSC) and therefore may be of greater utility to resilience planning than dynamic based models (Ganju & Schoellhamer, 2009) or highly simplified models (such as advection-dispersion model, Fagherazzi et al., 2012).

Limitations

Using the modified Lyzenga's seabed correction model and the empirical relationships to derive SSC may introduce unneglectable errors to the prediction model and thus impact its feasibility. For the shallow waters (water depth < 2m), we used Lyzenga's model to remove the contribution of seabed reflectance to the true water reflectance with the assumption that spatial variations in the water and seabed characteristics were small over local scales (Shao et al., 2022). This prediction model tended to result in additional errors in regions where nonuniform sediment properties exist. In addition, the R^2 value of the logarithmic regression between reflectance in Band Red and *in situ* measured SSC for shallow waters was relatively low (0.63), which likely accounts for the degree of scatter in Figure 4.5 and 4.6. Therefore, further development of our prediction model is limited by the availability of match-ups to calibrate the reflectance data. To enhance the prediction model's accuracy, future research should also focus on comparing the performances of different machine learning algorithms and expanding the range of features considered, such as incorporating anthropogenic activities (Yunus et al., 2022), and thus provide a more nuanced understanding of SSC dynamics within the estuary.

4.5 Conclusion

In this study, we demonstrated the application of random forest in predicting the incoming cohesive sediment concentration to a coastal wetland in Ōhiwa Harbour using Delft3D and geomorphic features as training and satellite images as the target. We show how this model could be used in conjunction with simple fringing wetland sediment accumulation models to understand sediment budgets and resilience of these fringing environments due to sea level rise. Our results indicated a high level of accuracy in predicting SSC when compared to testing data ($R^2 = 0.80$, MAE = 10.10). Furthermore, when compared to the *in situ* measurements from two sources, the prediction model showed a notable increase in accuracy (reducing errors by up to 49% in comparison to the direct use of the Delft3D-Flow model) (Figure 4.7) and compared to long term monitoring datasets (Figure 4.8). Testing showed that different ways of estimating C_0 in sediment accumulation models could cause significantly different accumulation rates, highlighting the importance of further research on this critical parameter. Therefore, using a real-time prediction derived from long-term and spatial observation such as our prediction model can help reduce the biases in prediction.

Chapter 5

Classifying Estuaries using New Satellite-derived Optical Indicators

Shao, Z., Bryan, K. R., Clark, D., Pilditch, C. A., In preparation to submit to *Estuaries and Coasts.*

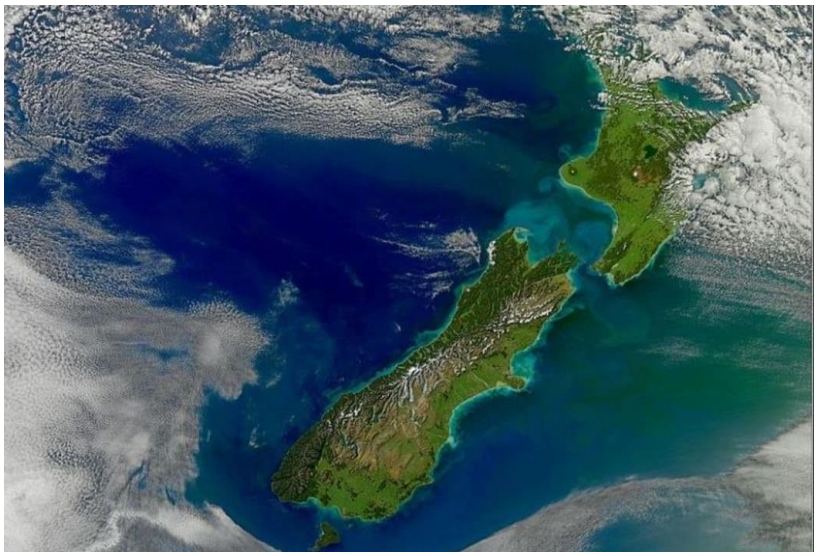

Satellite image of New Zealand

(Source: Radio New Zealand)

Contribution of authors

Chapter 5 presents the paper entitled “Classifying Estuaries using New Satellite-derived Optical Indicators”, which is in preparation to submit to *Estuaries and Coasts*.

Zhanchao Shao and Professor Karin Bryan both contributed to manuscript editing. Zhanchao Shao was also responsible for data processing and data analysis. Dr Dana Clark provided important ecological data. Professor Karin Bryan, Dr Dana Clark and Professor Conrad Pilditch provided useful comments and helped revise the draft.

Abstract

Satellite reflectance images, such as from Sentinel-2, are widely used to monitor coastal water by quantifying the concentration of optically active constituents (OAC) in the waterbody. However, these indicators are not commonly used to supplement estuarine monitoring programmes due to the complexity of application to shallow intertidal water bodies. Therefore, in this study, we use the modified Lyzenga's model to demonstrate how satellite-derived dominant wavelength and diffuse attenuation coefficient in band blue (K_d Blue) can be used as indicators to monitor estuarine water health over large scales in 12 New Zealand estuaries. These two indicators integrate several parameters including chlorophyll-a, coloured dissolved organic matters (CDOM) and suspended particular matters (SPM) due to their high correlation with OACs. Although smaller scale variability was site-specific, both indicators showed a strong seasonality in summer and winter. In addition, dominant wavelength and K_d Blue were correlated (R = 0.83) which meant that K_d Blue to be inferred in deep channels. Using K-means clustering for classification, twelve estuaries were categorised into three groups including less impacted, moderately impacted and highly impacted. Classes were well-aligned with other *in situ* monitoring methods such as light availability, benthic health model scores and eutrophication index. The study provides a foundation for future work assessing estuarine health automatically using satellites, which can provide a step change in spatial and temporal resolution, and allow improved detection of impending system state changes.

5.1 Introduction

Estuaries and shallow coastal lagoons in temperate regions are highly sensitive to anthropogenic effects such as additional suspended solids, pollution and nutrients (Ellis et al., 2015). These extra sediments can substantially alter estuarine optical properties, reduce light penetration and shorten the depth of the photic zone in the water, which flows to a decrease in light availability and benthic productivity (Gattuso et al., 2006). Without preservation and restoration, the impact on the ecological balance of these aquatic environments is likely to trigger regime shifts in estuarine health and eventually lead to eutrophication or degradation (Rodriguez & Heck, 2021), evidence of which can already be found in *in situ* observations (Clark et al., 2022). Developing a suite of remotely sensed indicators of estuarine health, applied at scale across many estuaries, which can be collected routinely, would provide a basis to classify and benchmark estuaries with similar conditions into groups to detect trends and target conservation strategies.

Remote sensing is widely used to monitor coastal inherent optical properties (IOP) at large temporal and spatial scales by quantifying absorption (a) and backscattering (b_b) of light. Therefore, absorption and backscattering are commonly used as a basis for indicators due to their strong correlation with optically active constituents (OAC) such as suspended sediment concentration (SSC), coloured dissolved organic matter (CDOM) and chlorophyll-a concentration (Boss et al., 2009; Pavlov et al., 2015). The retrieval algorithms derived from empirical or semi-analytical relationships between remote sensing reflectance and *in situ* measured OAC concentrations have allowed the precise estimation of a and b_b (Ogashawara et al., 2017). For example, a simple empirical model between chlorophyll-a concentration and reflectance in band green (O'Reilly, 2000) or the normalized difference chlorophyll index (NDCI) (Mishra & Mishra, 2012) have been

used to detect absorption by pigments in the coastal water region. Compared to simple empirical approaches, semi-analytical models are more robust (Vos et al., 2003), as these models integrate detailed spectral information from each IOP, allowing for a more precise and reliable interpretation of watercolour (Astuti et al., 2018). However, due to interference by the seabed on detection of true water reflectance, the accuracy of satellite-derived a and b_b is restricted especially in Case 2 optically shallow water regions.

New seabed reflectance correction models have allowed the recent development of satellite-derived indicators for estuaries, which can provide a direct and detailed understanding of estuarine optical properties such as dominant wavelength and diffuse attenuation coefficient (K_d) (Shao et al., 2023). Based on the radiative transfer equation and a complete spectral library of different land covers, Hydrolight and Water Colour Simulator (WASI) have become the two most frequently used models to quantify the true water reflectance (Gege, 2005; Mobley & Sundman, 2008). In addition, the reconfiguration of Lyzenga's algorithm also provides an opportunity to correct the seabed reflectance by using the exponential relationship between water depth and received signals (Lyzenga, 1981; Shao et al., 2023).

Once corrected, dominant wavelength and diffuse attenuation coefficient can be derived from the water reflectance, which we hypothesize may provide a solid basis for investigating estuarine health at scale. Woerd and Wernand (2015) proposed empirical algorithms to connect satellite-derived reflectance to tristimulus values using multilinear regressions based on blue, green and red bands, which bridges the gap between remote sensing and colour science data. This method has been expanded to a series of high- and middle-resolution satellites such as Landsat 8, Sentinel-2 and Worldview-3 (Woerd & Wernand, 2018). Converted from tristimulus values, the use of dominant wavelength is

an intuitive way to evaluate water colour since it can reflect the water colour numerically as perceived by the human eye (Lehmann et al., 2018; Post, 1997). The diffuse attenuation coefficient reflects how light at a specific wavelength dissipates with depth in water, which can be used as an alternative measure of water turbidity and clarity due to their high correlation (Mitchell & Holm-Hansen, 1991). The derivation of K_d includes building empirical relationships with remote sensing reflectance (such as blue-to-green ratio) (Mueller, 2000), applying the radiative transfer model (Lee et al., 2005; Sokoletsky et al., 2014) or using the modified Lyzenga's model (Shao et al., 2022). However, few studies explore the possibility of using dominant wavelength and K_d to evaluate the intertidal estuarine optical properties on the national scale.

The traditional satellite-based classification of estuarine health usually relies on one index or parameter, which is limited in its ability to describe the state of coastal water completely. The Trophic State Index (TSI), based on the chlorophyll-a concentration, is widely used to classify waters with similar eutrophication levels (Martins et al., 2017). Other parameters used to group waterbodies include normalized difference turbidity index (NDTI) (Garg et al., 2017), water surface temperature (Schaeffer et al., 2018) and salinity (Geiger et al., 2013). The latter can be derived from visible bands using empirical relationships based on *in situ* measurements (Ansari & Akhoondzadeh, 2020). However, the classification based on individual indexes provides relatively limited information compared to multi-indicators because one index is unlikely to capture all aspects of water quality due to the complexity of coastal water (O'Brien et al., 2009).

The objectives of this study were to (1) evaluate the feasibility of assessing intertidal estuarine health using satellite-derived dominant wavelength and K_d and (2) to use this to classify estuaries which could form the basis of a satellite-based monitoring system on a

nationwide scale. The study was carried out in 12 temperate intertidal coastal environments across New Zealand using the Sentinel-2 data collected from 2019 to 2023. We aimed to detect the seasonal and locational features for each site and connect this information to potential contributing factors, with the long-term goal of underpinning coastal management and restoration plans.

5.2 Materials and methods

5.2.1 Study area and required data

Twelve estuaries across New Zealand were involved in this study (Figure 5.1), chosen for their distinctive ecological and environmental features. These estuaries were Mahurangi, Manukau, Raglan, Tauranga, Whangārei, Whangateau, Whitianga, Akaroa, Avon, Newriver, Delaware, and Waimea. These sites provide a diverse representation of New Zealand's estuarine environments, ranging from relatively pristine ecosystems like Mahurangi (Patel, 2011) to urban-influenced estuaries such as Manukau (Davies, 2015). The contrasting sediment sources, from uniform black sands in Raglan (Phillips et al., 2001) to a mixture of rocky and sandy shores in Whangārei (Spörli & Harrison, 2004), present varied settings for water quality assessment. This variety ensures that the study's findings can inform a wide range of management and conservation strategies for estuarine environments in New Zealand and beyond.

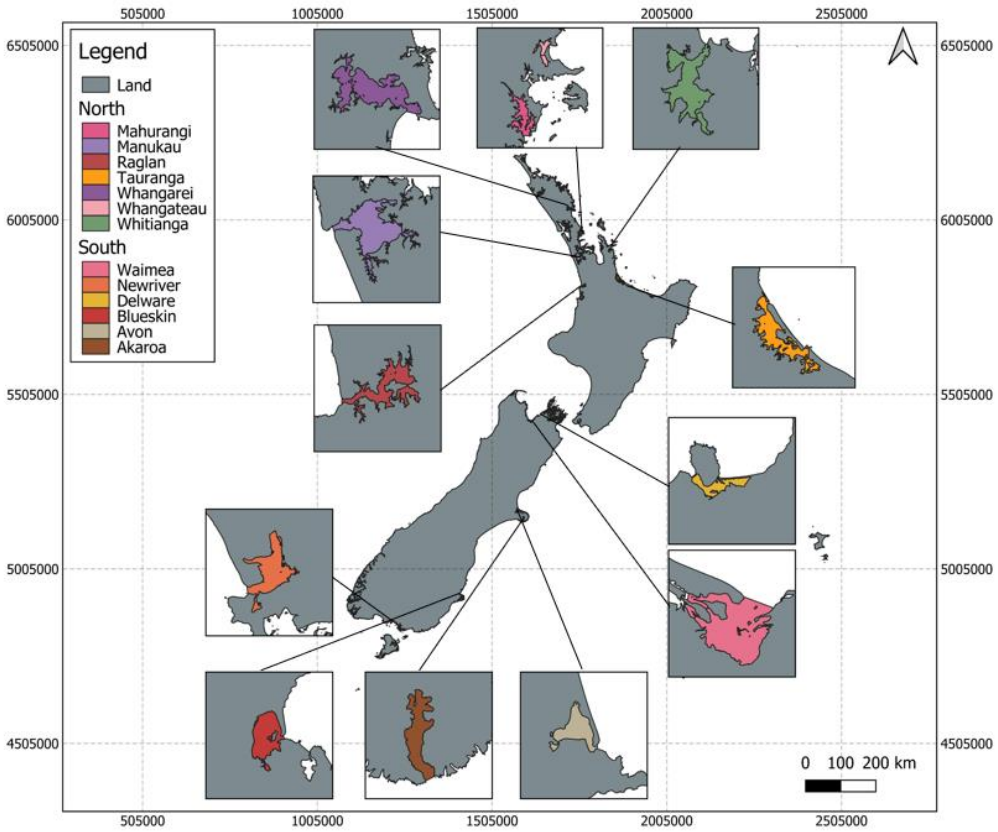

Figure 5. 1 The distribution map of selected estuaries across New Zealand.

In this study, we chose Sentinel-2 data (available on the European Space Agency) because its high spatial (10 m) and temporal resolution (revisiting New Zealand every five days) allowed for the continuous observation of selected estuaries. The Sentinel-2 images were captured between 2019 and 2023 from the Level-2A collection (after atmospheric correction). A total of 352 images with cloud coverage less than 5% were obtained for the study. Water depth at each pixel was estimated by the combination of the local elevation model (airborne light detection and ranging (LiDAR)) downloaded from Land Information New Zealand (LINZ, https://www.linz.govt.nz/) and tide levels provided by the National Institute of Water and Atmospheric Research (NIWA, https://tides.niwa.co.nz/).

5.2.2 Methods

Figure 5.2 shows a flow diagram of the approach used to classify estuaries using diffuse attenuation coefficient in band blue and dominant wavelength derived from corrected reflectance in visible bands. The approach mainly included three steps: (1) using normalized difference water index (NDWI), LiDAR and tide heights to derive the intertidal regions; (2) correcting the water reflectance for seabed effects and calculating dominant wavelength and K_d Blue; (3) classifying estuaries based on these two indicators.

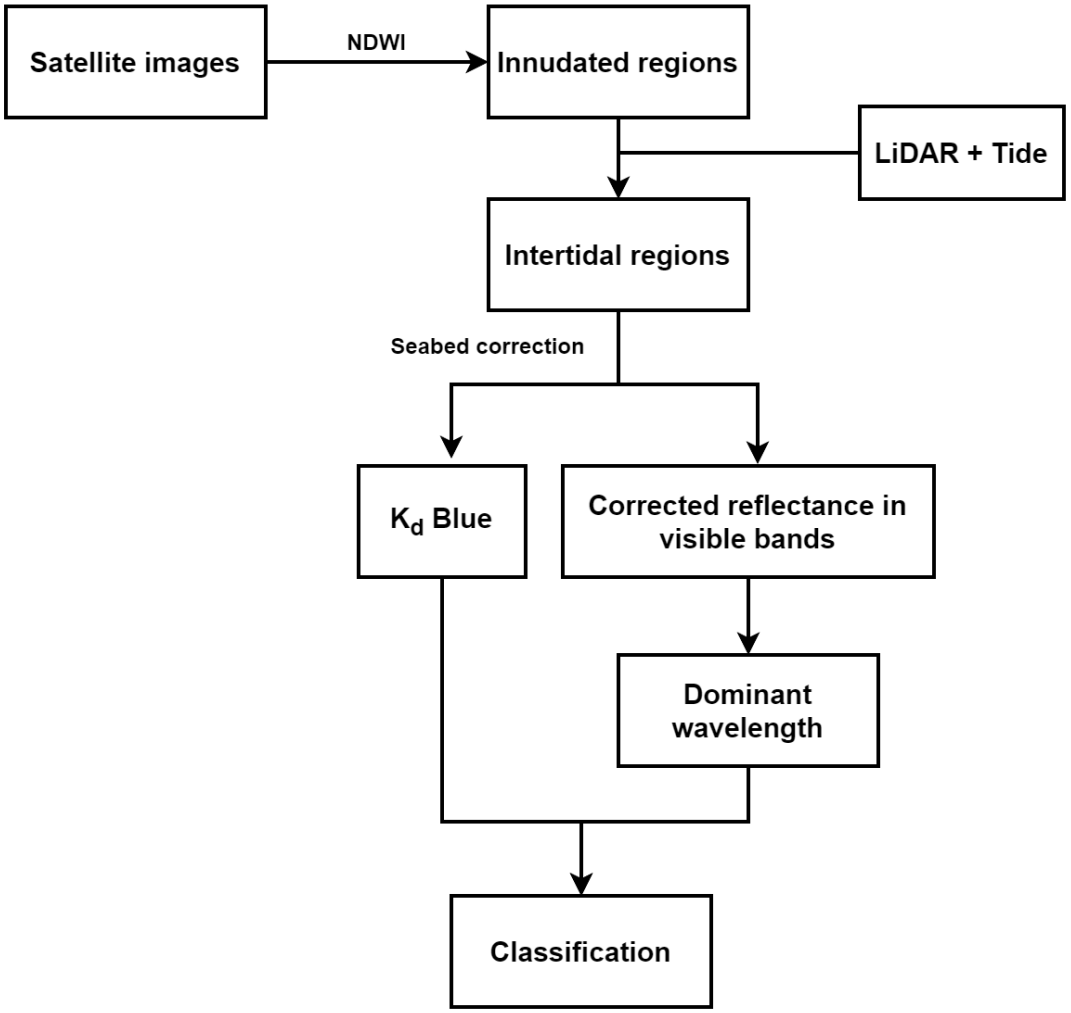

Figure 5. 2 The flow chart showing how to apply seabed correction and calculate K_d Blue and dominant wavelength.

5.2.2.1 Reflectance correction and calculation of K_d

Water depth derived from LiDAR and local tide levels and NDWI were used to confirm the inundated regions for images at each site because the variation of the NDWI can effectively detect waterbodies and or water level changes (McFeeters, 2013). The threshold we applied here was 0.3 using band Green (560 nm) and band NIR (883 nm) (Equation 1).

$$\mathrm{NDWI} = \frac{R(Green) - R(NIR)}{R(Green) + R(NIR)} \quad (1)$$

In order to correct contributions from the seabed to the water surface reflectance (R_w) and calculate the associated K_d, we applied the "spatial method" with the tile size of 60m from the modified Lyzenga's model in the intertidal regions to estimate K_d and R_w (Equation 2) (Lyzenga, 1981; Shao et al., 2022).

$$K_{d(i)} = \frac{1}{2z_i} \times \ln\left(\frac{R_b - R_{w,}}{R_i - R_w}\right) \quad (2)$$

The three variables R_i, z_i and R_b correspond to satellite-derived reflectance and water depth at pixel *i* as well as averaged seabed reflectance of the selected pixels when exposed at low tides, respectively. The model was repeatedly applied to band blue, green and red to obtain the corrected reflectance in each visible band.

The values of R_b can be derived at low tide when the intertidal regions emerge. Considering the spatial method for seabed correction assumes that water and seabed properties are homogeneous across the selected proximal pixels (the tile), excluding pixels with different seabed cover (such as seagrass) within each tile can help reduce the

errors in estimates of K_d and $R_{w.}$ Therefore, we applied a supervised classification using random forest to detect pixels with sediments, seagrass, mangroves and *Ulva* (Shao et al., 2024) using manual labelling of pixels with different covers as training data. The appropriate R_b was then derived by averaging the reflectance with all pixels remaining after the different classes were excluded. Outliers in the selected pixels were excluded by using random sample consensus (RANSAC) as RANSAC is a robust method widely used in uniform data with noise (Derpanis, 2010). For the deeper subtidal regions, K_d is not derivable using the spatial method, and R can be approximated to R_w as the seabed has a very limited impact on the surface in the deep waters (Lodhi & Rundquist, 2010).

5.2.2.2 Calculation of chromaticity and dominant wavelength

Chromaticity analysis characterizes the colour of an object as it is perceived by the human eye regardless of its luminance (Bukata et al., 1995), and can be visualized as coordinate pairs in the CIE horseshoe chart (Figure 5.3). The chromaticity coordinates (x, y) can be easily transformed by normalizing tristimulus values (X, Y, Z), as detailed in Equations 3 and 4) (CIE, 1932):

$$x = \frac{X}{X + Y + Z} \tag{3}$$

$$y = \frac{Y}{X + Y + Z} \tag{4}$$

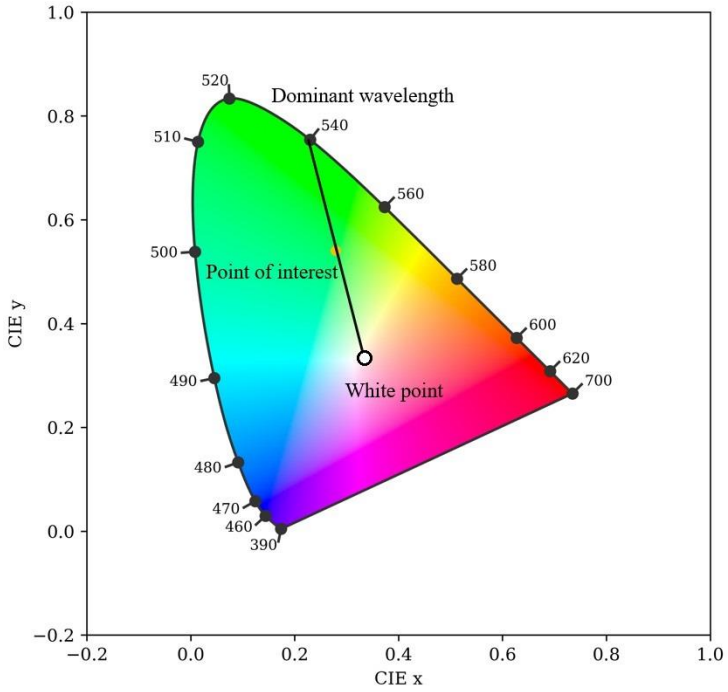

Figure 5. 3 The location of the white point, the point of interest (chromaticity coordinate) and the associated dominant wavelength in the CIE horseshoe chart.

The tristimulus values (X, Y, Z) are calculated as integrals of the upwelling reflectance spectrum, weighted within the range of 390-740 nm, which corresponds to the region sensitive to human eyes (Bukata et al., 1995). Although most satellite remote sensing including Sentinel-2 does not provide full spectral coverage, a multilinear weighted sum of reflectance after correction in visible bands can be used to approximate the tristimulus values (X, Y, Z) (Equation 5 – 7) (Lehmann et al., 2018; Woerd & Wernand, 2015).

$$\mathrm{X} = 6.423R_w(\mathrm{Blue}) + 53.696R_w(\mathrm{Green}) + 32.028R_w(\mathrm{Red}) \quad (5)$$

$$\mathrm{Y} = 22.289R_w(\mathrm{Blue}) + 65.702R_w(\mathrm{Green}) + 16.808R_w(\mathrm{Red}) \quad (6)$$

$$\mathrm{Z} = 31.101R_w(\mathrm{Blue}) + 1.778\,R_w(\mathrm{Green}) + 0.015R_w(\mathrm{Red}) \quad (7)$$

The dominant wavelength, which represents the natural colours of objects in a numeric way, can be calculated based on the chromaticity coordinate pairs. It is the wavelength of pure spectral colour derived as the intersection of the line joining the white point to the point of interest (in the form of Commission Internationale de l'Éclairage (CIE) chromaticity coordinates) in the horseshoe chart (Figure 5.3). To investigate the patterns of optical properties of the selected estuaries, we calculated the K_d Blue and dominant wavelength for each site and transformed them to seasonal or locational results for detailed analysis.

5.2.2.3 Classifying estuaries using K-means clustering

In this study, we used K-means clustering to classify the estuaries based on their dominant wavelength and diffuse attenuation coefficient in band Blue. K-means clustering is a robust unsupervised machine learning method to partition a dataset into distinct groups based on Euclidean distance (Agarwal & Mustafa, 2004). In order to match up the existing water health levels, we set the number of classified groups (K) as 3. Each class corresponds to less impacted, moderately impacted and highly impacted, respectively. In order to confirm the usefulness of such classification, the results were compared to relative datasets such as Benthic Health Model scores (BHM) (Clark et al., 2018) and available photosynthetically active radiation (PAR) (Mangan et al., 2020).

5.3 Results

5.3.1 Dominant wavelength

Clear location-specific differences in dominant wavelength between the estuaries across the North and South Islands of New Zealand were detected. In the North Island, most

estuaries except Manukau showed a broad range of dominant wavelength values approximately spanning from 556 nm to 565 nm, which indicated diverse water colour conditions over five years in each site (Figure 5.4a). In the South Island, especially, Akaroa and Blueskin featured tighter interquartile ranges and thus suggested a more homogenous colour, with the results clustered around 555 to 560 nm and 564 to 568 nm, respectively (Figure 5.4b). Therefore, in general, estuaries from the South Island reflected a yellower colour than those from the North. As to the comparisons among individual sites, Blueskin from the South Island was observed as the yellowest estuary with a median of 567 nm while Mahurangi from the North Island exhibited the lowest median at 555 nm (a greener colour) (Figure 5.4). Despite the site-specific differences, the median values across the locations tend to be relatively uniform, hinting at underlying commonalities in the estuarine water colour of New Zealand.

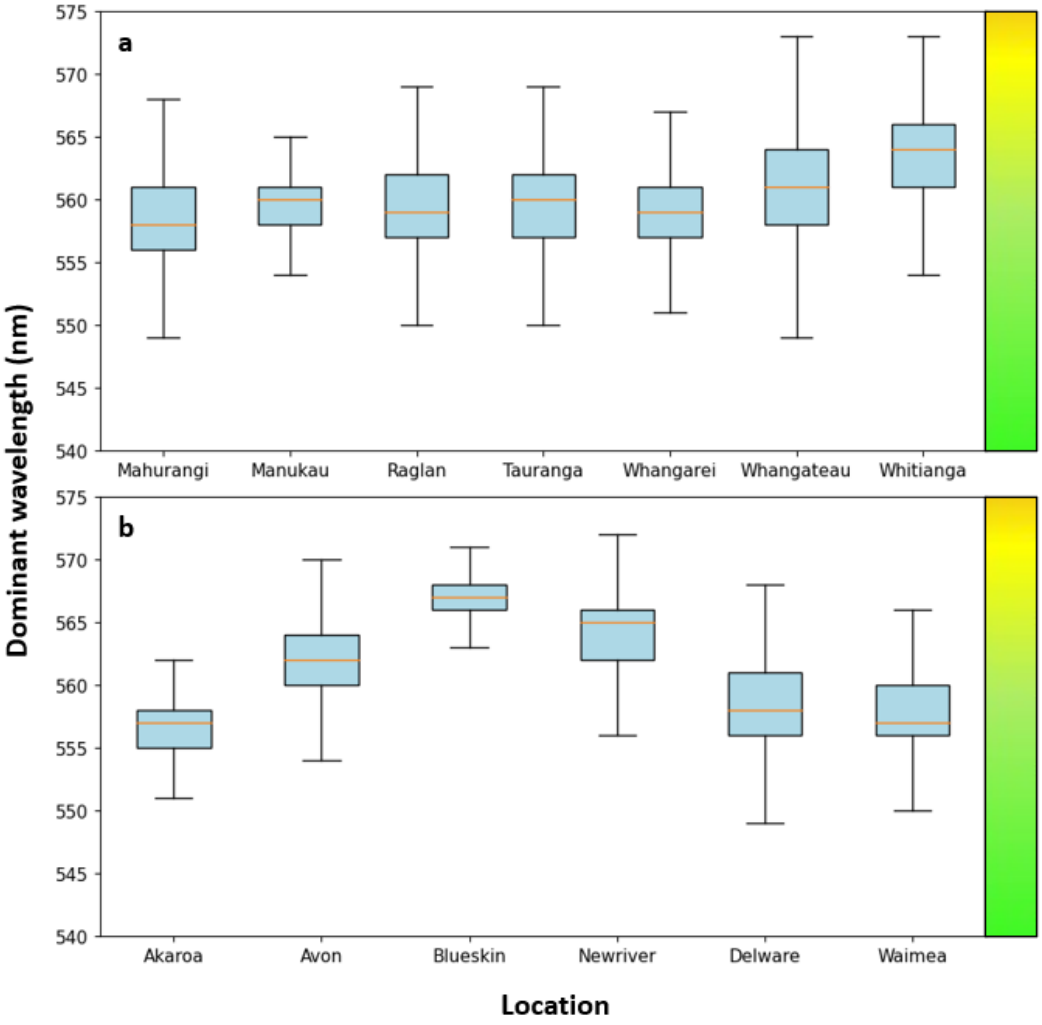

Figure 5. 4 The boxplots of dominant wavelength converted from chromaticity coordinates of each estuary across the North Island (a) and South Island (b) where the scale (right) corresponded to the natural colours. For the pixels in the intertidal regions, seabed correction was applied to each visible band to retrieve the true water reflectance. Note that the dominant wavelength of Blueskin only included the subtidal regions due to the lack of LiDAR data for the intertidal areas.

The variations in the dominant wavelength of most estuaries across New Zealand exhibited evident seasonal patterns. For most estuaries, especially in the South Island, the dominant wavelength reached the peak (green) either in summer or spring and decreased to the lowest (blue) in winter (Figure 5.5). However, Whitianga displayed a noticeable exception with a significant increase from autumn to winter, which was opposite to the regular pattern. The estuaries such as Manukau, Raglan and Tauranga showed relatively

consistent median values throughout the seasons with minimal fluctuations, suggesting a more stable seasonal influence on the dominant wavelength (Figure 5.5). In general, the results indicated that while there were estuary-specific variations, a generic seasonal trend was observed in most locations, with the most evident changes typically occurring in spring and summer.

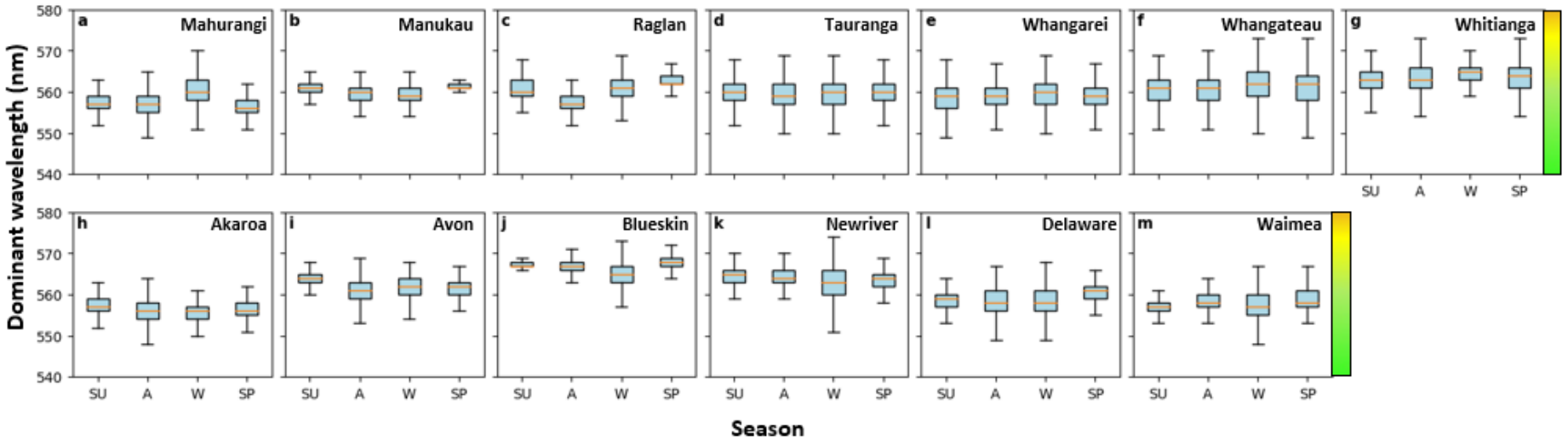

Figure 5. 5 The boxplots of dominant wavelength of each estuary across the North Island (a – g) and South Island (h – f) against seasons, where the scale (right) corresponded to the natural colours. The data were consistent with Figure 5.3. Note SU, A, W and SP represent summer, autumn, winter and spring, respectively.

5.3.2 Diffuse attenuation coefficient (K_d Blue)

The results revealed distinct spatial variability across the studied locations. Opposite to the patterns of dominant wavelength patterns, the diffuse attenuation coefficient (K_d Blue) in the estuaries from the South Island had wider but similar ranges (Figure 5.6). Most sites in the South Island such as Akaroa and Avon had values ranging between 0.24 m^{-1} and 0.74 m^{-1}. Only Waimea showed a relatively narrower range from 0.22 m^{-1} to 0.48 m^{-1}, suggesting clear water conditions. The range of K_d Blue was relatively more unique in each site of the North Island. The smaller estuaries such as Mahurangi had uniform results among all the sites with a range from 0.22 m^{-1} to 0.31 m^{-1}. In contrast, the interquartile range at Raglan, Tauranga, Whangateau and Whitianga suggested a higher variability in water clarity, respectively. Generally, although we observed the highest K_d Blue in Akaroa with a value of 1.32 m^{-1}, the majority of estuaries had a low level of diffuse attenuation with all median values less than 0.5 m^{-1}.

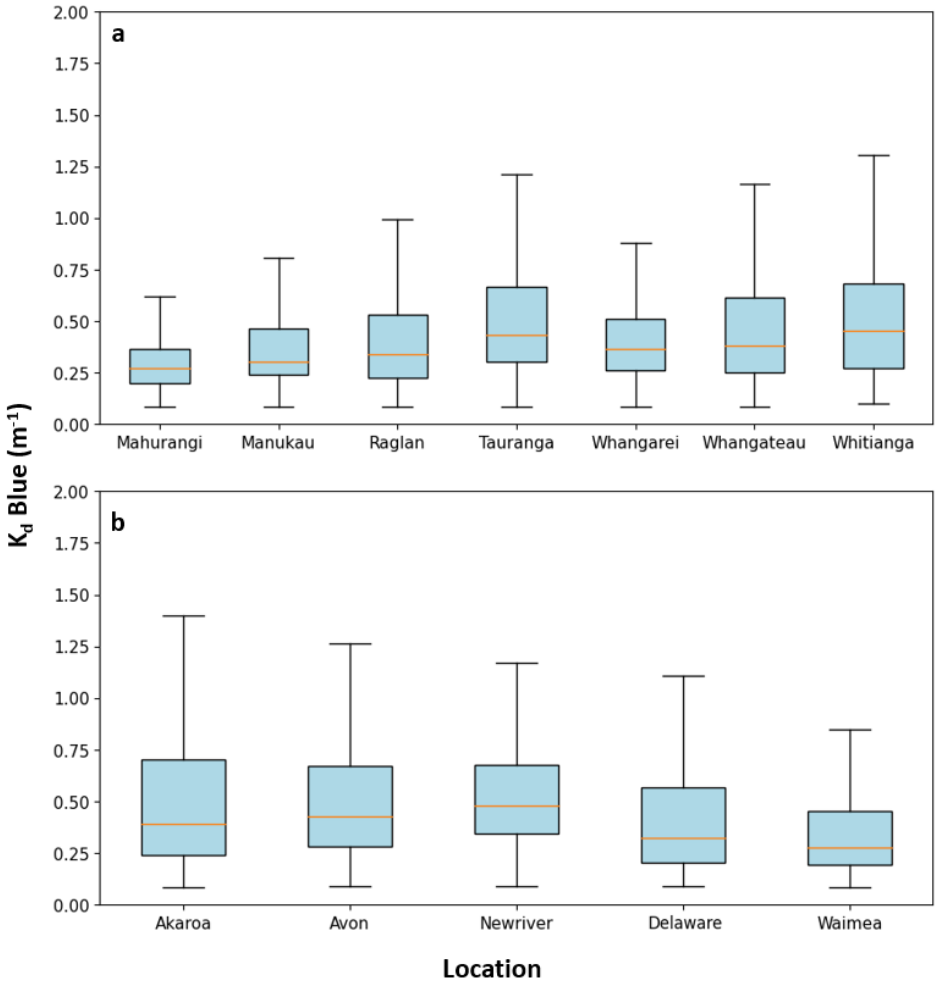

Figure 5. 6 The boxplots of K_d Blue in each estuary across the North Island (a) and South Island (b). Note that due to the lack of LiDAR data for the intertidal regions, able to K_d Blue values from Blueskin could not be derived.

The seasonality of K_d Blue across New Zealand depended on location. Similar to dominant wavelength, the diffuse attenuation coefficient K_d Blue indicated a strong seasonal pattern in most northern sites, which was accompanied by a strong variability in winter. In the North Island, the K_d Blue values decreased to the lowest in summer and the highest in winter in most sites such as Mahurangi, Manukau, Tauranga, and Whangateau (Figure 5.7). Particularly in Tauranga and Whangateau, the variability of K_d Blue in winter was significantly higher than that in other seasons, which was also observed at Avon from the South Island. The seasonality of K_d Blue was less evident in the Southern

Island. Sites like Newriver and Waimea were affected by season where the K_d Blue values remained at similar levels at all times. Although the peaks were observed at both Akaroa and Avon in winter, the K_d Blue values remained at relatively high levels. Another exception we found was Delaware, where in both summer autumn and spring, the estuary exhibited the highest K_d Blue vales.

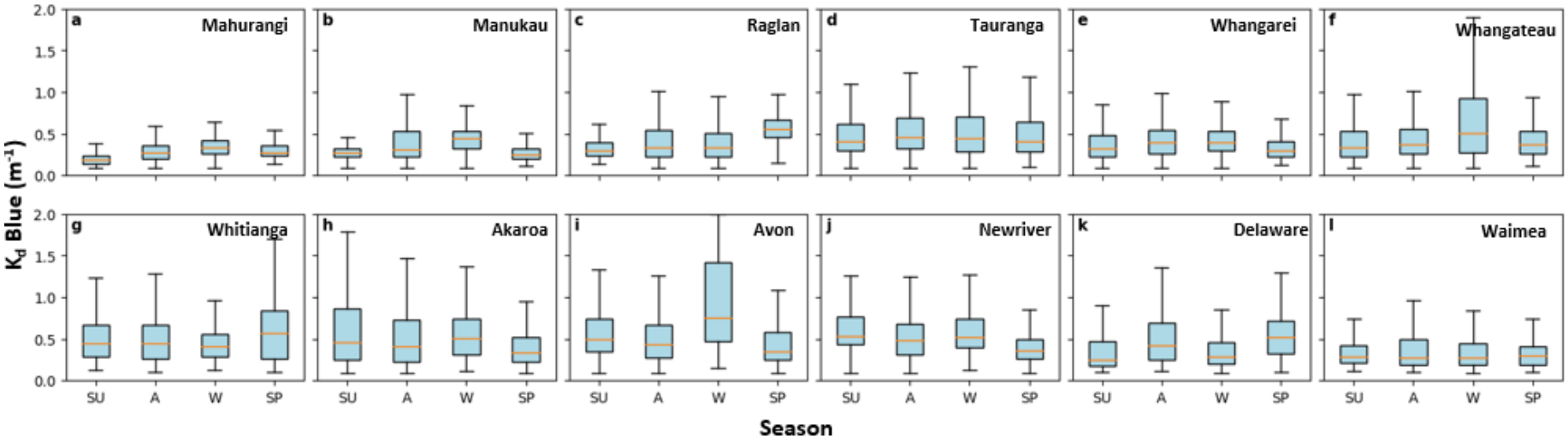

Figure 5. 7 The boxplots of K_d Blue converted corrected reflectance in the intertidal regions of each estuary across the North Island (a – g) and South Island (h – I) against seasons. Note that due to the lack of LiDAR data for the intertidal regions, K_d Blue values could not be derived for Blueskin.

5.3.3 Classifying estuaries using new indicators

The dominant wavelength and K_d Blue clusterings from all sites showed consistent patterns in summer and winter. In summer, the estuaries tended to have higher dominant wavelength values (indicating a yellower colour) but lower K_d Blue values accompanied by reduced variability (Figure 5.8). Conversely, with increased variability of the dominant wavelength of K_d Blue, these estuaries exhibited bluer colours and had higher diffuse attenuation levels in winter (Figure 5.8). Therefore, using the combination of dominant wavelength and K_d Blue was a good indicator to distinguish and classify the data derived from warm and cold seasons.

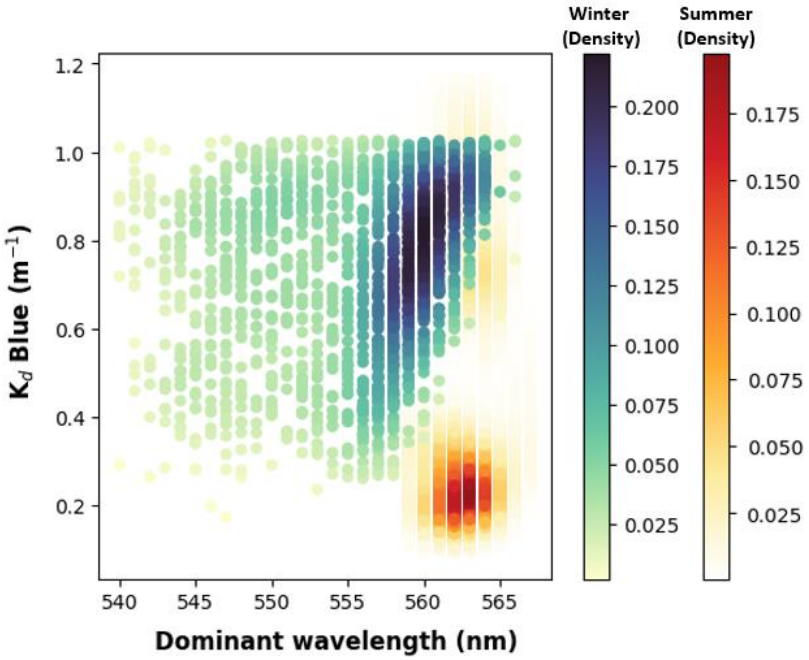

Figure 5. 8 The scatterplots of dominant wavelength against K_d Blue using the data collected at all sites in winter and summer.

Three categories were classified based on the two newly identified optical properties using K-means algorithms: “less impacted”, “moderately impacted” and “highly

impacted" (Figure 5.9c shows the 3 classes). The two highly impacted estuaries, Newriver and Whitianga, were associated with medians of dominant wavelength and K_d Blue exceeding 563 nm and 0.45 m^{-1} (Figure 5.9c), respectively. In contrast, less impacted estuaries such as Mahurangi, Raglan, Waimea, Akaroa and Delaware displayed reduced variability with medians of dominant wavelength and K_d Blue less than 558 nm and 0.4 m^{-1}. Other estuaries were classified as moderately impacted regions characterized by either a yellower colour (e.g. Manukau) or a higher diffuse attenuation level (e.g. Whangarei). Due to the strong seasonal fluctuations in dominant wavelength and K_d Blue, an obvious seasonal variability was observed in several estuaries like Akaroa, Delaware, Tauranga and Whangateau during classification, which led to some whiskers from these estuaries overlapping other categories.

We observed a strong correlation between dominant wavelength and K_d Blue, particularly evident in summer and across the five-year dataset. The correlation coefficients (R) for summer and overall data were 0.72 and 0.83, respectively, with both p-values less than 0.001. However, the correlation was somewhat weaker in winter, with an R value of 0.36 and a p-value less than 0.001. This variation can be attributed to high K_d Blue values observed in Akaroa and Avon, and low dominant wavelength values observed in Whitianga (Figure 5.9c). For long-term monitoring, the relationship between dominant wavelength and K_d Blue offers a relatively accurate method for estimating K_d Blue in deeper channels where Lyzenga's model is less effective (i.e. the deep channels).

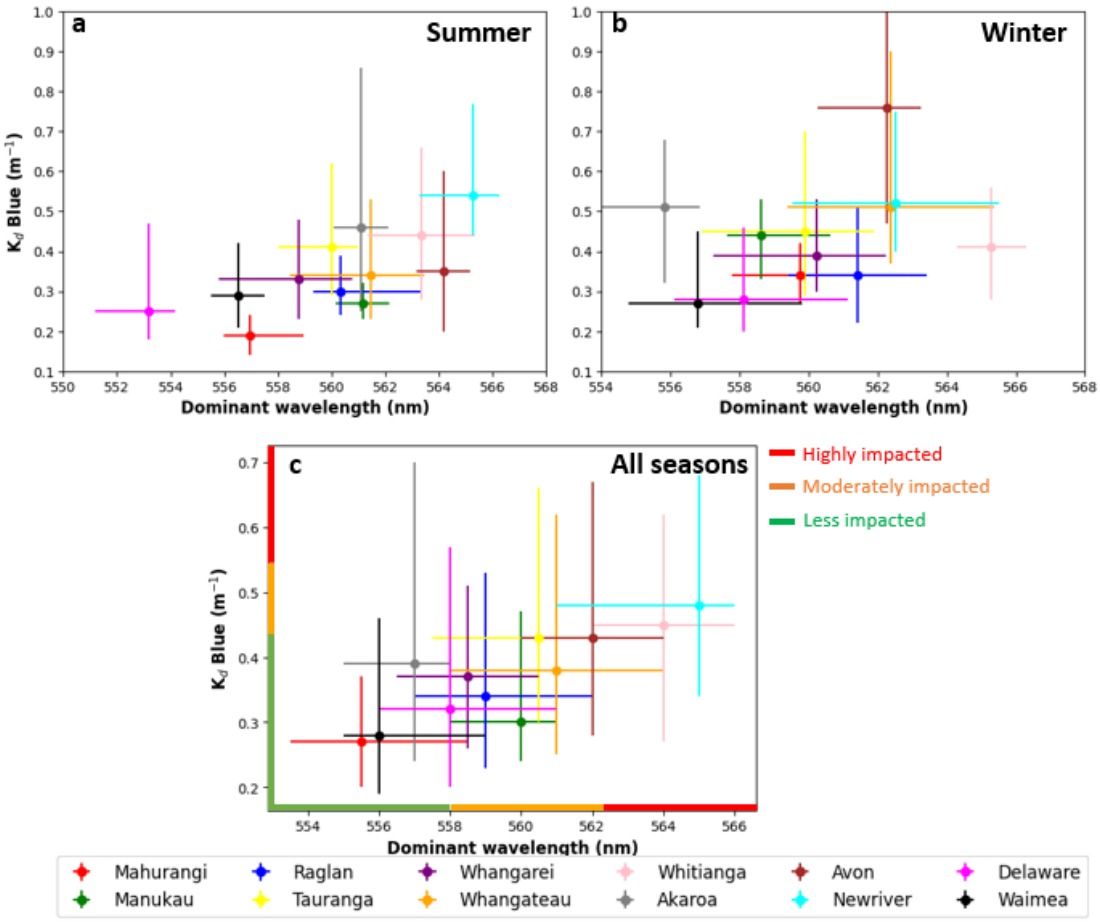

Figure 5. 9 The variability of dominant wavelength and K_d Blue derived from 12 sites in summer (a), winter (b) and all seasons (c). The scatters represented the median while the whiskers represented the 25th and 75th percentiles. K-means clustering was applied to the entire dataset to classify 12 sites into three categories: Highly Impacted, Moderately Impacted and Lowly Impacted. Due to the lack of K_d Blue, Blueskin was not included in the classification.

5.4 Discussion

In this study, we explored the possibility of using dominant wavelength and diffuse attenuation coefficient in band Blue as estuarine health indicators to reflect the water optical properties of 12 estuaries across New Zealand over five years. The selected 12 estuaries possessed different characteristics including turbid, pristine, and mesotrophic. Based on the seasonal and location-specific patterns we observed, both dominant wavelength and K_d Blue were useful in detecting the fluctuations of estuarine optical

properties and classifying estuaries based on these two new indicators. Considering the strong connections between eutrophication and water colour (Li et al., 2021), the continuous monitoring of these two indicators across the country can underpin management actions aimed at, for example, selecting degrading estuaries for restoration or preserving threatened sites from further damage.

The combination of satellite-derived dominant wavelength and K_d as an indicator had some encouraging consistencies with existing monitoring methods such as the benthic health model scores (BHMS) (Clark et al., 2020), *in situ* measured ratio of submerged to emerged photosynthesis active radiation (PAR) between sites (Mangan et al., 2020) and estuary trophic index susceptibility bands (ETISB) (Zeldis & Plew, 2022). BHMS can characterize variations in the structure of macrofaunal communities in response to ecological stressors by applying Canonical Analysis of Principal coordinates on metal and mud data (Clark et al., 2020). The comparisons between the classifications on estuaries derived from our method and BHMS indicated a high consistency with each other such as Raglan, Tauranga, Whangarei, Whangateau, Whitianga, Newriver and Delaware (Figure 5.10). The *in situ* measured ratio of PAR, which reflected the light attenuation and water turbidity, was continuously collected at the intertidal regions of these sites over seven months (Mangan et al., 2020). Our results showed that the same state classifications in Manukau, Tauranga, Whangarei, Whangateau, Avon and Newriver as those derived from the ratio of PAR (Figure 5.10). Similar results were found that most sites returned the same state classifications except Manukau, Raglan, Avon and Waimea (Figure 5.10b) when our classifications were compared to those derived from ETISB, which was converted by ecological factors such as total nitrogen, total phosphorous, sediment loads, heavy metals etc using Bayesian Belief Network (Zeldis & Plew, 2022).

Although the existing indicators do not provide consistent measures, the combination of dominant wavelength and $K_{d\ exhibited}$ the potential of reflecting the general optical properties of estuaries, especially for those with fewer variations in water colours (Figure 5.9). The combination might be less accurate and useful when dominant wavelength or K_d had a particular range such as Akoroa (Figure 5.9).

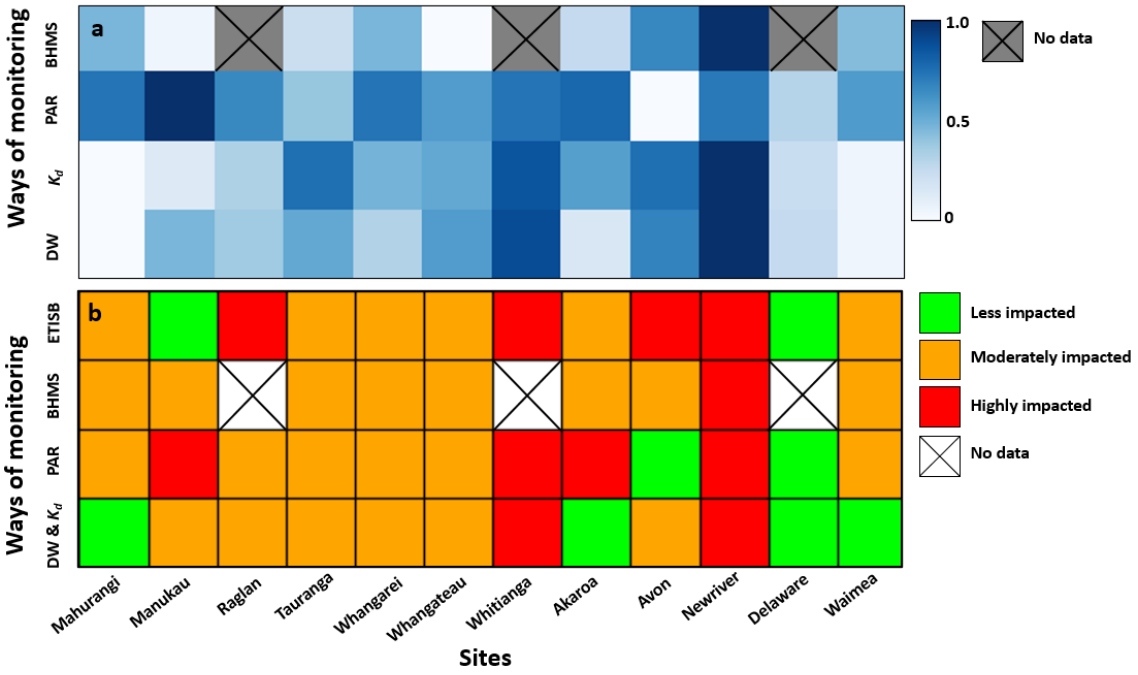

Figure 5. 10 The comparisons of normalized results (a) and states of 12 estuaries using different ways of monitoring (b). The three monitoring ways include the combination of dominant wavelength and K_d Blue (DW & K_d), the in situ measured photosynthesis active radiation (PAR) (Mangan et al., 2020) and the benthic health model scores (BHMs) (Clark et al., 2020) (see Supplementary material 2). Blueskin was not involved due to the lack of K_d Blue data.

Dominant wavelength and K_d can be two useful indicators to measure estuarine optical health considering both indicators integrate the effects of optically active constituents (i.e. chlorophyll-a, CDOM and SSC). Although the ranges of dominant wavelength were site-specific (Figure 5.3), we observed seasonal patterns of dominant wavelength in most estuaries where water colour shifted toward green in summer and returned to blue in

winter (Figure 5.4), which was consistent with the seasonal fluctuations of *in situ* chlorophyll-a concentrations in these estuaries (Fraser et al., 2021). For relatively non-turbid regions, the continuous introduction of CDOM and SSC can also increase the dominant wavelength (turn the colour yellow) (Bowers et al., 2004). Dominant wavelength can also indicate the trophic levels of the waterbody since the estuarine colour is sensitive to algal blooms and scum (water colour turns green) (Zaldívar et al., 2008). As an alternative measure of turbidity and clarity, the variations of K_d can respond to multiple drivers including water temperature and hydrodynamic regimes as well as optically active constituents (Zhao et al., 2013). Our results suggested that K_d mainly increased in warmed winter and spring corresponding to phytoplankton blooms triggered by increased temperatures (Figure 5.6), which can substantially elevate the sediment concentration and thus attenuate the light (Fujiki & Taguchi, 2002). Several studies have successfully used this connection to detect or predict spring blooms with satellite-derived K_d (He et al., 2013; Yang et al., 2020).

Combined with light intensity equations, K_d can be used to estimate the total amount of light (light quantity) and distribution of energy with wavelength (light quality) at the seabed (e.g. Shao et al., 2024). Many studies have emphasised the importance of sufficient light in a relatively turbid estuary as light is the primary condition for photosynthesis (e.g. Mangan et al., 2020). However, to species in intertidal regions such as seagrass and microphytobenthos (MPB), the availability of preferred light at a specific range of wavelengths can determine the photosynthetic process and thus primary productivity (Livingston et al., 1998). For example, seagrass mainly absorbs light optimally at a wavelength less than 500 nm and between 650 nm and 700 nm (Cussioli et al., 2020). Therefore, the K_d values derived in these bands could be extended to estimate

the potential productivity. In addition, by spatially mapping the optimal spectral wavelength range of invasive species such as the exotic seaweed (*Caulerpa brachyurus*), the mapping of areas that may be susceptible to invasion could be a useful tool to safeguard the ecological balance of intertidal ecosystems (Kilroy et al., 2008).

In this study, we showed how to evaluate the estuarine optical properties rapidly using two satellite-derived indicators on a large scale and use this as a basis to classify estuaries into different levels for highly efficient coastal restoration. Although the derivation of the two indicators is limited by the availability of water depth and seabed reflectance data, the observations of dominant wavelength and K_d Blue covered the major areas of the intertidal regions. In a future study, more *in situ* measured dominant wavelength (e.g. using phone cameras, Busch et al., 2016) and diffuse attenuation coefficient data (e.g. using radiometric sensors, Chauhan et al., 2003) can be collected to expand the dataset and thus cover more coastal waters.

5.5 Conclusion

In this study, we used Lyzenga's model to obtain satellite-derived dominant wavelength and diffuse attenuation coefficient in band Blue to assess the optical properties of 12 estuaries across New Zealand, which in turn were used as indicators to classify the estuaries. Although the variations and variability of dominant wavelength and K_d Blue were site-specific, we observed most estuaries indicated a strong but reverse seasonality of the two indicators. Estuaries tend to have higher dominant wavelength values (turn yellower) but lower K_d Blue values (less turbid) in summer and vice versa in winter, which is consistent with the seasonal fluctuations of chlorophyll-a and CDOM. In addition, we found a strong correlation ($R = 0.83$ and $p = 0.001$) between the dominant

wavelength and K_d Blue derived from five-year continuous monitoring, and so dominant wavelength could be used to estimate K_d Blue values in the deep water. Compared with other ways of monitoring, the classification based on dominant wavelength and K_d Blue using K-means clustering returned a high consistency with the *in situ* measured light availability and cohesive sediment concentration. Therefore, satellite-divide optical properties, dominant wavelength and K_d Blue are the two useful and comprehensive indicators to reflect the overall health of estuaries.

Supplementary materials

S1 Complete data of dominant wavelength

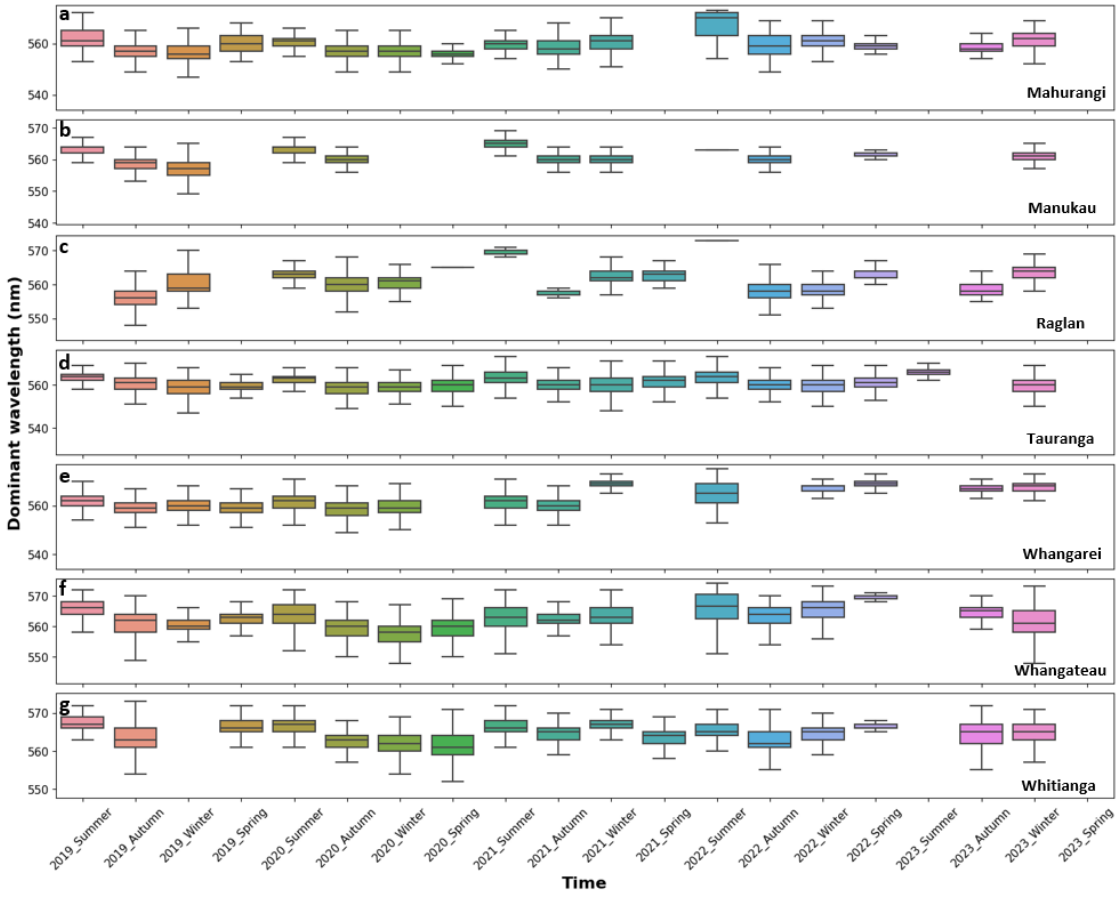

Figure S1. The boxplots of dominant wavelength against seasons from 2019 to 2023 at each site in the North Island. Due to the unavailability of good-quality satellite images, in some seasons, several sites did not present data.

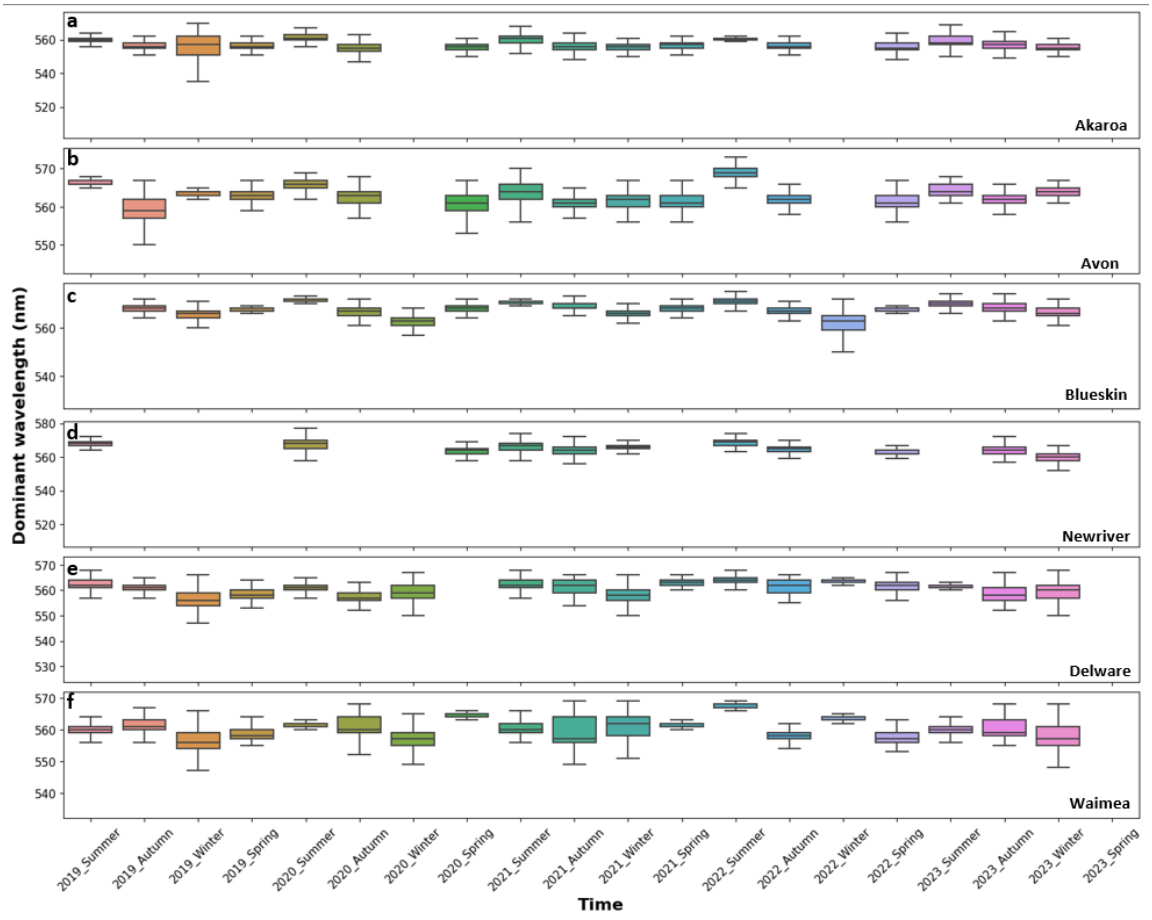

Figure S2. The boxplots of dominant wavelength against seasons from 2019 to 2023 at each site in the South Island. Due to the unavailability of good-quality satellite images, in some seasons, several sites did not present data.

S2 Complete data of K_d Blue

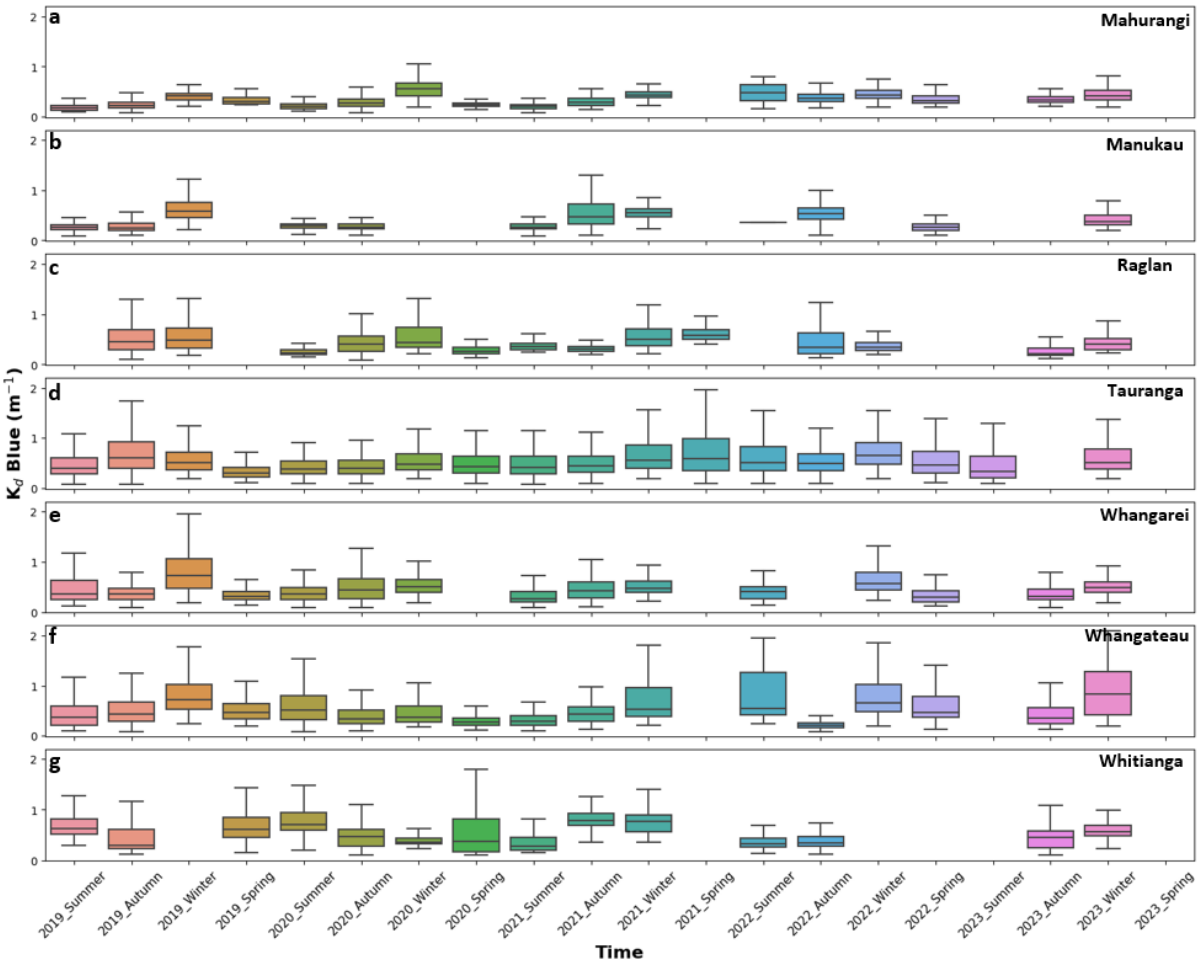

Figure S3. The boxplots of diffuse attenuation coefficient in band blue (K_d Blue) against seasons from 2019 to 2023 at each site in the North Island. Due to the unavailability of good-quality satellite images, in some seasons, several sites did not present data.

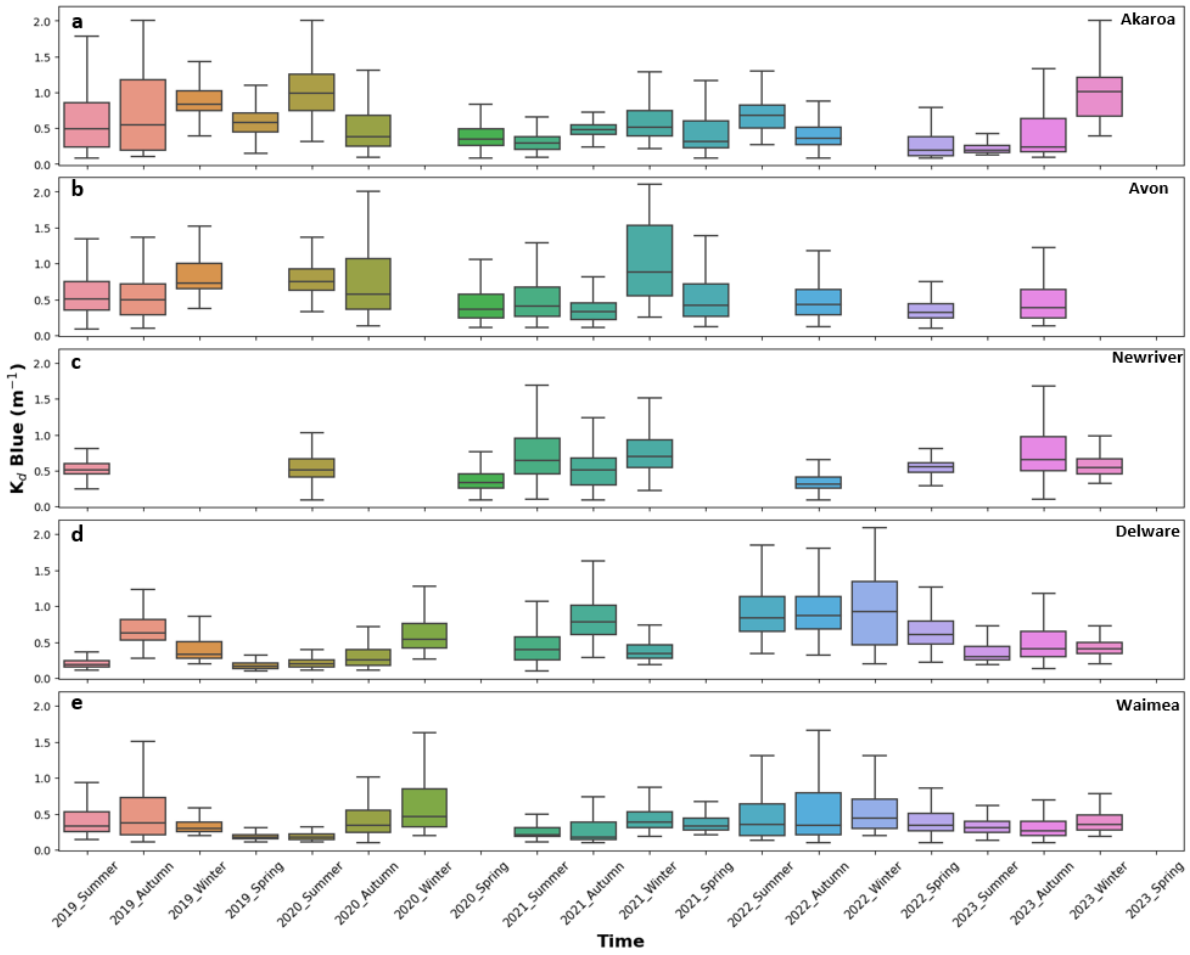

Figure S3. The boxplots of diffuse attenuation coefficient in band blue (K_d Blue) against seasons from 2019 to 2023 at each site in the South Island. Due to the unavailability of good-quality satellite images, in some seasons, several sites did not present data.

S3 States of estuaries based on PAR and BHMS

The states of estuaries based on the ratio of immersed to emerged median PAR were manually classified into three categories (lowly impacted, moderated impacted and highly impacted), which were consistent with those derived from dominant wavelength and K_d Blue (Mangan et al., 2020). The ratios higher than 0.6, between 0.4 and 0.6, and lower than 0.4 were recognized as lowly impacted, moderately impacted and highly impacted estuaries, respectively (Table S1). The data was collected from March to November 2017.

Table S1. The state of each site derived from different ways of monitoring.

Sites	The ratio of immersed to emerged median PAR		Benthic health model scores	
	Value	State	Value	State
Mahurangi	0.43	Moderately impacted	4.2	Moderately impacted
Manukau	0.21	Highly impacted	2.8	Moderately impacted
Raglan	0.43	Moderately impacted	-	-
Tauranga	0.59	Moderately impacted	3.4	Moderately impacted
Whangarei	0.41	Moderately impacted	4.1	Moderately impacted
Whangateau	0.47	Moderately impacted	2.6	Moderately impacted
Whitianga	0.38	Highly impacted	-	-
Akaroa	0.34	Highly impacted	3.5	Moderately impacted
Avon	0.85	Lowly impacted	4.9	Moderately impacted
Newriver	0.38	Highly impacted	Out of limit	Highly impacted
Delaware	0.65	Lowly impacted	-	-
Waimea	0.47	Moderately impacted	4.1	Highly impacted

The states of estuaries based on the benthic health model scores (mud) were originally classified into five categories (Clark et al., 2020). In order to match up the classification we had for this study, we updated the ranges for different categories and obtained three categories. The scores with the ranges of 1.0 – 2.6, 2.7 – 4.3, and 4.4 – 6.0 corresponded to “lowly impacted”, “moderately impacted” and “highly impacted”, respectively. The data provided by the regional councils was collected from 2002 and updated annually.

Chapter 6

Conclusions

6.1 Summary of findings

In this study, I developed several models to monitor the estuarine health indicators (including water colour, diffuse attenuation coefficient, benthic primary productivity and suspended sediment concentration), focused on issues that are particularly important to New Zealand estuaries (Figure 6.1). I used these models to show how this new information could be used as a basis for scaling up benthic primary productivity and fringing wetland sediment accumulation, as case study examples (Figure 6.1). To add to the information derived from satellite imagery, I also used machine learning and numeric modelling. The study focused on two shallow intertidal estuaries — Tauranga Harbour and Ōhiwa Harbour, which have relatively high vegetation (seagrass and mangroves) coverage and significant sediment and nutrient inputs from various discharges, respectively, and both have complex intertidal geomorphologies. Therefore, these two sites are optimal for exploring the temporospatial patterns of estuarine optical properties, benthic primary productivity and sediment transport/settlement in fringing environments. The study in Tauranga Harbour was later expanded to other 12 estuaries across New Zealand to explore the spatial and temporal patterns of water colour and diffuse attenuation. Based on these two indicators, estuaries with similar health states were classified into the same group for consistent management and restoration.

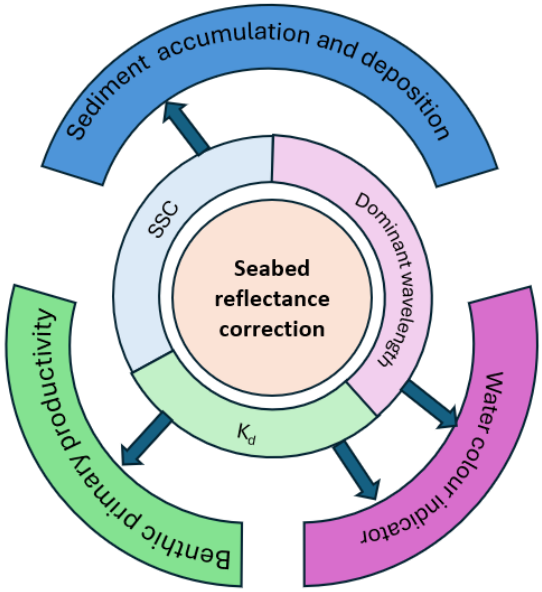

Figure 6. 1 The circular chart showing the logic of the development of different health indicators with the basis of the seabed reflectance correction model.

The extraction of water quality parameters from satellite imagery in intertidal areas is not trivial due to the influence of seabed properties, and developing these techniques underpinned all the outcomes of this research. To achieve this, I introduced two innovative methods based on Lyzenga's model for correcting water reflectance in shallow regions (Chapter 2). While applying these methods necessitated a trade-off between the spatial or temporal resolution of the original images, the resulting reflectances were highly consistent with one other. The models were then utilized to calculate the dominant wavelength and K_d of the water column. I analysed these two indicators over three years during both flood and ebb tides. The findings revealed an evident seasonal fluctuation in the estuary's water colour, aligning with the observed spring bloom. K_d was mainly affected by location because the introduction of extra CDOM from the river discharges might create a gradient to the estuary mouth. However, both indicators indicated that Tauranga Harbour remained in a good state in optical properties from 2018 to 2021. In

addition, the robust correlation between K_d Blue and *in situ* $K_{d\,PAR}$ suggested that K_d Blue could be used as a proxy for routine ecological monitoring at scale. For monitoring estuarine health using satellite data, this chapter is of great importance since the corrected reflectance and available K_d are the foundation of coastal vegetation detection and light estimation.

In the first case study application (Chapter 3), I combined remote sensing and machine learning to develop a detection model for seagrass coverage and unvegetated flats which showed high accuracy. By referencing productivity-irradience curves (*P-I* curves) derived from the literature, the model could provide a detailed spatial map of gross primary productivity (GPP) with the input of water depth, available light and $K_{d\,PAR}$. The model successfully captured the hotspots of GPP and their variations with time. The distribution of hotspots was consistent with the distribution of seagrass because MPB in the unvegetated flats was much less productive. However, for the entire Tauranga Harbour, the dominant contributor to the total GPP depended on location and season. Seagrass usually contributed more in warm seasons, especially in the northern and middle Habour while MPB GPP was highest in the southern Habour due to the decent distribution of unvegetated flats. By adjusting the water depth and K_d, projections using this model could describe the effect of sea level rise and climate change on the current dominant role of seagrass. Seagrass might suffer a significant loss as a high frequency of extreme events could lead to sediment resuspension and thus increase water turbidity substantially. Therefore, keeping the current water clarity is key to mitigating GPP losses from sea level rise and climate change.

In the second case study application, I attempted a primary trial of combining numeric simulation (Delft3D-Flow), remote sensing and random forest machine learning to

predict the incoming cohesive sediment concentration (C_0) and used this as a basis to simulate the sediment accumulation using different assumptions and models. The prediction model I developed in this chapter could be used to understand the sediment budget in the fringing coastal wetlands and thus help coastal management. The estimates from the prediction model were consistent with the short-term and long-term *in situ* measurements, which implied that the technique could be used for estuarine monitoring over an extended period. After applying the various C_0 values (derived from constant, linear, Delft3D and the prediction model) to four accumulation models (Krone's, Temmerman's, $C_{out = 0}$ and $C_{out\ variable}$), I found that the variability in C_0 could result in great differences when different sediment accumulation models were applied. The accumulated sediments varied from 1.13 mm/yr to 3.70 mm/yr, which was substantial considering the sea level rise in this area of New Zealand is about 4.2 mm/yr. Therefore, using a real-time prediction with the combination of *in situ* measurements and spatial observation could help reduce the biases in prediction.

To wrap the thesis up, the final Chapter showed how these new water quality measurements could be used to compare and benchmark estuaries over scale. Twelve estuaries across New Zealand were selected to be classified based on the satellite-derived dominant wavelength and K_d Blue using the seabed correction model proposed in Chapter 2. I found that although the variability of dominant wavelength and K_d Blue was site-specific, most estuaries exhibited strong but reverse seasonal patterns in dominant wavelength and K_d Blue, which provided an opportunity to cluster the results from all estuaries into summer and winter. In addition, a significant correlation (R = 0.83) was observed between the dominant wavelength and K_d Blue, which could be used to estimate the values when the other was not derivable (e.g. in the deep channels where seabed

reflectance and water depth were not available). Based on these results, thirteen estuaries were grouped into “less impacted”, “moderately impacted” and “highly impacted”. The most impacted sites included Newriver and Whitianga while Akaroa, Delaware and Waimea remained in a heathy state. The derived classifications were later compared to other *in situ* measurements (e.g. light availability, Mangan et al., 2020) and judging criteria (e.g. benthic health model scores, Clark et al., 2020). The results showed that the satellite-derived classification indicated a relatively high consistency with other datasets. Therefore, it was likely to apply dominant wavelength and diffuse attenuation coefficient to monitor the estuarine health at scale as two new optical properties.

6.2 Suggestions for future research

In Chapter 2, especially when using the “spatial method”, multiple observations of the same water at different water depths were needed to develop the correction for seabed effects. For this, I assumed that the seabed and water optical properties do not vary substantially among the selected pixels in the tiles. Therefore, the occasional introduction of pixels from different objects might influence the uniformity. Instead of manually categorising the pixels into different classes, a classification model (e.g. Luo et al., 2019), which can detect the objects during exposure and submergence based on their visible bands, could be helpful in excluding the pixels of different land covers in the tile and thus maintaining uniformity.

Another suggestion is to improve the accuracy of estimating seabed reflectance (R_b) in the intertidal/subtidal regions. One possible method is to conduct seasonal *in situ* measurements using spectral radiometers or underwater photographs, which could be converted to reflectance at a specific wavelength (such as blue, green or red) (Hochberg

& Atkinson, 2003). This approach promises to mitigate the influence of temporal variations in the vegetation-covered seabed like seagrass and *Ulva*. Several other studies reference Hydrolight to simulate the reflectance of seabeds either using the default settings or mixtures of different bottom types (Ma et al., 2021; Wang et al., 2022). Together with the classification model, this method is likely to reduce the bias on R_b estimates and thus improve the accuracy.

Water depth can also contribute errors to the correction model. Although the hydrodynamics model derived from Delft3D can return accurate tidal heights (Stewart, 2021), the complex setup and long processing time might restrict the application of the correction model. Therefore, using the satellite-based water depth retrieval algorithm could be a good replacement. Due to the high penetration, the ratio of reflectance between blue and green is widely used to estimate the bathymetry in the optically deep channels by establishing empirical relationships with *in situ* measurements (Jagalingam et al., 2015) or applying Stumpf's band ratio model (Stumpf et al., 2003; Zhu et al., 2020). For shallow waters, the new machine learning based method using visible bands and near-infrared bands yields robust bathymetric estimates (Sagawa et al., 2019), which can provide a complete distribution map of water depth in the intertidal regions.

In Chapter 3, improvements could be made by increasing the accuracy of predicting seagrass area when submerged and modelling the potential seagrass distribution trend. Although the results showed water depth did not significantly affect the detection accuracy, seagrass coverage might be biased due to the effects of the water column on reflectance. Therefore, rather than using absolute values of seagrass reflectance, applying the bottom reflectance index (BRI) converted from visible bands (Sagawa et al., 2010), which creates different indexes for different seabed types (Ha et al., 2020), is likely to

increase the detection model's performance. Meanwhile, more ground truth points should be collected over the subtidal regions to be compared with the machine learning model derived results, which will be particularly important if seagrass continues to thrive and expand. For the prediction of future benthic primary productivity, instead of adding the restrictions of light and averaged annual growth area to seagrass, a model which can provide expansion/degradation details of seagrass based on current distribution would be much more accurate. Several parameters may contribute to this model including heatwaves (Clemente et al., 2023), nutrients (Li et al., 2019), natural events (Cussioli et al., 2019), as well as light availability (Bulmer et al., 2016).

More biological effects from the surrounding environment and ecophysiological adaptations from both seagrass and MPB could be included in estimating productivity. For example, the increased mud content can significantly reduce the photosynthetic efficiency of MPB while seagrass is barely affected (Flowers et al., 2023). Seagrass can also adapt to limited light conditions by changing pigment compositions and up-regulate productivity to compensate for lack of energy (Davey et al., 2018; Keyzer et al., 2020). The MPB communities instead are able to tolerate the wide temperate variation (Salleh & McMinn, 2021) and desiccation (Coelho et al., 2009). These factors were ignored in my model but were worthwhile adding in future studies for more accurate GPP estimates.

In Chapter 4, considering the accuracy of the prediction model strongly depends on the satellite observation, it is of great importance to develop better algorithms to estimate SSC, especially in shallow waters. Several methods may useful than the method I used, such as applying end-to-end neural interpolation on satellite images (Vient et al., 2022), extracting the amplitudes and phases of SSC through coupling the Lomb-Scargle Periodogram with phase-folded diagrams (Lin et al., 2022) and using the empirical model

based band ratio (Red/Green) (Markert et al., 2018). These methods all returned accurate estimates of SSC, which can provide a solid basis for predicting cohesive sediment concentration in the fringing environments of estuaries.

More features can be included in the prediction model to improve the accuracy of C_0. The model did not include rainfall (extreme weather), waves and human effects, which are all significant contributors to hydrodynamic conditions and thus sediment concentration variations. Therefore, future projects can be connected to meteorological models (Sokol et al., 2021) and quantify the anthropogenic effects on estuarine sediments (Grasso et al., 2021). The cohesive sediment concentration should be derived from the wave model of Delft3D, which fully considers the effect of waves on sediment dynamics.

In Chapter 5, the results showed that dominant wavelength and K_d Blue could be used to classify the states of 12 estuaries across New Zealand. Although I compared the results with other *in situ* measurements and evaluation models, more detailed criteria should be added to the classification model to avoid errors due to seasonal variations in water properties. Fieldwork on measuring the water colour and diffuse attenuation should also be carried out to assess and correct the errors from satellite-derived results. In addition, more estuaries should be involved in the study so that a nationwide classification system can be established to provide instant and relatively precise results of estuarine optical properties.

6.3 Conclusions

Due to anthropogenic stress, the coastal environment is currently under immense pressure which continues to worsen with climate change, increased pollution and decreased

biodiversity. Enormous economic and biological loss may come rapidly with the degradation of coastal habitats, made worse by the loss of resilience in the human communities and natural ecosystems. Therefore, there is a clear need for us to change the way we interact with the environment. The effects of human behaviours and natural processes need to be numerically quantified using *in situ* and remote sensing measures, to provide strong evidence to incite behavioural change. With the support of great data at scale, using health indices derived from multiple coastal stressors and indicators can be the basis for a comprehensive assessment of coastal waters. The quantified changes in estuarine indicators can provide coastal restoration teams with precise and locally-relevant tools, enabling timely and effective intervention and the data to persuade local communities to actively participate in protective actions.

The research chapters above provided a comprehensive understanding of estuarine health derived from the combination of satellite images, machine learning and numerical simulation. The main thesis outcome was to assess estuarine health based on different criteria including water optical properties, surrounding vegetation health and coastal sediment budget. The key innovations and findings from this study were:

- The development of a seabed reflectance correction model based on Lyzenga's algorithms. The seabed reflectance correction model provided a simple way to calculate the true water reflectance in visible bands in optically shallow regions, which was the basis for deriving water surface optical properties accurately. Based on the assumptions I made, the diffuse attenuation coefficient could be computed by applying the "spatial" or "temporal" method.
- The development of a new machine-learning-based model to estimate seagrass percentage coverage, unvegetated flat distribution and thus benthic primary

productivity. Due to the application of machine learning, the model was the first model which could provide accurate estimates of the areas of seagrass and other vegetation. By combining satellite images, random forest models and literature-derived photosynthesis parameters, this model filled an important gap in how to upscale empirical $P - I$ relationships derived from limited samples to a spatial distribution map of productivity. By adjusting the water depth and diffuse attenuation coefficient, this model could be further used to predict the impacted GPP due to sea level rise and climate change.

- The derivation of the incoming cohesive sediment concentration. In this chapter, a new model to estimate the cohesive sediment concentration and to predict sediment accumulation in the fringing environment was proposed using a combination of satellite imagery, machine learning and numerical simulation (Delft3D). Although previous studies explored the possibility of assimilating satellite-derived data into numeric models to provide complete and long monitoring of SSC, the new prediction model could predict spatially-resolved sediment dynamics precisely and quickly. In addition, this chapter was also the first to investigate how sediment accumulation in simple wetland models was sensitive to the parameterisation of SSC of the incoming estuarine water.
- The classification of estuaries across New Zealand based on dominant wavelength and diffuse attenuation coefficient. There are limited papers on classifying estuaries using two satellite-derived optical properties. Many previous studies focused on one index or indicator, which can not convey complete information about the estuaries. Classifying estuaries with similar optical conditions into groups can contribute to consistent coastal management and restoration of benthic

vegetation because dominant wavelength and diffuse attenuation coefficient control the light availability at the seabed.

- The models developed in this study are generally applicable to other sites, and so can contribute to a more complete understanding of estuarine health on which to base more accurate predictions for other estuaries.

References

Agarwal, P. K., & Mustafa, N. H. (2004). K-means projective clustering. Proceedings of the twenty-third ACM SIGMOD-SIGACT-SIGART symposium on Principles of database systems,

Albert, A., & Mobley, C. D. (2003). An analytical model for subsurface irradiance and remote sensing reflectance in deep and shallow case-2 waters. *Optics Express*, *11*(22), 2873-2890.

Allen, G. P., Salomon, J., Bassoullet, P., Du Penhoat, Y., & De Grandpre, C. (1980). Effects of tides on mixing and suspended sediment transport in macrotidal estuaries. *Sedimentary Geology, 26*(1-3), 69-90.

Ansari, M., & Akhoondzadeh, M. (2020). Mapping water salinity using Landsat-8 OLI satellite images (Case study: Karun basin located in Iran). *Advances in Space Research, 65*(5), 1490-1502.

Arce, G. R. (2005). *Nonlinear signal processing: a statistical approach*. John Wiley & Sons.

Ask, J., Rowe, O., Brugel, S., Strömgren, M., Byström, P., & Andersson, A. (2016). Importance of coastal primary production in the northern Baltic Sea. *Ambio, 45*, 635-648.

Astuti, I. S., Mishra, D. R., Mishra, S., & Schaeffer, B. (2018). Spatio-temporal dynamics of inherent optical properties in oligotrophic northern Gulf of Mexico estuaries. *Continental Shelf Research, 166*, 92-107.

Baek, S. S., Pyo, J., Kwon, Y. S., Chun, S.-J., Baek, S. H., Ahn, C.-Y., Oh, H.-M., Kim, Y. O., & Cho, K. H. (2021). Deep learning for simulating harmful algal blooms using ocean numerical model. *Frontiers in Marine Science, 8*, 729954.

Bailey, S. W., & Werdell, P. J. (2006). A multi-sensor approach for the on-orbit validation of ocean color satellite data products. *Remote Sensing of Environment, 102*(1-2), 12-23.

Ball, D., Soto-Berelov, M., & Young, P. (2014). Historical seagrass mapping in Port Phillip Bay, Australia. *Journal of Coastal Conservation*, *18*, 257-272.

Barillé, L., Mouget, J. L., Méléder, V., Rosa, P., & Jesus, B. (2011). Spectral response of benthic diatoms with different sediment backgrounds. *Remote sensing of Environment*, *115*(4), 1034-1042.

Bianchi, T. S. (2011). The role of terrestrially derived organic carbon in the coastal ocean: A changing paradigm and the priming effect. *Proceedings of the National Academy of Sciences, 108*(49), 19473-19481.

Binding, C. E., Jerome, J. H., Bukata, R. P., & Booty, W. G. (2008). Spectral absorption properties of dissolved and particulate matter in Lake Erie. *Remote Sensing of Environment, 112*(4), 1702-1711.

Björk, M., Short, F., Mcleod, E., & Beer, S. (2008). *Managing seagrasses for resilience to climate change* (No. 3). Iucn.

Bordovskiy, O. (1965). Accumulation of organic matter in bottom sediments. *Marine Geology, 3*(1-2), 33-82.

Borkman, D. G., & Smayda, T. J. (1998). Long-term trends in water clarity revealed by Secchi-disk measurements in lower Narragansett Bay. *ICES Journal of Marine Science, 55*(4), 668-679.

Borrelli, P., Robinson, D. A., Panagos, P., Lugato, E., Yang, J. E., Alewell, C., Wuepper, D., Montanarella, L., & Ballabio, C. (2020). Land use and climate change impacts on global soil erosion by water (2015-2070). *Proceedings of the National Academy of Sciences, 117*(36), 21994-22001.

Boss, E., Taylor, L., Gilbert, S., Gundersen, K., Hawley, N., Janzen, C., Johengen, T., Purcell, H., Robertson, C., & Schar, D. W. (2009). Comparison of inherent optical properties as a surrogate for particulate matter concentration in coastal waters. *Limnology and Oceanography: Methods, 7*(11), 803-810.

Bouma, T., Van Duren, L., Temmerman, S., Claverie, T., Blanco-Garcia, A., Ysebaert, T., & Herman, P. (2007). Spatial flow and sedimentation patterns within patches of epibenthic structures: Combining field, flume and modelling experiments. *Continental Shelf Research, 27*(8), 1020-1045.

Bowers, D. G., Evans, D., Thomas, D. N., Ellis, K., & Williams, P. J. l. B. (2004). Interpreting the colour of an estuary. *Estuarine, Coastal and Shelf Science, 59*(1), 13-20. https://doi.org/10.1016/j.ecss.2003.06.001

Boyer, J. N., Kelble, C. R., Ortner, P. B., & Rudnick, D. T. (2009). Phytoplankton bloom status: Chlorophyll a biomass as an indicator of water quality condition in the southern estuaries of Florida, USA. *Ecological indicators*, *9*(6), S56-S67.

Breda, A., Saco, P. M., Sandi, S. G., Saintilan, N., Riccardi, G., & Rodríguez, J. F. (2021). Accretion, retreat and transgression of coastal wetlands experiencing sea-level rise. *Hydrology and Earth System Sciences, 25*(2), 769-786.

Breiman, L. (2001). Random forests. *Machine learning, 45*(1), 5-32.

Bricaud, A., Morel, A., & Prieur, L. (1981). Absorption by dissolved organic matter of the sea (yellow substance) in the UV and visible domains. *Limnol. Oceanogr, 26*(1), 43-53.

Brezonik, P. L., Bouchard Jr, R. W., Finlay, J. C., Griffin, C. G., Olmanson, L. G., Anderson, J. P., ... & Hozalski, R. (2019). Color, chlorophyll a, and suspended solids effects on Secchi depth in lakes: implications for trophic state assessment. *Ecological Applications*, *29*(3), e01871.

Bukata, R. P., Jerome, J. H., Kondratyev, A. S., & Pozdnyakov, D. V. (1995). *Optical properties and remote sensing of inland and coastal waters*. CRC press.

Bulmer, R., Kelly, S., & Jeffs, A. (2016). Light requirements of the seagrass, Zostera muelleri, determined by observations at the maximum depth limit in a temperate estuary, New Zealand. *New Zealand Journal of Marine and Freshwater Research, 50*(2), 183-194.

Bulmer, R. H., Townsend, M., Drylie, T., & Lohrer, A. M. (2018). Elevated turbidity and the nutrient removal capacity of seagrass. *Frontiers in Marine Science*, *5*, 462.

Busch, J. A., Price, I., Jeansou, E., Zielinski, O., & van der Woerd, H. J. (2016). Citizens and satellites: Assessment of phytoplankton dynamics in a NW Mediterranean aquaculture zone. *International Journal of Applied Earth Observation and Geoinformation, 47*, 40-49.

Caballero, I., Steinmetz, F., & Navarro, G. (2018). Evaluation of the first year of operational Sentinel-2A data for retrieval of suspended solids in medium-to high-turbidity waters. *Remote Sensing, 10*(7), 982.

Cahoon, L. B. (2002). The role of benthic microalgae in neritic ecosystems. In *Oceanography and marine biology* (pp. 55-94). CRC Press.

Carstensen, J., Krause-Jensen, D., & Balsby, T. J. (2016). Biomass-cover relationship for eelgrass meadows. *Estuaries and coasts*, *39*, 440-450.

Chao, X., Jia, Y., Shields Jr, F. D., Wang, S. S., & Cooper, C. M. (2008). Three-dimensional numerical modeling of cohesive sediment transport and wind wave impact in a shallow oxbow lake. *Advances in Water Resources, 31*(7), 1004-1014.

Chauhan, P., Sahay, A., Rajawat, A., & Nayak, S. (2003). Remote sensing of diffuse attenuation coefficient (K490) using IRS-P4 Ocean Colour Monitor (OCM) sensor.

Chen, W., Wang, D., Liu, X., Cheng, J., & Zhang, J. (2022). Improve the Accuracy in Numerical Modeling of Suspended Sediment Concentrations in the Hangzhou Bay by Assimilating Remote Sensing Data Utilizing Combined Techniques of Adjoint Data Assimilation and the Penalty Function Method. *Remote Sensing, 15*(1), 148.

Chiarelli, A.M.; Low, K.A.; Maclin, E.L.; Fletcher, M.A.; Kong, T.S.; Zimmerman, B.; Tan, C.H.; Sutton, B.P.; Fabiani, M.; Gratton, G. (2019). Ocean optics protocols for SeaWiFS validation. *Photonics*, *6*, 79

Chen, Y., Li, Y., Cai, T., Thompson, C., & Li, Y. (2016). A comparison of biohydrodynamic interaction within mangrove and saltmarsh boundaries. *Earth Surface Processes and Landforms, 41*(13), 1967-1979.

Chen, Y., Thompson, C., & Collins, M. (2012). Saltmarsh creek bank stability: biostabilisation and consolidation with depth. *Continental Shelf Research, 35*, 64-74.

CIE. (1932). Commission Internationale de l'Éclairage Proceedings. (Cambridge University Press).

Clark, D., Hewitt, J., Pilditch, C., & Ellis, J. (2020). The development of a national approach to monitoring estuarine health based on multivariate analysis. *Marine Pollution Bulletin, 150*, 110602.

Clark, D., Taiapa, C., Sinner, J., Taikato, V., Culliford, D., Battershill, C. N., Ellis, J. I., Hewitt, J. E., Gower, F., & Borges, H. (2018). 2016 Subtidal Ecological Survey of Tauranga Harbour and development of benthic health models.

Claverie, M., Ju, J., Masek, J. G., Dungan, J. L., Vermote, E. F., Roger, J.-C., Skakun, S. V., & Justice, C. (2018). The Harmonized Landsat and Sentinel-2 surface reflectance data set. *Remote Sensing of Environment, 219*, 145-161.

Clavier, J., Chauvaud, L., Carlier, A., Amice, E., Van der Geest, M., Labrosse, P., ... & Hily, C. (2011). Aerial and underwater carbon metabolism of a Zostera noltii seagrass bed in the Banc d'Arguin, Mauritania. *Aquatic Botany*, *95*(1), 24-30.

Clemente, K. J. E., Thomsen, M. S., & Zimmerman, R. C. (2023). The vulnerability and resilience of seagrass ecosystems to marine heatwaves in New Zealand: a remote sensing analysis of seascape metrics using PlanetScope imagery. *Remote Sensing in Ecology and Conservation*.

Cloern, J. E., Abreu, P. C., Carstensen, J., Chauvaud, L., Elmgren, R., Grall, J., Greening, H., Johansson, J. O. R., Kahru, M., & Sherwood, E. T. (2016). Human activities

and climate variability drive fast-paced change across the world's estuarine–coastal ecosystems. *Global Change Biology, 22*(2), 513-529.

Coelho, H., Vieira, S., & Serôdio, J. (2009). Effects of desiccation on the photosynthetic activity of intertidal microphytobenthos biofilms as studied by optical methods. *Journal of Experimental Marine Biology and Ecology, 381*(2), 98-104.

Cooper, H. M., Zhang, C., Davis, S. E., & Troxler, T. G. (2019). Object-based correction of LiDAR DEMs using RTK-GPS data and machine learning modeling in the coastal Everglades. *Environmental modelling & software*, *112*, 179-191.

Costanza, R., De Groot, R., Sutton, P., Van der Ploeg, S., Anderson, S. J., Kubiszewski, I., Farber, S., & Turner, R. K. (2014). Changes in the global value of ecosystem services. *Global environmental change, 26*, 152-158.

Crawshaw, J, Park, S., Medina, R. Hawes, I., McDougal, M. (2023). Seagrass Dynamics in the Bay of Plenty. *Bay of Plenty Regional Council. Environmental Publication* 2023/10.

Cussioli, M. C., Bryan, K. R., Pilditch, C. A., de Lange, W. P., & Bischof, K. (2019). Light penetration in a temperate meso-tidal lagoon: implications for seagrass growth and dredging in Tauranga Harbour, New Zealand. *Ocean & Coastal Management, 174*, 25-37. https://doi.org/10.1016/j.ocecoaman.2019.01.014

Cussioli, M. C., Seeger, D., Pratt, D. R., Bryan, K. R., Bischof, K., de Lange, W. P., Bornman, J. F., & Pilditch, C. A. (2020). Spectral differences in the underwater light regime caused by sediment types in New Zealand estuaries: implications for seagrass photosynthesis. *Geo-Marine Letters*, 1-9.

Daggers, T. D., Kromkamp, J. C., Herman, P. M., & van der Wal, D. (2018). A model to assess microphytobenthic primary production in tidal systems using satellite remote sensing. *Remote sensing of environment*, *211*, 129-145.

Davey, P. A., Pernice, M., Ashworth, J., Kuzhiumparambil, U., Szabó, M., Dolferus, R., & Ralph, P. J. (2018). A new mechanistic understanding of light-limitation in the seagrass Zostera muelleri. *Marine environmental research, 134*, 55-67.

Davies-Colley, R. J., Vant, W. N., & Smith, D. G. (2003). *Colour and clarity of natural waters*. Blackburn Press.

Davis, T. R., Harasti, D., Smith, S. D., & Kelaher, B. P. (2016). Using modelling to predict impacts of sea level rise and increased turbidity on seagrass distributions in estuarine embayments. *Estuarine, Coastal and Shelf Science*, *181*, 294-301.

Davies, K. (2015). *Many voices of the Manukau: Participatory modelling, ecosystem services and decision making in New Zealand* Research Space at Auckland.

Dehkordi, A. T., Ghasemi, H., & Zoej, M. J. V. (2021). Machine Learning-Based Estimation of Suspended Sediment Concentration along Missouri River using Remote Sensing Imageries in Google Earth Engine. 2021 7th International Conference on Signal Processing and Intelligent Systems (ICSPIS),

Derpanis, K. G. (2010). Overview of the RANSAC Algorithm. *Image Rochester NY, 4*(1), 2-3.

Dimitriadis, P., Koutsoyiannis, D., Iliopoulou, T., & Papanicolaou, P. (2021). A global-scale investigation of stochastic similarities in marginal distribution and dependence structure of key hydrological-cycle processes. *Hydrology*, *8*(2), 59.

Doglioli, A. M., Griffa, A., & Magaldi, M. G. (2004). Numerical study of a coastal current on a steep slope in presence of a cape: The case of the Promontorio di Portofino. *Journal of Geophysical Research: Oceans, 109*(C12).

Donatelli, C., Ganju, N. K., Fagherazzi, S., & Leonardi, N. (2018). Seagrass impact on sediment exchange between tidal flats and salt marsh, and the sediment budget of shallow bays. *Geophysical Research Letters, 45*(10), 4933-4943.

Douglas, E. J., Pilditch, C. A., Lohrer, A. M., Savage, C., Schipper, L. A., & Thrush, S. F. (2018). Sedimentary environment influences ecosystem response to nutrient enrichment. *Estuaries and coasts*, *41*, 1994-2008.

Douglas, G., Caitcheon, G., & Palmer, M. (2009). Sediment source identification and residence times in the Maroochy River estuary, southeast Queensland, Australia. *Environmental Geology, 57*, 629-639.

Doxaran, D., Froidefond, J.-M., Castaing, P., & Babin, M. (2009). Dynamics of the turbidity maximum zone in a macrotidal estuary (the Gironde, France): Observations from field and MODIS satellite data. *Estuarine, Coastal and Shelf Science, 81*(3), 321-332.

Droppo, I. G. (2001). Rethinking what constitutes suspended sediment. *Hydrological processes, 15*(9), 1551-1564.

Drylie, T. P., Lohrer, A. M., Needham, H. R., Bulmer, R. H., & Pilditch, C. A. (2018). Benthic primary production in emerged intertidal habitats provides resilience to high water column turbidity. *Journal of sea research*, *142*, 101-112.

Duarte, C. M., Losada, I. J., Hendriks, I. E., Mazarrasa, I., & Marbà, N. (2013). The role of coastal plant communities for climate change mitigation and adaptation. *Nature climate change*, *3*(11), 961-968.

Dudley, B., Zeldis, J., & Brurge, O. (2017). New Zealand Coastal Water Quality Assessment *NIWA Client Report 2016093CH*.

Elias, E. P., Van der Spek, A. J., Wang, Z. B., & De Ronde, J. (2012). Morphodynamic development and sediment budget of the Dutch Wadden Sea over the last century. *Netherlands Journal of Geosciences, 91*(3), 293-310.

Ellis, J. I., Clark, D., Hewitt, J. E., Taiapa, C., Sinner, J., Patterson, M., ... & McCallion, A. (2017). *Ecological survey of Tauranga harbour*. Cawthron Institute.

Ellis, J., Hewitt, J., Clark, D., Taiapa, C., Patterson, M., Sinner, J., Hardy, D., & Thrush, S. (2015). Assessing ecological community health in coastal estuarine systems impacted by multiple stressors. *Journal of Experimental Marine Biology and Ecology, 473*, 176-187.

Engelund, F., & Hansen, E. (1967). A monograph on sediment transport in alluvial streams. *Technical University of Denmark 0stervoldgade 10, Copenhagen K.*

Erftemeijer, P. L., Osinga, R., & Mars, A. E. (1993). Primary production of seagrass beds in South Sulawesi (Indonesia): a comparison of habitats, methods and species. *Aquatic Botany*, *46*(1), 67-90.

Evrard, V., Kiswara, W., Bouma, T. J., & Middelburg, J. J. (2005). Nutrient dynamics of seagrass ecosystems: 15N evidence for the importance of particulate organic matter and root systems. *Marine Ecology Progress Series*, *295*, 49-55.

Fagherazzi, S., Kirwan, M. L., Mudd, S. M., Guntenspergen, G. R., Temmerman, S., D'Alpaos, A., Van De Koppel, J., Rybczyk, J. M., Reyes, E., & Craft, C. (2012). Numerical models of salt marsh evolution: Ecological, geomorphic, and climatic factors. *Reviews of Geophysics, 50*(1).

Fairweather, P. G. (1999). Determining the 'health'of estuaries: Priorities for ecological research. *Australian Journal of Ecology, 24*(4), 441-451.

Fan, Y., Chen, S., Zhao, B., Pan, S., Jiang, C., & Ji, H. (2018). Shoreline dynamics of the active Yellow River delta since the implementation of Water-Sediment Regulation Scheme: A remote-sensing and statistics-based approach. *Estuarine, Coastal and Shelf Science, 200*, 406-419.

Ferguson, A. J., Gruber, R. K., Orr, M., & Scanes, P. (2016). Morphological plasticity in Zostera muelleri across light, sediment, and nutrient gradients in Australian temperate coastal lakes. *Marine Ecology Progress Series*, *556*, 91-104.

Filippucci, P., Brocca, L., Bonafoni, S., Saltalippi, C., Wagner, W., & Tarpanelli, A. (2022). Sentinel-2 high-resolution data for river discharge monitoring. *Remote Sensing of Environment, 281*, 113255.

Fleri, J. R., Lera, S., Gerevini, A., Staver, L., & Nardin, W. (2019). Empirical observations and numerical modelling of tides, channel morphology, and vegetative effects on accretion in a restored tidal marsh. *Earth Surface Processes and Landforms, 44*(11), 2223-2235.

Flowers, G. J., Needham, H. R., Bulmer, R. H., Lohrer, A. M., & Pilditch, C. A. (2023). The effect of sediment mud content on primary production in seagrass and unvegetated intertidal flats.

Fraser, C., White, R., Snelder, T., & Stoffels, R. (2021). New Zealand Coastal Water Quality Assessment 2021. *NIWA Client Report 2021316H*.

French, J. R. (1993). Numerical simulation of vertical marsh growth and adjustment to accelerated sea-level rise, North Norfolk, UK. *Earth Surface Processes and Landforms, 18*(1), 63-81.

Fujiki, T., & Taguchi, S. (2002). Variability in chlorophyll a specific absorption coefficient in marine phytoplankton as a function of cell size and irradiance. *Journal of Plankton Research, 24*(9), 859-874. https://doi.org/10.1093/plankt/24.9.859

Gall, M., Swales, A., Davies-Colley, R., & Bremner, D. (2019). Predicting visual clarity and light penetration from water quality measures in New Zealand estuaries. *Estuarine, Coastal and Shelf Science, 219*, 429-443.

Gallegos, C. L. (2001). Calculating optical water quality targets to restore and protect submersed aquatic vegetation: overcoming problems in partitioning the diffuse attenuation coefficient for photosynthetically active radiation. *Estuaries, 24*, 381-397.

Gallegos, D., Jafari, N. H., Ozdemir, C. E., & Boudreaux, J. (2023). EMPIRICAL MODEL OF SEDIMENT TRANSPORT AND CONSOLIDATION IN MARSH CREATION PROJECTS. In *Coastal Sediments 2023: The Proceedings of the Coastal Sediments 2023* (pp. 452-465). World Scientific.

Ganju, N. K., & Schoellhamer, D. H. (2009). Calibration of an estuarine sediment transport model to sediment fluxes as an intermediate step for simulation of geomorphic evolution. *Continental Shelf Research, 29*(1), 148-158.

Garg, V., Kumar, A. S., Aggarwal, S., Kumar, V., Dhote, P. R., Thakur, P. K., Nikam, B. R., Sambare, R. S., Siddiqui, A., & Muduli, P. R. (2017). Spectral similarity approach for mapping turbidity of an inland waterbody. *Journal of Hydrology, 550*, 527-537.

Gattuso, J.-P., Gentili, B., Duarte, C. M., Kleypas, J., Middelburg, J. J., & Antoine, D. (2006). Light availability in the coastal ocean: impact on the distribution of benthic photosynthetic organisms and their contribution to primary production. *Biogeosciences, 3*(4), 489-513.

Gege, P. (2005). The Water Colour Simulator WASI-User manual for version 3.

Geiger, E. F., Grossi, M. D., Trembanis, A. C., Kohut, J. T., & Oliver, M. J. (2013). Satellite-derived coastal ocean and estuarine salinity in the Mid-Atlantic. *Continental Shelf Research, 63*, S235-S242.

Gilvear, D., Hunter, P., & Higgins, T. (2007). An experimental approach to the measurement of the effects of water depth and substrate on optical and near infra-red reflectance: A field-based assessment of the feasibility of mapping submerged instream habitat. *International Journal of Remote Sensing, 28*(10), 2241-2256.

Goodfellow, I., Bengio, Y., & Courville, A. (2016). *Deep learning*. MIT press.

Grasso, F., Bismuth, E., & Verney, R. (2021). Unraveling the impacts of meteorological and anthropogenic changes on sediment fluxes along an estuary-sea continuum. *Scientific Reports, 11*(1), 20230.

Groom, S., Sathyendranath, S., Ban, Y., Bernard, S., Brewin, R., Brotas, V., Brockmann, C., Chauhan, P., Choi, J.-k., & Chuprin, A. (2019). Satellite ocean colour: current status and future perspective. *Frontiers in Marine Science, 6*, 485.

Grossman, E. E., Stevens, A. W., Dartnell, P., George, D., & Finlayson, D. (2020). Sediment export and impacts associated with river delta channelization compound estuary vulnerability to sea-level rise, Skagit River Delta, Washington, USA. *Marine Geology, 430*, 106336.

Grover, J. P. (1997). *Resource competition* (Vol. 19). Springer Science & Business Media.

Ha, N. T., Manley-Harris, M., Pham, T. D., & Hawes, I. (2020). A Comparative Assessment of Ensemble-Based Machine Learning and Maximum Likelihood Methods for Mapping Seagrass Using Sentinel-2 Imagery in Tauranga Harbor, New Zealand. *Remote Sensing, 12*(3), 355-371.

Ha, N. T., Manley-Harris, M., Pham, T. D., & Hawes, I. (2021). Detecting multi-decadal changes in seagrass cover in tauranga harbour, new zealand, using landsat imagery and boosting ensemble classification techniques. *ISPRS International Journal of Geo-Information*, *10*(6), 371.

Ha, N. T., Manley-Harris, M., Pham, T. D., & Hawes, I. (2021). The use of radar and optical satellite imagery combined with advanced machine learning and metaheuristic optimization techniques to detect and quantify above ground biomass of intertidal seagrass in a New Zealand estuary. *International Journal of Remote Sensing*, *42*(12), 4712-4738.

Hafeez, S. (2022). Integrating remote sensing and machine learning technologies for coastal water quality monitoring in Hong Kong and the Pearl River Estuary.

Hafizt, M., Manessa, M. D. M., Adi, N. S., & Prayudha, B. (2017, December). Benthic habitat mapping by combining lyzenga's optical model and relative water depth model in Lintea Island, Southeast Sulawesi. In *IOP Conference Series: Earth and Environmental Science* (Vol. 98, No. 1, p. 012037). IOP Publishing.

Han, W., Feng, R., Wang, L., & Cheng, Y. (2018). A semi-supervised generative framework with deep learning features for high-resolution remote sensing image scene classification. *Isprs Journal of Photogrammetry and Remote Sensing, 145*, 23-43.

Hastie, T., Tibshirani, R., Friedman, J. H., & Friedman, J. H. (2009). *The elements of statistical learning: data mining, inference, and prediction* (Vol. 2, pp. 1-758). New York: springer.

He, X., Bai, Y., Pan, D., Chen, C.-T., Cheng, Q., Wang, D., & Gong, F. (2013). Satellite views of the seasonal and interannual variability of phytoplankton blooms in the eastern China seas over the past 14 yr (1998–2011). *Biogeosciences, 10*(7), 4721-4739.

Hedley, J. D., Roelfsema, C., Brando, V., Giardino, C., Kutser, T., Phinn, S., Mumby, P. J., Barrilero, O., Laporte, J., & Koetz, B. (2018). Coral reef applications of Sentinel-2: Coverage, characteristics, bathymetry and benthic mapping with comparison to Landsat 8. *Remote Sensing of Environment, 216*, 598-614.

Heip, C. H. R., Goosen, N. K., Herman, P. M. J., Kromkamp, J., Middelburg, J. J., & Soetaert, K. (1995). Production and consumption of biological particles in temperate tidal estuaries. *Oceanography and Marine Biology: an annual review*.

Heyes, A., Miller, C., & Mason, R. P. (2004). Mercury and methylmercury in Hudson River sediment: impact of tidal resuspension on partitioning and methylation. *Marine Chemistry*, *90*(1-4), 75-89.

Hicks, D. M. Review and Analysis of Suspended Sediment Monitoring in the Tauranga Moana Catchment. (2019). *NIWA Client Report*

Review and Analysis of Suspended Sediment Monitoring in the Tauranga Moana Catchment

Hochberg, E. J., & Atkinson, M. J. (2003, May 15). Capabilities of remote sensors to classify coral, algae, and sand as pure and mixed spectra. *Remote Sensing of Environment, 85*(2), 174-189. https://doi.org/10.1016/s0034-4257(02)00202-x

Hope, J. A., Paterson, D. M., & Thrush, S. F. (2020). The role of microphytobenthos in soft-sediment ecological networks and their contribution to the delivery of multiple ecosystem services. *Journal of Ecology*, *108*(3), 815-830.

Horstman, E. M., Dohmen-Janssen, C. M., Bouma, T. J., & Hulscher, S. J. (2015). Tidal-scale flow routing and sedimentation in mangrove forests: Combining field data and numerical modelling. *Geomorphology, 228*, 244-262.

Hossain, M. S., Hashim, M., Bujang, J. S., Zakaria, M. H., & Muslim, A. M. (2019). Assessment of the impact of coastal reclamation activities on seagrass meadows in Sungai Pulai estuary, Malaysia, using Landsat data (1994–2017). *International Journal of Remote Sensing*, *40*(9), 3571-3605.

Hume, T. M., Green, M. O., & Elliott, S. (2010). Tauranga Harbour sediment study: Assessment of predictions for management: Environment Bay of Penty. atlas.boprc.govt.nz/api/v1/edms/document/A3888411/content

Isidro, C. M., McIntyre, N., Lechner, A. M., & Callow, I. (2018). Quantifying suspended solids in small rivers using satellite data. *Science of the Total Environment, 634*, 1554-1562.

Jacobs, P., Pitarch, J., Kromkamp, J. C., & Philippart, C. J. (2021). Assessing biomass and primary production of microphytobenthos in depositional coastal systems using spectral information. *Plos one*, *16*(7), e0246012.

Jagalingam, P., Akshaya, B., & Hegde, A. V. (2015). Bathymetry mapping using Landsat 8 satellite imagery. *Procedia Engineering, 116*, 560-566.

Jankowska, E., Michel, L. N., Lepoint, G., & Włodarska-Kowalczuk, M. (2019). Stabilizing effects of seagrass meadows on coastal water benthic food webs. *Journal of Experimental Marine Biology and Ecology*, *510*, 54-63.

Jensen, K., Revsbech, N. P., & Nielsen, L. P. (1993). Microscale distribution of nitrification activity in sediment determined with a shielded microsensor for nitrate. *Applied and Environmental Microbiology, 59*(10), 3287-3296.

Kamerosky, A., Cho, H. J., & Morris, L. (2015). Monitoring of the 2011 super algal bloom in Indian River Lagoon, FL, USA, using MERIS. *Remote Sensing*, *7*(2), 1441-1460.

Kanno, A., Tanaka, Y., & Sekine, M. (2013). Validation of shallow-water reflectance model for remote sensing of water depth and bottom type by radiative transfer simulation. *Journal of applied remote sensing*, *7*(1), 073516-073516.

Kettle, T. (2021). *Mātauranga Māori to inform understanding of population dynamics and health of pipi in Waihī Estuary, Bay of Plenty* The University of Waikato.

Keyzer, L., Herman, P., Smits, B., Pietrzak, J., James, R., Candy, A. S., Riva, R., Bouma, T., van der Boog, C., & Katsman, C. (2020). The potential of coastal ecosystems to mitigate the impact of sea-level rise in shallow tropical bays. *Estuarine, Coastal and Shelf Science, 246*, 107050.

Kilroy, C., Snelder, T. H., Floerl, O., Vieglais, C. C., & Dey, K. L. (2008). A rapid technique for assessing the suitability of areas for invasive species applied to New Zealand's rivers. *Diversity and Distributions, 14*(2), 262-272.

Kim, Y. H., Im, J., Ha, H. K., Choi, J.-K., & Ha, S. (2014). Machine learning approaches to coastal water quality monitoring using GOCI satellite data. *Giscience & Remote Sensing, 51*(2), 158-174.

Kirk, J. T. (1994). *Light and photosynthesis in aquatic ecosystems*. Cambridge university press.

Kirwan, M., & Temmerman, S. (2009). Coastal marsh response to historical and future sea-level acceleration. *Quaternary Science Reviews, 28*(17-18), 1801-1808.

Kirwan, M. L., Temmerman, S., Skeehan, E. E., Guntenspergen, G. R., & Fagherazzi, S. (2016). Overestimation of marsh vulnerability to sea level rise. *Nature climate change, 6*(3), 253-260.

Kohler, K. E., & Gill, S. M. (2006). Coral Point Count with Excel extensions (CPCe): A Visual Basic program for the determination of coral and substrate coverage using random point count methodology. *Computers & geosciences*, *32*(9), 1259-1269.

Krauss, K. W., Allen, J., & Cahoon, D. R. (2003). Differential rates of vertical accretion and elevation change among aerial root types in Micronesian mangrove forests. *Estuarine, Coastal and Shelf Science, 56*(2), 251-259.

Krauss, K. W., McKee, K. L., Lovelock, C. E., Cahoon, D. R., Saintilan, N., Reef, R., & Chen, L. (2014). How mangrove forests adjust to rising sea level. *New Phytologist, 202*(1), 19-34.

Krone, R. B. (1987). A Method for Simulating Historic Marsh Elevations.

Kuhn, C., de Matos Valerio, A., Ward, N., Loken, L., Sawakuchi, H. O., Kampel, M., Richey, J., Stadler, P., Crawford, J., & Striegl, R. (2019). Performance of Landsat-8 and Sentinel-2 surface reflectance products for river remote sensing retrievals of chlorophyll-a and turbidity. *Remote Sensing of Environment, 224*, 104-118.

Lee, K. S., Park, S. R., & Kim, Y. K. (2007). Effects of irradiance, temperature, and nutrients on growth dynamics of seagrasses: a review. *Journal of Experimental Marine Biology and Ecology*, *350*(1-2), 144-175.

Lee, S. Y., Primavera, J. H., Dahdouh-Guebas, F., McKee, K., Bosire, J. O., Cannicci, S., Diele, K., Fromard, F., Koedam, N., & Marchand, C. (2014). Ecological role and services of tropical mangrove ecosystems: a reassessment. *Global ecology and biogeography, 23*(7), 726-743.

Lee, Z. P., Du, K. P., & Arnone, R. (2005). A model for the diffuse attenuation coefficient of downwelling irradiance. *Journal of Geophysical Research: Oceans, 110*(C2).

Legge, O., Johnson, M., Hicks, N., Jickells, T., Diesing, M., Aldridge, J., ... & Williamson, P. (2020). Carbon on the northwest European shelf: Contemporary budget and future influences. *Frontiers in Marine Science*, *7*, 143.

Lehmann, M., Nguyen, U., Allan, M., & van der Woerd, H. (2018). Colour Classification of 1486 Lakes across a Wide Range of Optical Water Types. *Remote Sensing, 10*(8), 1273-1295. https://doi.org/10.3390/rs10081273

Leonard, L. A., & Croft, A. L. (2006). The effect of standing biomass on flow velocity and turbulence in Spartina alterniflora canopies. *Estuarine, Coastal and Shelf Science, 69*(3-4), 325-336.

Lesser, G. R., Roelvink, J. v., van Kester, J. T. M., & Stelling, G. (2004). Development and validation of a three-dimensional morphological model. *Coastal engineering, 51*(8-9), 883-915.

Li, M., Lundquist, C. J., Pilditch, C. A., Rees, T., & Ellis, J. (2019). Implications of nutrient enrichment for the conservation and management of seagrass Zostera muelleri meadows. *Aquatic Conservation: Marine and Freshwater Ecosystems, 29*(9), 1484-1502.

Li, M., Sun, Y., Li, X., Cui, M., & Huang, C. (2021). An improved eutrophication assessment algorithm of estuaries and coastal waters in Liaodong Bay. *Remote Sensing, 13*(19), 3867.

Li, P., Ke, Y., Bai, J., Zhang, S., Chen, M., & Zhou, D. (2019). Spatiotemporal dynamics of suspended particulate matter in the Yellow River Estuary, China during the past two decades based on time-series Landsat and Sentinel-2 data. *Marine Pollution Bulletin, 149*, 110518.

Liaw, A., & Wiener, M. (2002). Classification and regression by randomForest. *R news, 2*(3), 18-22.

Lin, H., Yu, Q., Wang, Y., & Gao, S. (2022). Identification, extraction and interpretation of multi-period variations of coastal suspended sediment concentration based on unevenly spaced observations. *Marine Geology, 445*, 106732.

Liu, H., Li, Q., Shi, T., Hu, S., Wu, G., & Zhou, Q. (2017). Application of Sentinel 2 MSI Images to Retrieve Suspended Particulate Matter Concentrations in Poyang Lake. *Remote Sensing, 9*(7).

Liu, T., Jin, H., Li, A., Fang, H., Wei, D., Xie, X., & Nan, X. (2022). Estimation of Vegetation Leaf-Area-Index Dynamics from Multiple Satellite Products through Deep-Learning Method. *Remote Sensing*, *14*(19), 4733.

Livingston, R. J., McGlynn, S. E., & Niu, X. (1998). Factors controlling seagrass growth in a gulf coastal system: Water and sediment quality and light. *Aquatic Botany, 60*(2), 135-159.

Lodhi, M. A., & Rundquist, D. C. (2010). A spectral analysis of bottom-induced variation in the colour of Sand Hills lakes, Nebraska, USA. *International Journal of Remote Sensing, 22*(9), 1665-1682. https://doi.org/10.1080/01431160117495

Lunetta, R. S., Knight, J. F., Paerl, H. W., Streicher, J. J., Peierls, B. L., Gallo, T., ... & Buzzelli, C. P. (2009). Measurement of water colour using AVIRIS imagery to assess the potential for an operational monitoring capability in the Pamlico Sound Estuary, USA. *International Journal of Remote Sensing*, *30*(13), 3291-3314.

Lund-Hansen, L. C. (2004). Diffuse attenuation coefficients Kd (PAR) at the estuarine North Sea–Baltic Sea transition: time-series, partitioning, absorption, and scattering. *Estuarine, Coastal and Shelf Science*, *61*(2), 251-259.

Luo, X., Qin, X., Wu, Z., Yang, F., Wang, M., & Shang, J. (2019). Sediment classification of small-size seabed acoustic images using convolutional neural networks. *IEEE access, 7*, 98331-98339.

Lyzenga, D. R. (1981). Remote sensing of bottom reflectance and water attenuation parameters in shallow water using aircraft and Landsat data. *International Journal of Remote Sensing, 2*(1), 71-82. https://doi.org/10.1080/01431168108948342

Ma, Y., Zhang, H., Li, X., Wang, J., Cao, W., Li, D., Lou, X., & Fan, K. (2021). An exponential algorithm for bottom reflectance retrieval in clear optically shallow waters from multispectral imagery without ground data. *Remote Sensing, 13*(6), 1169.

Maciel, F., & Pedocchi, F. (2022). Evaluation of ACOLITE atmospheric correction methods for Landsat-8 and Sentinel-2 in the Río de la Plata turbid coastal waters. *International Journal of Remote Sensing, 43*(1), 215-240.

Mangan, S., Bryan, K., Thrush, S., Gladstone-Gallagher, R., Lohrer, A., & Pilditch, C. (2020). Shady business: the darkening of estuaries constrains benthic ecosystem function. *Marine Ecology Progress Series, 647*, 33-48.

Mangan, S., Lohrer, A. M., Thrush, S. F., & Pilditch, C. A. (2020). Water column turbidity not sediment nutrient enrichment moderates microphytobenthic primary production. *Journal of Marine Science and Engineering, 8*(10), 732. https://doi.org/10.3390/jmse8100732

Manning, A., & Dyer, K. (2007). Mass settling flux of fine sediments in Northern European estuaries: measurements and predictions. *Marine Geology, 245*(1-4), 107-122.

Mannino, A., Russ, M. E., & Hooker, S. B. (2008). Algorithm development and validation for satellite-derived distributions of DOC and CDOM in the US Middle Atlantic Bight. *Journal of Geophysical Research: Oceans, 113*(C7).

Maritorena, S., Morel, A., & Gentili, B. (1994). Diffuse reflectance of oceanic shallow waters: Influence of water depth and bottom albedo. *Limnology and oceanography*, *39*(7), 1689-1703.

Markert, K. N., Schmidt, C. M., Griffin, R. E., Flores, A. I., Poortinga, A., Saah, D. S., Muench, R. E., Clinton, N. E., Chishtie, F., & Kityuttachai, K. (2018). Historical and operational monitoring of surface sediments in the lower mekong basin using landsat and google earth engine cloud computing. *Remote Sensing, 10*(6), 909.

Martin, J., Mouchel, J., & Nirel, P. (1986). Some recent developments in the characterization of estuarine particulates. *Water science and technology, 18*(4-5), 83-92.

Martins, V., Barbosa, C., de Carvalho, L., Jorge, D., Lobo, F., & Novo, E. (2017). Assessment of Atmospheric Correction Methods for Sentinel-2 MSI Images Applied to Amazon Floodplain Lakes. *Remote Sensing, 9*(4). https://doi.org/10.3390/rs9040322

Mastrocicco, M., Busico, G., Colombani, N., Vigliotti, M., & Ruberti, D. (2019). Modelling actual and future seawater intrusion in the Variconi coastal wetland (Italy) due to climate and landscape changes. *Water, 11*(7), 1502.

Matheson, F. E., & Schwarz, A. M. (2007). Growth responses of Zostera capricorni to estuarine sediment conditions. *Aquatic Botany*, *87*(4), 299-306.

Mazda, Y., Magi, M., Nanao, H., Kogo, M., Miyagi, T., Kanazawa, N., & Kobashi, D. (2002). Coastal erosion due to long-term human impact on mangrove forests. *Wetlands Ecology and Management, 10*, 1-9.

McFeeters, S. K. (1996). The use of the Normalized Difference Water Index (NDWI) in the delineation of open water features. *International journal of remote sensing*, *17*(7), 1425-1432.

McFeeters, S. (2013). Using the Normalized Difference Water Index (NDWI) within a Geographic Information System to Detect Swimming Pools for Mosquito Abatement: A Practical Approach. *Remote Sensing, 5*(7), 3544-3561. https://doi.org/10.3390/rs5073544

McKinna, L. I., & Werdell, P. J. (2018). Approach for identifying optically shallow pixels when processing ocean-color imagery. *Optics express*, *26*(22), A915-A928.

Méléder, V., Savelli, R., Barnett, A., Polsenaere, P., Gernez, P., Cugier, P., ... & Lavaud, J. (2020). Mapping the intertidal microphytobenthos gross primary production part I: coupling multispectral remote sensing and physical modeling. *Frontiers in Marine Science*, *7*, 520.

Migné, A., Spilmont, N., & Davoult, D. (2004). In situ measurements of benthic primary production during emersion: seasonal variations and annual production in the Bay of Somme (eastern English Channel, France). *Continental Shelf Research*, *24*(13-14), 1437-1449.

Miles, A., & Sundbäck, K. (2000). Diel variation in microphytobenthic productivity in areas of different tidal amplitude. *Marine Ecology Progress Series*, *205*, 11-22.

Miller, G. C., & Zepp, R. G. (1979). Effects of suspended sediments on photolysis rates of dissolved pollutants. *Water Research, 13*(5), 453-459.

Mishra, S., & Mishra, D. R. (2012). Normalized difference chlorophyll index: A novel model for remote estimation of chlorophyll-a concentration in turbid productive waters. *Remote Sensing of Environment, 117*, 394-406.

Mitchell, B. G., & Holm-Hansen, O. (1991). Bio-optical properties of Antarctic Peninsula waters: Differentiation from temperate ocean models. *Deep Sea Research Part A. Oceanographic Research Papers, 38*(8-9), 1009-1028.

Mobley, C. D., & Sundman, L. K. (2008). Hydrolight 5 Ecolight 5. *Sequoia Scientific Inc*.

Morelle, J., Claquin, P., & Orvain, F. (2020). Evidence for better microphytobenthos dynamics in mixed sand/mud zones than in pure sand or mud intertidal flats (Seine estuary, Normandy, France). *PloS one*, *15*(8), e0237211.

Moriarty, D. J. W., Boon, P. I., Hansen, J. A., Hunt, W. G., Poiner, I. R., Pollard, P. C., ... & White, D. C. (1985). Microbial biomass and productivity in seagrass beds. *Geomicrobiology Journal*, *4*(1), 21-51.

Morris, J. T., Sundareshwar, P., Nietch, C. T., Kjerfve, B., & Cahoon, D. R. (2002). Responses of coastal wetlands to rising sea level. *Ecology, 83*(10), 2869-2877.

Morrison, M., Lowe, M. L., Grant, C. M., Smith, P. J., Carbines, G. D., Reed, J., ... & Brown, J. C. (2014). Seagrass meadows as biodiversity and productivity hotspots.

Mouw, C. B., Greb, S., Aurin, D., DiGiacomo, P. M., Lee, Z., Twardowski, M., Binding, C., Hu, C., Ma, R., Moore, T., Moses, W., & Craig, S. E. (2015, Apr). Aquatic color radiometry remote sensing of coastal and inland waters: Challenges and recommendations for future satellite missions. *Remote Sensing of Environment, 160*, 15-30. https://doi.org/10.1016/j.rse.2015.02.001

Mountrakis, G., Im, J., & Ogole, C. (2011). Support vector machines in remote sensing: A review. *ISPRS journal of photogrammetry and remote sensing*, *66*(3), 247-259.

Mueller, J. L. (2000). SeaWiFS algorithm for the diffuse attenuation coefficient, K (490), using water-leaving radiances at 490 and 555 nm. *SeaWiFS postlaunch calibration and validation analyses, part, 3*(11), 24-27.

Nazemi Ashani, Z., Zainuddin, M. F., Che Ilias, I. S., & Ng, K. Y. (2023). A Combined Computer Vision and Convolution Neural Network Approach to Classify Turbid Water Samples in Accordance with National Water Quality Standards. *Arabian Journal for Science and Engineering*, 1-14.

Neverman, A. J., Donovan, M., Smith, H. G., Ausseil, A.-G., & Zammit, C. (2023). Climate change impacts on erosion and suspended sediment loads in New Zealand. *Geomorphology, 427*, 108607.

Nguyen, H. M., Bryan, K. R., Pilditch, C. A., & Moon, V. G. (2019). Influence of ambient temperature on erosion properties of exposed cohesive sediment from an intertidal mudflat. *Geo-Marine Letters, 39*, 337-347.

O'Brien, D. S., Chiswell, B., & Mueller, J. F. (2009, 2009). A novel method for the in situ calibration of flow effects on a phosphate passive sampler. *Journal of Environmental Monitoring, 11*(1), 212-219. https://doi.org/10.1039/b809901d

O'Reilly, J. E. (2000). *SeaWiFS postlaunch calibration and validation analyses, part 3*. NASA Center for AeroSpace Information.

O'Brien, A., Townsend, K., Hale, R., Sharley, D., & Pettigrove, V. (2016). How is ecosystem health defined and measured? A critical review of freshwater and estuarine studies. *Ecological Indicators, 69*, 722-729.

Ogashawara, I., Mishra, D. R., & Gitelson, A. A. (2017). Remote sensing of inland waters: background and current state-of-the-art. In *Bio-optical modeling and remote sensing of inland waters* (pp. 1-24). Elsevier.

Ogston, A. S., & Field, M. E. (2010). Predictions of turbidity due to enhanced sediment resuspension resulting from sea-level rise on a fringing coral reef: evidence from Molokai, Hawaii. *Journal of Coastal Research*, *26*(6), 1027-1037.

Oppenheimer, M., Glavovic, B., Hinkel, J., Van de Wal, R., Magnan, A. K., Abd-Elgawad, A., ... & Sebesvari, Z. (2019). Sea level rise and implications for low lying islands, coasts and communities.

Orth, R. J., Carruthers, T. J., Dennison, W. C., Duarte, C. M., Fourqurean, J. W., Heck, K. L., ... & Williams, S. L. (2006). A global crisis for seagrass ecosystems. *Bioscience*, *56*(12), 987-996.

Owens, P. N., Batalla, R., Collins, A., Gomez, B., Hicks, D., Horowitz, A., Kondolf, G., Marden, M., Page, M., & Peacock, D. (2005). Fine-grained sediment in river systems: environmental significance and management issues. *River Research and Applications, 21*(7), 693-717.

Palandro, D., Hu, C., Andréfouët, S., & Muller-Karger, F. E. (2004). Synoptic water clarity assessment in the Florida Keys using diffuse attenuation coefficient estimated from Landsat imagery. In *Coelenterate Biology 2003: Trends in Research on Cnidaria and Ctenophora* (pp. 489-493). Springer Netherlands.

Parshotam, A., Wadhwa, S., & Mullan, B. (2009). *Tauranga harbour sediment study: sediment load model implementation and validation*. NIWA.

Papenmeier, S. (2012). *Properties and dynamics of suspended load and near-bed fine cohesive sediments in highly impacted estuaries. Case studies from the Weser, Ems and Elbe estuaries (Germany)* Univierstiy of Kiel.

Park, S. (1991). Coastal and Overview Report. *Bay of Plenty Regional Council Technical publication Number 3, August 1991*.

Park, S. (2005). Environmental Quality of Ohiwa Harbour - 2005. *Bay of Plenty Regional Council Technical Publication*.

Park, S. (2020). Seagrass health monitoring in Tauranga Harbor. *Bay of Plenty Regional Council Environmental Publication*, *8*.

Partheniades, E. (1962). *A study of erosion and deposition of cohesive soils in salt water*. University of California, Berkeley.

Patel, B. (2011). *The response of juvenile snapper, Pagrus auratus, to environmental hypoxia and oxygen profiles in the Mahurangi estuary, Auckland region* ResearchSpace@ Auckland].

Pavlov, A. K., Granskog, M. A., Stedmon, C. A., Ivanov, B. V., Hudson, S. R., & Falk-Petersen, S. (2015). Contrasting optical properties of surface waters across the Fram Strait and its potential biological implications. *Journal of Marine Systems, 143*, 62-72.

Petus, C., da Silva, E. T., Devlin, M., Wenger, A. S., & Álvarez-Romero, J. G. (2014). Using MODIS data for mapping of water types within river plumes in the Great Barrier Reef, Australia: Towards the production of river plume risk maps for reef and seagrass ecosystems. *Journal of Environmental Management, 137*, 163-177.

Pham, T. D., Yoshino, K., Le, N. N., & Bui, D. T. (2018). Estimating aboveground biomass of a mangrove plantation on the Northern coast of Vietnam using machine learning techniques with an integration of ALOS-2 PALSAR-2 and Sentinel-2A data. *International Journal of Remote Sensing*, *39*(22), 7761-7788.

Phillips, D., Black, K., & Healy, T. (2001). Seabed characteristics of a dynamic exposed headland. Australasian Port and Harbour Conference (8th: 2001: Gold Coast, Qld.),

Pinckney, J. L., & Zingmark, R. G. (1993). Modeling the annual production of intertidal benthic microalgae in estuarine ecosystems 1. *Journal of Phycology, 29*(4), 396-407.

Pitarch, J., Bellacicco, M., Marullo, S., & Van Der Woerd, H. J. (2021). Global maps of Forel–Ule index, hue angle and Secchi disk depth derived from 21 years of monthly ESA Ocean Colour Climate Change Initiative data. *Earth System Science Data*, *13*(2), 481-490.

Post, D. L. (1997). Color and human-computer interaction. In *Handbook of human-computer interaction* (pp. 573-615). Elsevier.

Pratt, D. R., Pilditch, C. A., Lohrer, A. M., & Thrush, S. F. (2014). The effects of short-term increases in turbidity on sandflat microphytobenthic productivity and nutrient fluxes. *Journal of sea research*, *92*, 170-177.

Pu, R., Bell, S., & Meyer, C. (2014). Mapping and assessing seagrass bed changes in Central Florida's west coast using multitemporal Landsat TM imagery. *Estuarine, Coastal and Shelf Science*, *149*, 68-79.

Raposa, K. B., Wasson, K., Smith, E., Crooks, J. A., Delgado, P., Fernald, S. H., Ferner, M. C., Helms, A., Hice, L. A., & Mora, J. W. (2016). Assessing tidal marsh resilience to sea-level rise at broad geographic scales with multi-metric indices. *Biological Conservation, 204*, 263-275.

Ray, S. (2019). A quick review of machine learning algorithms. 2019 International conference on machine learning, big data, cloud and parallel computing (COMITCon),

Reed, D. J., Spencer, T., Murray, A. L., French, J. R., & Leonard, L. (1999). Marsh surface sediment deposition and the role of tidal creeks: implications for created and managed coastal marshes. *Journal of Coastal Conservation, 5*, 81-90.

Reidenbach, M. A., & Timmerman, R. (2019). Interactive effects of seagrass and the microphytobenthos on sediment suspension within shallow coastal bays. *Estuaries and Coasts*, *42*(8), 2038-2053.

Repolho, T., Duarte, B., Dionísio, G., Paula, J. R., Lopes, A. R., Rosa, I. C., ... & Rosa, R. (2017). Seagrass ecophysiological performance under ocean warming and acidification. *Scientific Reports*, *7*(1), 41443.

Robins, P. E., Skov, M. W., Lewis, M. J., Giménez, L., Davies, A. G., Malham, S. K., Neill, S. P., McDonald, J. E., Whitton, T. A., & Jackson, S. E. (2016). Impact of climate change on UK estuaries: A review of past trends and potential projections. *Estuarine, Coastal and Shelf Science, 169*, 119-135.

Rocha, A. D., Groen, T. A., Skidmore, A. K., Darvishzadeh, R., & Willemen, L. (2017). The Naïve Overfitting Index Selection (NOIS): A new method to optimize model complexity for hyperspectral data. *Isprs Journal of Photogrammetry and Remote Sensing, 133*, 61-74.

Rodil, I. F., Attard, K. M., Norkko, J., Glud, R. N., & Norkko, A. (2019). Towards a sampling design for characterizing habitat-specific benthic biodiversity related to oxygen flux dynamics using Aquatic Eddy Covariance. *PLoS One*, *14*(2), e0211673.

Rodriguez, A. R., & Heck, K. L. (2021). Approaching a Tipping Point? Herbivore Carrying Capacity Estimates in a Rapidly Changing, Seagrass-Dominated Florida Bay. *Estuaries and Coasts, 44*(2), 522-534. https://doi.org/10.1007/s12237-020-00866-2

Roelvink, J., & Van Banning, G. (1995). Design and development of DELFT3D and application to coastal morphodynamics. *Oceanographic Literature Review, 11*(42), 925.

Roskoden, R. R., Bryan, K. R., Schreiber, I., & Kopf, A. (2020). Rapid transition of sediment consolidation across an expanding mangrove fringe in the Firth of Thames New Zealand. *Geo-Marine Letters, 40*, 295-308.

Rullens, V., Mangan, S., Stephenson, F., Clark, D. E., Bulmer, R. H., Berthelsen, A., ... & Pilditch, C. A. (2022). Understanding the consequences of sea level rise: the

ecological implications of losing intertidal habitat. *New Zealand Journal of Marine and Freshwater Research*, *56*(3), 353-370.

Rullens, V., Stephenson, F., Lohrer, A. M., Townsend, M., & Pilditch, C. A. (2021). Combined species occurrence and density predictions to improve marine spatial management. *Ocean & Coastal Management*, *209*, 105697.

Sadeghi, M., Babaeian, E., Tuller, M., & Jones, S. B. (2018). Particle size effects on soil reflectance explained by an analytical radiative transfer model. *Remote Sensing of Environment*, *210*, 375-386.

Sagawa, T., Boisnier, E., Komatsu, T., Mustapha, K. B., Hattour, A., Kosaka, N., & Miyazaki, S. (2010). Using bottom surface reflectance to map coastal marine areas: a new application method for Lyzenga's model. *International Journal of Remote Sensing, 31*(12), 3051-3064.

Sagawa, T., Mikami, A., Komatsu, T., Kosaka, N., Kosako, A., Miyazaki, S., & Takahashi, M. (2008). Mapping seagrass beds using IKONOS satellite image and side scan sonar measurements: a Japanese case study. *International Journal of Remote Sensing*, *29*(1), 281-291.

Sagawa, T., Yamashita, Y., Okumura, T., & Yamanokuchi, T. (2019). Satellite derived bathymetry using machine learning and multi-temporal satellite images. *Remote Sensing, 11*(10), 1155.

Salleh, S., & McMinn, A. (2021). Tolerance of tropical marine microphytobenthos exposed to elevated irradiance and temperature. *Biogeosciences, 18*(19), 5313-5326.

Scarpetta, M., Affuso, P., De Virgilio, M., Spadavecchia, M., Andria, G., & Giaquinto, N. (2022, May). Monitoring of Seagrass Meadows Using Satellite Images and U-Net Convolutional Neural Network. In *2022 IEEE International Instrumentation and Measurement Technology Conference (I2MTC)* (pp. 1-6). IEEE.

Schaeffer, B. A., Iiames, J., Dwyer, J., Urquhart, E., Salls, W., Rover, J., & Seegers, B. (2018). An initial validation of Landsat 5 and 7 derived surface water temperature for US lakes, reservoirs, and estuaries. *International Journal of Remote Sensing, 39*(22), 7789-7805.

Schile, L. M., Callaway, J. C., Morris, J. T., Stralberg, D., Parker, V. T., & Kelly, M. (2014). Modeling tidal marsh distribution with sea-level rise: evaluating the role of vegetation, sediment, and upland habitat in marsh resiliency. *PLoS One, 9*(2), e88760.

Scholes, P. (2015). *NERMN estuary water quality report 2014*. Bay of Plenty Regional Council.

Sekertekin, A. (2021). A survey on global thresholding methods for mapping open water body using Sentinel-2 satellite imagery and normalized difference water index. *Archives of Computational Methods in Engineering, 28*, 1335-1347.

Shao, Z., Bryan, K. R., Lehmann, M. K., Flowers, G. J., & Pilditch, C. A. (2024). Scaling up benthic primary productivity estimates in a large intertidal estuary using remote sensing. *Science of the Total Environment, 906*, 167389.

Shao, Z., Bryan, K. R., Lehmann, M. K., & Pilditch, C. A. (2023). Extracting remotely sensed water quality parameters from shallow intertidal estuaries. *Remote Sensing, 15*(1), 11.

Shchepetkin, A. F., & McWilliams, J. C. (2005). The regional oceanic modeling system (ROMS): a split-explicit, free-surface, topography-following-coordinate oceanic model. *Ocean Modelling, 9*(4), 347-404.

Sheahan, D., Maud, J., Wither, A., Moffat, C., & Engelke, C. (2013). Impacts of climate change on pollution (estuarine and coastal). *MCCIP Science Review, 4*, 244-251.

Sherwood, C. R., Aretxabaleta, A. L., Harris, C. K., Rinehimer, J. P., Verney, R., & Ferré, B. (2018). Cohesive and mixed sediment in the regional ocean modeling system (ROMS v3. 6) implemented in the Coupled Ocean–Atmosphere–Wave–Sediment Transport Modeling System (COAWST r1234). *Geoscientific Model Development, 11*(5), 1849-1871.

Shin, J. Y., Artigas, F., Hobble, C., & Lee, Y.-S. (2013). Assessment of anthropogenic influences on surface water quality in urban estuary, northern New Jersey: multivariate approach. *Environmental monitoring and assessment, 185*, 2777-2794.

Short, F. T., & Neckles, H. A. (1999). The effects of global climate change on seagrasses. *Aquatic Botany*, *63*(3-4), 169-196.

Sinaga, K. P., & Yang, M.-S. (2020). Unsupervised K-means clustering algorithm. *IEEE access, 8*, 80716-80727.

Sokol, Z., Szturc, J., Orellana-Alvear, J., Popova, J., Jurczyk, A., & Célleri, R. (2021). The role of weather radar in rainfall estimation and its application in meteorological and hydrological modelling—A review. *Remote Sensing, 13*(3), 351.

Sokoletsky, L. G., Budak, V. P., Shen, F., & Kokhanovsky, A. A. (2014). Comparative analysis of radiative transfer approaches for calculation of plane transmittance and diffuse attenuation coefficient of plane-parallel light scattering layers. *Applied optics, 53*(3), 459-468.

Spörli, K., & Harrison, R. E. (2004). Northland Allochthon infolded into basement, Whangarei area, northern New Zealand. *New Zealand Journal of Geology and Geophysics, 47*(3), 391-398.

Staehr, P. A., Testa, J. M., Kemp, W. M., Cole, J. J., Sand-Jensen, K., & Smith, S. V. (2012). The metabolism of aquatic ecosystems: history, applications, and future challenges. *Aquatic Sciences*, *74*, 15-29.

Statham, P. J. (2012). Nutrients in estuaries—An overview and the potential impacts of climate change. *Science of the total environment*, *434*, 213-227.

Steinberg, D., & Colla, P. (2009). CART: classification and regression trees. *The top ten algorithms in data mining, 9*, 179.

Stewart, B. T. (2021). *Investigating groundwater derived nutrient fluxes within Tauranga harbour, New Zealand* The University of Waikato.

Stone, M., Krishnappan, B., Granger, S., Upadhayay, H., Zhang, Y., Chivers, C., Decent, Q., & Collins, A. (2021). Deposition and erosion behaviour of cohesive sediments in the upper River Taw observatory, southwest UK: Implications for management and modelling. *Journal of Hydrology, 598*, 126145.

Storlazzi, C., Elias, E., Field, M., & Presto, M. (2011). Numerical modeling of the impact of sea-level rise on fringing coral reef hydrodynamics and sediment transport. *Coral Reefs, 30*(Suppl 1), 83-96.

Stralberg, D., Brennan, M., Callaway, J. C., Wood, J. K., Schile, L. M., Jongsomjit, D., Kelly, M., Parker, V. T., & Crooks, S. (2011). Evaluating tidal marsh sustainability in the face of sea-level rise: a hybrid modeling approach applied to San Francisco Bay. *PLoS One, 6*(11), e27388.

Stumpf, R. P., Holderied, K., & Sinclair, M. (2003, Jan). Determination of water depth with high-resolution satellite imagery over variable bottom types. *Limnology and Oceanography, 48*(1), 547-556.

Sundbäck, K., & Miles, A. (2002). Role of microphytobenthos and denitrification for nutrient turnover in embayments with floating macroalgal mats: a spring situation. *Aquatic Microbial Ecology*, *30*(1), 91-101.

Swanson, K. M., Drexler, J. Z., Schoellhamer, D. H., Thorne, K. M., Casazza, M. L., Overton, C. T., Callaway, J. C., & Takekawa, J. Y. (2014). Wetland accretion rate model of ecosystem resilience (WARMER) and its application to habitat sustainability for endangered species in the San Francisco estuary. *Estuaries and Coasts, 37*, 476-492.

Syvitski, J. P., Vörösmarty, C. J., Kettner, A. J., & Green, P. (2005). Impact of humans on the flux of terrestrial sediment to the global coastal ocean. *science, 308*(5720), 376-380.

Tay, H. W., Bryan, K. R., Pilditch, C. A., Park, S., & Hamilton, D. P. (2011). Variations in nutrient concentrations at different time scales in two shallow tidally dominated estuaries. *Marine and Freshwater Research*, *63*(2), 95-109.

Tallam, K., & White Jr, E. (2023). The role of diseases in unifying the health of global estuaries. *Frontiers in Marine Science, 10*, 1185662.

Talukdar, S., Singha, P., Mahato, S., Pal, S., Liou, Y.-A., & Rahman, A. (2020). Land-use land-cover classification by machine learning classifiers for satellite observations—A review. *Remote Sensing, 12*(7), 1135.

Temmerman, S., Bouma, T. J., Govers, G., Wang, Z. B., De Vries, M., & Herman, P. (2005). Impact of vegetation on flow routing and sedimentation patterns: Three-dimensional modeling for a tidal marsh. *Journal of Geophysical Research: Earth Surface, 110*(F4).

Temmerman, S., Govers, G., Meire, P., & Wartel, S. (2003). Modelling long-term tidal marsh growth under changing tidal conditions and suspended sediment concentrations, Scheldt estuary, Belgium. *Marine Geology, 193*(1-2), 151-169.

Temmerman, S., Govers, G., Wartel, S., & Meire, P. (2004). Modelling estuarine variations in tidal marsh sedimentation: response to changing sea level and suspended sediment concentrations. *Marine Geology, 212*(1-4), 1-19.

Thalib, M. S., Nurdin, N., & Aris, A. (2018, June). The ability of lyzenga's algorithm for seagrass mapping using sentinel-2a imagery on Small Island, Spermonde Archipelago, Indonesia. In *IOP Conference Series: Earth and Environmental Science* (Vol. 165, No. 1, p. 012028). IOP Publishing.

Thomas, S., & Ridd, P. V. (2004). Review of methods to measure short time scale sediment accumulation. *Marine Geology, 207*(1-4), 95-114.

Thorhaug, A., Richardson, A. D., & Berlyn, G. P. (2007). Spectral reflectance of the seagrasses: Thalassia testudinum, Halodule wrightii, Syringodium filiforme and five marine algae. *International Journal of Remote Sensing*, *28*(7), 1487-1501.

Thrush, S. F., Hewitt, J. E., Cummings, V. J., Ellis, J., Hatton, C., Lohrer, A., & Norkko, A. (2004). Muddy waters: elevating sediment input to coastal and estuarine habitats. *Frontiers in Ecology and the Environment, 2*(6), 299-306.

Thrush, S. F., Hewitt, J. E., Gladstone-Gallagher, R. V., Savage, C., Lundquist, C., O'Meara, T., ... & Pilditch, C. (2021). Cumulative stressors reduce the self-regulating capacity of coastal ecosystems. *Ecological Applications, 31*(1), e02223.

Thrush, S. F., Hewitt, J. E., & Lohrer, A. M. (2012). Interaction networks in coastal soft-sediments highlight the potential for change in ecological resilience. *Ecological applications*, *22*(4), 1213-1223.

Traganos, D., & Reinartz, P. (2018). Interannual change detection of Mediterranean seagrasses using RapidEye image time series. *Frontiers in plant science*, *9*, 96.

Traganos, D., & Reinartz, P. (2018). Mapping Mediterranean seagrasses with Sentinel-2 imagery. *Marine pollution bulletin*, *134*, 197-209.

Umgiesser, G., Canu, D. M., Cucco, A., & Solidoro, C. (2004). A finite element model for the Venice Lagoon. Development, set up, calibration and validation. *Journal of Marine Systems, 51*(1-4), 123-145.

Vahtmäe, E., Kotta, J., Argus, L., Kotta, M., Kotta, I., & Kutser, T. (2021). A Model-Based Assessment of Canopy-Scale Primary Productivity for the Baltic Sea Benthic Vegetation Using Environmental Variables and Spectral Indices. *Remote Sensing*, *14*(1), 158.

Van der Wal, D. P. M. J. H. D., Herman, P. M. J., Forster, R. M., Ysebaert, T., Rossi, F., Knaeps, E., ... & Ides, S. J. (2008). Distribution and dynamics of intertidal

macrobenthos predicted from remote sensing: response to microphytobenthos and environment. *Marine Ecology Progress Series*, *367*, 57-72.

Van Vuuren, D. P., Edmonds, J., Kainuma, M., Riahi, K., Thomson, A., Hibbard, K., ... & Rose, S. K. (2011). The representative concentration pathways: an overview. *Climatic change*, *109*, 5-31.

Vapnik, V., Golowich, S., & Smola, A. (1996). Support vector method for function approximation, regression estimation and signal processing. *Advances in neural information processing systems, 9*.

Vette, J. I. (1991). *The NASA/National Space Science Data Center: Trapped Radiation Environment Model Program (1964-1991)* (Vol. 91). National Space Science Data Center (NSSDC), World Data Center A for Rockets.

Verpoorter, C., Carrère, V., & Combe, J. P. (2014). Visible, near-infrared spectrometry for simultaneous assessment of geophysical sediment properties (water and grain size) using the Spectral Derivative–Modified Gaussian Model. *Journal of Geophysical Research: Earth Surface*, *119*(10), 2098-2122.

Vient, J.M., Fablet, R., Jourdin, F., & Delacourt, C. (2022). End-to-End Neural Interpolation of Satellite-Derived Sea Surface Suspended Sediment Concentrations. *Remote Sensing, 14*(16), 4024.

Vos, R., Hakvoort, J., Jordans, R., & Ibelings, B. (2003). Multiplatform optical monitoring of eutrophication in temporally and spatially variable lakes. *Science of the Total Environment, 312*(1-3), 221-243.

Walling, D. (2006). Human impact on land–ocean sediment transfer by the world's rivers. *Geomorphology, 79*(3-4), 192-216.

Wang, C., Li, W., Chen, S., Li, D., Wang, D., & Liu, J. (2018). The spatial and temporal variation of total suspended solid concentration in Pearl River Estuary during 1987–2015 based on remote sensing. *Science of the Total Environment, 618*, 1125-1138.

Wang, Y., He, X., Bai, Y., Li, T., Wang, D., Zhu, Q., & Gong, F. (2022). Satellite-Derived Bottom Depth for Optically Shallow Waters Based on Hydrolight Simulations. *Remote Sensing, 14*(18), 4590.

Ward, P. J., van Balen, R. T., Verstraeten, G., Renssen, H., & Vandenberghe, J. (2009). The impact of land use and climate change on late Holocene and future suspended sediment yield of the Meuse catchment. *Geomorphology*, *103*(3), 389-400.

Webb, W. L., Newton, M., & Starr, D. (1974). Carbon dioxide exchange of Alnus rubra: a mathematical model. *Oecologia*, *17*, 281-291.

Wernand, M., & Van der Woerd, H. (2010). Spectral analysis of the Forel-Ule Ocean colour comparator scale. *Journal of the European Optical Society-Rapid Publications, 5*.

Wernand, M. R. (2010). On the history of the Secchi disc. *Journal of the European Optical Society-Rapid Publications, 5*.

Whiting, P. J., Matisoff, G., Fornes, W., & Soster, F. M. (2005). Suspended sediment sources and transport distances in the Yellowstone River basin. *Geological Society of America Bulletin, 117*(3-4), 515-529.

Williams, G. P. (1970). *Flume width and water depth effects in sediment-transport experiments*. US Government Printing Office.

Woerd, H., & Wernand, M. (2018). Hue-Angle Product for Low to Medium Spatial Resolution Optical Satellite Sensors. *Remote Sensing, 10*(2), 180-198. https://doi.org/10.3390/rs10020180

Woerd, H. J., & Wernand, M. R. (2015). True colour classification of natural waters with medium-spectral resolution satellites: SeaWiFS, MODIS, MERIS and OLCI. *Sensors (Basel), 15*(10), 25663-25680. https://doi.org/10.3390/s151025663

Wyszecki, G.; Stiles, W.S. *Color Science: Concepts and Methods, Quantitative Data and Formulas*; Wiley: Hoboken, NJ, USA, 1982; ISBN 978-0-471-39918-6.

Yegnanarayana, B. (2009). *Artificial neural networks*. PHI Learning Pvt. Ltd..

Yang, C., Ye, H., & Tang, S. (2020). Seasonal Variability of Diffuse Attenuation Coefficient in the Pearl River Estuary from Long-Term Remote Sensing Imagery. *Remote Sensing, 12*(14). https://doi.org/10.3390/rs12142269

York, P. H., Gruber, R. K., Hill, R., Ralph, P. J., Booth, D. J., & Macreadie, P. I. (2013). Physiological and morphological responses of the temperate seagrass Zostera muelleri to multiple stressors: investigating the interactive effects of light and temperature. *PloS one*, *8*(10), e76377.

Yunus, A. P., Masago, Y., Boulange, J., & Hijioka, Y. (2022). Natural and anthropogenic forces on suspended sediment dynamics in Asian estuaries. *Science of the Total Environment, 836*, 155569.

Zaldívar, J.M., Viaroli, P., Newton, A., De Wit, R., Ibañez, C., Reizopoulou, S., Somma, F., Razinkovas, A., Basset, A., & Holmer, M. (2008). Eutrophication in transitional waters: an overview. *Transitional Waters Monographs, 2*(1), 1-78.

Zeldis, J. R., & Plew, D. R. (2022). Predicting and Scoring Estuary Ecological Health Using a Bayesian Belief Network. *Frontiers in Marine Science, 9*, 898992.

Zhang, H., Ma, Y., Zhang, J., Zhao, X., Zhang, X., & Leng, Z. (2022). Atmospheric Correction Model for Water–Land Boundary Adjacency Effects in Landsat-8 Multispectral Images and Its Impact on Bathymetric Remote Sensing. *Remote Sensing, 14*(19), 4769.

Zhang, M., Dong, Q., Cui, T., Xue, C., & Zhang, S. (2014). Suspended sediment monitoring and assessment for Yellow River estuary from Landsat TM and ETM+ imagery. *Remote Sensing of Environment, 146*, 136-147.

Zhang, X., Leonardi, N., Donatelli, C., & Fagherazzi, S. (2019). Fate of cohesive sediments in a marsh-dominated estuary. *Advances in Water Resources, 125*, 32-40.

Zhao, J., Barnes, B., Melo, N., English, D., Lapointe, B., Muller-Karger, F., Schaeffer, B., & Hu, C. (2013, Apr 15). Assessment of satellite-derived diffuse attenuation coefficients and euphotic depths in south Florida coastal waters. *Remote Sensing of Environment, 131*, 38-50. https://doi.org/10.1016/j.rse.2012.12.009

Zhu, J., Hu, P., Zhao, L., Gao, L., Qi, J., Zhang, Y., & Wang, R. (2020). Determine the stumpf 2003 model parameters for multispectral remote sensing shallow water bathymetry. *Journal of Coastal Research, 102*(SI), 54-62.

Zygadlo, M. 2021. NERMN Estuary quality report 2020. *Bay of Plenty Regional Council Environmental Publication 2021/15*.